8-31-2011

Functional 2D nanoparticle/polymer array : interfacial assembly, transfer, characterization, and coupling to photonic crystal cavities

Shisheng Xiong

Shisheng Xiong
Candidate

Nanoscience and Microsystems
Department

This dissertation is approved, and it is acceptable in quality and form for publication:

Approved by the Dissertation Committee:

C. Jeffrey Brinker , Chairperson

Abhaya Datye

Tingshan Luk

John K. Grey

FUNCTIONAL 2D NANOPARTICLE/POLYMER ARRAY: INTERFACIAL ASSEMBLY, TRANSFER, CHARACTERIZATION, AND COUPLING TO PHOTONIC CRYSTAL CAVITIES

BY

SHISHENG XIONG

B.S., Chemical Engineering, Wuhan University, 1999
M.S., Electrical Engineering, Wuhan University, 2002

DISSERTATION

Submitted in Partial Fulfillment of the
Requirements for the Degree of

Doctor of Philosophy
Nanoscience and Microsystems

The University of New Mexico
Albuquerque, New Mexico

July 2011

2011

FUNCTIONAL 2D NANOPARTICLE/POLYMER ARRAY: INTERFACIAL ASSEMBLY, TRANSFER, CHARACTERIZATION, AND COUPLING TO PHOTONIC CRYSTAL CAVITIES

BY

SHISHENG XIONG

ABSTRACT OF DISSERTATION

Submitted in Partial Fulfillment of the
Requirements for the Degree of

Doctor of Philosophy
Nanoscience and Microsystems

The University of New Mexico
Albuquerque, New Mexico

July 2011

ACKNOWLEDGEMENTS

I would like to thank Dr. C. Jeffrey Brinker, my advisor, for his excellent guidance and support during my graduate study, research work, and dissertation preparation. He introduced me to this fascinating filed and trained me hard in molecular/nanoparticle self-assembly. I am thankful to the Center for MicroEngineered Materials (CMEM) for financial support and giving me an opportunity to use the facility. Thanks to Ms. Carol Ashley and other scientists from Advanced Material Lab (AML), including the whole Brinker group for providing access to the facility for my research work.

I am thankful to the Center for Integrated NanoTechnologies (CINT) for providing various facilities and for their support. Help in electron microscopy work by Dr. Ying-Bing Jiang and Dr. Shenghong Huang on UNM main Campus is highly appreciated.

I would like to thank my co-advisor, Dr. Ting Shan Luk (CINT) for his guidance during later part of my research work. In addition, I want to extend my many thanks to Dr. Jiebin Pang, Dr. Darren Dunphy, and Dr. Felix Jaeckel and Mr. Yongqian Gao for contributions in my research work. I am grateful to Prof. J. K. Grey for his help in the spectroscopic characterization of our nanocomposite samples.

I would like to express my gratitude for the support and help from the scientist (Dr. Jin Wang and Dr. Zhang Jiang) at Advanced Photon Source (APS) in Argonne National Lab (ANL) on our X-ray characterization experiments. I would also like to thank Mr. Li Wang and Prof. Ravi Jain for their assistance on some of the PL measurements. The effort of REU students Robert Bradley (North Carolina State University), Tyler Todd (Oral Roberts University), and Matthew Bosch (University of Texas at Austin) are highly

appreciated. UNM undergraduate student Jeff Spencer gave me a lot of help in the nanoindentation and film stretching experiments.

I would also like to thank all my Advisory Committee Members (Dr. C. J. Brinker, Dr. A. Datye, Dr. T. S. Luk and Dr. J. K. Grey) for showing interest in my research work and for their advice and consistent cooperation. Finally, I would thank MS Carol Ashley, MS Cathleen Casper, and MS Heather Armstrong for their sustaining support during my study and research.

This work is supported by DOE Office of Basic Energy Sciences. Use of the Advanced Photon Source was supported by DOE Office of Basic Energy Sciences under Contract No.DE-AC02-06CH11357. Sandia is a multiprogram laboratory operated by Sandia Corporation, a Lockheed Martin Company, for the United States Department of Energy's National Nuclear Security Administration under Contract DE-AC04-94AL85000.

Finally, I am extremely thankful to my parents whose blessings and encouragement has always been a part of my life and played a very important role in making me what I am today.

Functional 2D Nanoparticle/ Polymer Array: Interfacial Assembly, Transfer, Characterization, and Coupling to Photonic Crystal Cavity

By

Shisheng Xiong

We developed a universal, facile and robust method to prepare free-standing, ordered and patternable nanoparticle/polymer monolayer arrays by evaporation-induced self-assembly at a fluid interface. The ultra-thin monolayer nanoparticle/polymer arrays are sufficiently robust that they can be transferred to arbitrary substrates, even with complex topographies. More importantly, the Poly (methyl methacrylate) (PMMA) in the system serves as a photoresist enabling two modes of electron beam (e-beam) nanoparticle patterning. These ultra-thin films of monolayer nanoparticle arrays are of fundamental interest as 2D artificial solids for electronic, magnetic and optical properties and are also of technological interest for a diverse range of applications in micro- and macro-scale devices including photovoltaics, sensors, catalysis, and magnetic storage. By co-assembly with block co-polymers, the nanoparticles were selectively positioned in one specific phase, representing a high throughput route for creating nanoparticle patterns. The self-assembly process was investigated by combined in-situ grazing incidence small angle x-ray scattering (GISAXS) and numerical simulation. By e-beam irradiation of free-standing 2D NP/polymer arrays, anisotropic nanowire arrays have been fabricated. Additionally, preliminary investigation on assembly of binary nanoparticle arrays has also been introduced, serving as promising future directions of interfacial assembly.

Controlling the rate of spontaneous emission and thus promoting the photon generation efficiency is a key step toward fabrication of Quantum dot based single-photon sources, and harnessing of light energy from emitters with a broad emitting spectrum. Coupling of photo emitters to photonic cavities without perturbing the optical performance of cavities remains as a challenge in study of Purcell effect based on quantum electrodynamics.

Taking advantage of interfacial assembly and transfer, we have achieved controlled deposition of quantum dots into high Q photonic microcavities and studied the modification of their optical properties. Anomalous enhanced spontaneous emission and Fabry-Perot resonance have been observed.

KEYWORDS: Nanoparticle/polymer monolayer array, nanocomposite, Evaporation Induced Self-Assembly (EISA), E-beam lithography, patterning, energy transfer, catalysis, photonic crystal, Raman spectroscopy

TABLE OF CONTENTS

LIST OF TABLES

LIST OF FIGURES

Figure 5.7: (a) Comparison of PL signals from the QD-photonic crystal cavity systems prepared by picking or lifting transfer processes. The inset denotes the region of excitation marked by a black dashed circle. This resonance is referred to as E_x resonance with its emission polarization parallel to the waveguide. The PL is collected by a spectrometer with a 300 g/mm grating and 50 μm slit width. (b) Enhanced photoluminescence spectrum of E_y resonance of a L3 photonic crystal microcavity collected by a spectrometer with a 300 g/mm grating and 50 μm slit width. The polymer used in the sample for this experiment is polystyrene. The inset shows a high-resolution measurement of the same resonance measured with a 900 g/mm grating and a 10 μm slit width. The linewidth of the resonance is measured to be 0.2 nm and the corresponding Q factor is 8028……..……90

Figure 6.1: (a) SEM image of a 2D silicon membrane photonic crystal device consists of two L3 cavities and a waveguide supported with SiO_2 anchors. The top left inset shows the top view of the holes on the silicon membrane. The lower right inset shows the side wall profile of the holes. (b) Top SEM view of the L3 cavity created by three missing air holes. (c) SEM image of a cavity with polymer film on top. (d) TEM image of a monolayer of PbS in P3HT polymer. Lower left inset shows a free-standing film hanged by a corner feature of the photonic crystal sample……..…….94

Chapter 1. Introduction

1.1 Progress of nanotechnology

Materials science is the basic foundation of all technological advances and is dated back in the history of the earth earlier than the living organisms on the planet earth. Some of the earliest materials known to the mankind include wood, stone, and bone. [1] The inorganic materials existing in the world are majorly categorized as: (1) metals, (2) ceramics, (3) polymers, (4) composites, and (5) semiconductors. The prefix nano means a billionth ($1x10^{-9}$). The research at nanoscale has emerged for several hundred years since the first synthesis of metal nanoparticles by Faraday. However, only after the invention of novel characterization tools such as electron microscope, our ability to analyze, manipulate, and better understand molecular scale phenomena has facilitated an increased thrust in this area of research.

Nanotechnology refers to technological applications of the structures with at least one of the physical dimensions of an order of 100 nm or less.[2] As a result, the physical and chemical characteristic of nanomaterials acts as an intermediate between the molecular unit and the bulk material.

Continual decrease in the size of electronic devices is a major driving force for rapid improvement in the area of nanotechnology. Most important to the electronics applications, it is crucial to fabricate devices with high storage density, low power consumptions, and with high speeds. This requires reduction in the device dimensions and complies with the trends predicted by Gordon Moore in his Moore's Law (1965). In addition to the increased computational abilities, these technological advancements have

affected areas such as medicine and space travel. Nanotechnology enables the fabrication of nanometer scale devices and structures with unique properties and potential for new clean energy sources,[3] pollution control systems,[4] catalysts or catalyst supports,[5] nanoscale sensors,[6] and drug delivery tools working inside the human body to detect and treat diseases.[7] At a nanometer-scale, the mechanical properties differ from the bulk properties, and the surface properties are dominant. There is enough evidence of an on-going research in nanoscale electronics and molecular electronics. [8-10]

Progress in nanotechnology necessitates inventing methods to observe, characterize, and control the phenomena at the nanometer-scale. Characterization techniques such as electron microscopy, scanning probe microscopy, and X-ray methods assist in studying materials at nanoscale. Nanoscale measurements are challenging and require tomographic imaging, atomic scale resolution, and scanning over large area. [11] Emergence of the novel characterization techniques such as scanning tunneling microscopy (STM) and atomic force microscopy (AFM) are few of the reliable methods to investigate the nanoscale phenomena. [12,13] Not only, these techniques facilitated the characterization and measurements but also eased the manipulations at the molecular scale. This ability to manipulate can be further enhanced by combining with the techniques such as transmission electron microscopy (TEM). [14] Recently, STM technique was also used to manipulate the bonding of a molecular species such as carbon monoxide and the structure and vibrational properties of the product were analyzed. [15] But the concerns of the temperature, surface diffusion, conductivity of the sample, and precision in the bond maneuvering using STM tip are of the high priority.

1.2 Top down and bottom up approaches at nanometer scale

Understanding of the nanostructures can be split in two ways: [16] defining nanostructures according to the fabrication methods such as vapor phase growth, liquid phase growth, solid phase growth, and hybrid growth which couple various processes. Another way to categorize them is on the basis of the product synthesized such as nanoparticles, nanowires, nanotubes, thin films, and other hybrid nanostructures such as photonic band gap crystals.

Two basic approaches to fabricate or synthesize the nanomaterials and nanostructures are top-down and bottom-up. [17] Synthesis of materials in solution can be an example of the bottom-up approach while grinding and milling operation to produce micro or nanoparticles can be an example of the top-down approach. The devices such as complementary metal oxide semiconductor devices (CMOS) [18] are fabricated in a hybrid method incorporating both the aforementioned approaches. Nanostructures can be fabricated by utilizing the top down approaches which includes the fabrication of nanowires using lithography techniques. [19] But such an approach can produce nanowires with imperfection in surface structure and the defects during subsequent etching processes. Defects in the nanostructures can drastically affect its physical, chemical, and electrical properties. While the bottom-up approach relies on the basis that the fabrication steps or growth involves atom-by-atom build up process. Energy considerations are crucial to such a process and thus, the resultant nanomaterials or nanostructures are at the minimal energy state or thermodynamic equilibrium. This is a very common approach and has been used extensively since long time. [20]

It is easy to extract an analogy between STM atom-by-atom approach, nanostructure fabrication, and synthetic chemistry. All three incorporate the bottom-up approach towards final result. The synthetic chemistry can involve complicated synthesis methods and thus, specificity becomes an important issue in such processes. While, majority of the biological phenomena demonstrates an excellent trend for the self assembly or self replication processes. This introduces a long term goal for the scientists in this research area to develop methods which can self organize the nanostructures to result in various functionalities. Major challenges in the nanotechnology include the nanostructures with controlled properties and dimensions, integration of the nanostructures into functional and scalable devices, and most importantly, novel techniques to characterize materials at the nanoscale.

1.3 Brief overview of the chemistry and physics involved at nanometer scales

The properties of the nanostructures are different than their bulk materials because of dramatic change in the ratio of surface atoms to interior atoms. It has been demonstrated for palladium that percent of surface atoms is much higher for Pd nanoparticles as compared to the large palladium microcluster. [21] Nanostructures have high surface to volume ratio and thus associated with high surface energies and require methods to reduce the surface energy. There are four different ways to reduce surface energy of a given surface:[16]

- Surface relaxation, which is more common in fluids where higher energy atoms or ions have tendency to move inward to lose their energy.

- Surface restructuring which involves annihilation of surface dangling bonds.
- Surface adsorption, where dangling bonds are occupied by other species.
- Composition segregation, by adding impurities to form bonds with surface dangling bonds and also involves processes like solid state diffusion.

These concepts can be further understood by the concept of chemical potential, which is dependent on the surface curvature of the nanostructure. Understanding of the chemical potential is related to phenomena such as Ostwald ripening, sintering, and formation of faceted crystals at the nanometer scale. In addition, the nanoscale structures can be the basis of understanding the dependence of material properties on their dimensionality. For example, 1-D nanostructures exhibit density of states singularities, energetically discrete molecular states, and spin charge separation. [22] The nanometer scale size also confines the number of electrons present in these nanostructures. The properties of these nanostructures are highly dependent on the number of electrons and require understanding, particularly, in the quantum mechanical regime. Such length scale confinements can further approve of difference in electronic properties in different spatial directions (l_x, l_y, l_z). Taking into consideration particle in a box situation where $\Delta E \alpha l^{-2}$ and if $l_x >> l_y$, l_z then the degree of freedom of electrons will be confined in y and z direction. Thus, nanostructure is quasi 1-D where electron has only degree of freedom in x direction. If $l_x \sim l_y >> l_z$, then the nanostructure is quasi 2-D. Similarly, if $l_x \sim l_y \sim l_z$, then the nanostructure is quasi 3-D. Such particle confinement has led to study of low dimensional, few body systems. Nanostructures where the electrons are confined in all the three directions are termed as quantum dots or 0-D nanostructures. The electron wavelength in such structures is of same length scale as that of confinement and thus,

quantum effects become extremely important. Due to their finite size, nanostructures find many applications in emerging area of nanoelectronics, functional nanoscale materials, and as nanoscale probes.

1.4 Nanoparticles

Nanoparticles are tiny objects sized between 1 and 100 nanometers. Nanoparticles often exhibit size-related properties that differ significantly from their bulk counterparts. Additionally, their distribution, shape, chemical composition, crystallinity, and uniform dispersion are also important issues. Significant advancement has been made in self assembled, uniformly dispersed, and size tunable nanoparticles in the last decades. [23-26]

Synthesizing nanoparticles by homogeneous nucleation involves the supersaturation of the growth species. This can be either achieved by modulating the temperature or the solubility of the reactants in a particular growth environment. [16] While heterogeneous nucleation of the nanoparticles occurs via formation of a new phase on the surface of another material. The process involves surface diffusion and aggregation leading to decrease in free energy of the system.[16]

Metal colloidal particles can be synthesized by reduction of metal complexes in dilute solutions.[27,28] The synthesis involves use of precursors, reducing reagents, and a method to control the reduction reactions as indicated in table 1.1.[16] Colloidal gold nanoparticles were reported for the first time by Michael Faraday in 1857[29] and are still under intense investigation by numerous researchers. These can be easily produced in a chemical reaction with water as a reaction medium involving chloroauric acid as a precursor and, sodium citrate as a reducing agent. Nanoparticles of rhodium with diameters between 0.8

to 4 nm have also been reported. [16] Methanol was used as a reducing agent and polyvinyl alcohol as a stabilizer. Concentration of the reducing agent and refluxing time are few of the important parameters that needed to be controlled.

Utilizing reverse micelles formation, nanoparticles of iron were also synthesized in a chemical reaction using cetyltriethylammonium bromide (CTAB) as a surfactant and octane as a oil phase. [30] Another technique to synthesize metallic nanoparticles in solution is based on electrochemistry. [31] Nanoparticles of semiconductors and oxides are also of much technological interests. Such nanoparticles can be prepared by variety of methods[16] such as sol-gel methods, forced hydrolysis, by controlled release of ions, vapor phase reactions, solid state phase segregation, spray pyrolysis, and the template based synthesis.

In many applications it's desired to disperse nanoparticles uniformly in solution. [32] For instance the gold colloidal nanoparticles were dispersed onto a silane functionalized silicon substrate or by chemically modifying the nanoparticle surface. [33],[34] Single electron transistors, switches, and sensors have been demonstrated treating each nanoparticle as a discrete quantum island. [35]

1.5 Nanowires

Nanowires are rigid nanostructures with micrometer-scale lengths and nanometer-scale diameters and can be metallic,[36] semiconducting,[37] or insulating.[38] Numerous interesting properties of these nanowires have been investigated including the electron transport studies and nanoscale sensing. [39,40] There are abundant choices of materials for fabricating different nanowires including those of polymers.[41] Nanowires can be grown

by variety of methods such as laser ablation,[42] template based growth,[43] solution phase growth,[44,45] and high temperature growth.[46] Four general approaches to synthesize or fabricate these nanowires are: (1) Spontaneous growth (Evaporation-condensation, VLS or SLS, and stress induced crystallization), (2) Template based growth (Electrochemical methods, colloid dispersion, solution filling, Chemical reaction based conversion), (3) Electrospinning, and (4) Lithography.

1.6 NP Assembly for Applications

NPs may be assembled using a variety of techniques. The most common techniques for NP assembly are top-down, including previously discussed procedures such as lithography, templating, and transfer printing; as well as other procedures such as dip-pen nanolithography, fluid-assisted assembly, and LBL thin-film assembly. Bottom-up NP assembly techniques involve NP self-assembly that is guided by various methods including bioconjugation, electrostatic interactions, steric interactions. These techniques allow the synthesis of various photonic devices, electronic devices, and sensing devices.

Top-down NP Assembly for Applications. Many top-down NP assembly techniques are two-fold. The first step involves patterning the substrate using techniques such as lithography and dip-pen; the second step involves the overlay of nanomaterials onto these patterned substrates using various methods including atomic force microscopy (AFM), fluidics, and electrical field induced alignment to make useful devices. As discussed previously, the most common technique to produce ordered nanoscale structures is lithography. While still a time consuming and expensive process that is somewhat limited in the size with which nanostructures may be produced (owing to the

resolution limits in the wavelength of irradiation used to create the nanostructures), it is commonly used to prepare the backbone of many nanoscale devices.

DPN is another technique used to pattern substrates that was developed by the C. Mirkin group. This technique uses an AFM tip to deliver a material directly onto a substrate, much as a fountain-tip pen delivers ink to a page. [47,48] This method allows for any molecule that will adhere to the substrate (thiols on gold surfaces for example) to be patterned onto a substrate using an AFM tip. This application tool is very small and can be controlled with resolution down to 5 nm. This technique may also be applied in parallel using multiple AFM tips simultaneously to scale up the process.

In addition to patterning substrates with molecules, as with DPN[48], AFM is also used to physically manipulate and move nanomaterials around on substrates[49]. One such method grows CNTs on an AFM tip, then using AFM, breaks the CNT off at the desired location to deposit the CNT[50]. Obviously, this is a very tedious, time consuming method that is difficult to scale up.

One of the more common and useful techniques to order nanomaterials onto patterned substrates is using fluids to carry the nanomaterials into position. In this technique, a shear force generated by a laminar flowing liquid in a microfluidic device aligns NWs in a parallel orientation. The NW containing fluid is passed over a patterned substrate, where the NW adheres.[51,52] This process typically is used to suspend NWs over previously patterned electrodes in the substrate, and can be manipulated to create crossed NWs to give various nanocircuits. This process offers quicker and more efficient NW organization than AFM assisted assembly techniques.[49]

Another technique to arrange nanomaterials onto substrates is by the application of an external force, such as that generated by an electronic[53] or magnetic field[54]. In the case of magnetic fields, magnetic NWs are immobilized on substrates patterned with magnetic trapping sites. NWs can be segmented with various materials to help determine which part of the NW is immobilized on the substrate[54]. External electronic fields generated between electrodes can also allow NWs to align on a substrate[55]. Parallel NWs align between parallel electrodes[52], and by rotating the field, the NWs may be crossed.

LBL films can also be used to create layers of nanomaterials on a substrate[56]. In this technique, hybrid organic/inorganic layers of oppositely charged materials are layered onto a substrate. This is typically done by dipping the substrate into one material, rinsing, and then dipping it into the next material, rinsing, and repeating the process until the desired number of bilayers has been reached. This can be done with nanomaterials to create sandwiches of nanomaterials in other materials such as PDDA.

1.7 Challenges and Motivations

Limitations of current approaches for making robust and ordered 2D NP/polymer array:

- With LB/LS method, the NP monolayer is transferrable, but we can not make composite
- By drop evaporation, highly ordered NP array can be made, but the monolayer cannot be transferred
- LBL method is flexible in making layered structure and the spacing between layers can be precisely controlled, however, the in-plane

arrangement is poor

- NPs can be selectively positioned in specific phase, but they are clusters instead of arrays

Project Motivation: Unnecessary to change the surface chemistry of NPs, any as-synthesized hydrophobic NPs mixed with a homopolymer at appropriate ratio can be dispensed onto fluid surface and form 2D NP/polymer monolayer array. The dry film floating on fluid surface can be transferred to any solid substrate, even pre-patterned surface for integration of functional devices. Robustness, transferability and flexibility (in composition) will be among the advantages for this technique.

1.8 Goals of the research

"Breaking the 2D, small-area bottleneck"- Explore and develop large-area, 3D fabrication techniques for metamaterials. We are seeking to codify and demonstrate fabrication of 2D and 3D structures. Specifically, we will investigate bottom-up fabrication of monodisperse and structured (core-shell) nanoparticles and their incorporation into large area metamaterial patterns with directed self-assembly. "Metamaterials" with periodic ordering and with both abrupt and adiabatic period variations can thus be investigated. The major research is based on fabricating robust, free-standing, functional and transferrable nanoparticle/polymer monolayer composite, and use it as ideal 2D platform for research in catalysis, electron transfer/transport, energy transfer/transport. Using specific polymer as matrix, novel functions will be introduced, such as patterning, or conductivity. Our investigations will be organized with three parallel, interactive, iterative thrusts: theoretical analysis of different structures and

materials, nanofabrication of large area samples, and detailed nanoscale (near- and far-field) characterization of the resulting composite materials.

Recently we have reported a universal, facile and robust method to prepare free-standing, patternable nanoparticle/polymer monolayer arrays by evaporation induced self-assembly at a fluid Interface (C.J.B et. al., JACS 2008). The ultra-thin monolayer nanoparticle/polymer arrays are sufficiently robust that it can be transferred to arbitrary substrates and can be suspended as a free-standing membrane over cm-sized holes - even with free edges. More importantly, the poly (methyl methacrylate) (PMMA) in the system serves as a photoresist enabling two modes of electron beam (e-beam) nanoparticle patterning. Lower e-beam doses direct differential nanoparticle solubility and result in nanoparticle patterns with somewhat diffuse interfaces. At higher e-beam doses the PMMA serves as a negative resist resulting in sub-micrometer patterns with edge roughness comparable to that of the nanoparticle diameter. These ultra-thin films of monolayer nanoparticle arrays are of fundamental interest as 2D artificial solids for electronic, magnetic and optical properties and are also of technological interest for a diverse range of applications in micro- and macro-scale devices including photovoltaics, sensors, catalysis, and magnetic storage.

Using the Au NP/polymer monolayer arrays as a nice 2D model, we studied the catalysis for conversion of carbon monoxide to carbon dioxide, with a supporting titanium dioxide layer deposited by atomic layer deposition (ALD).

High Q optical microcavities can be used to control radiative process of dipole emitters such as quantum dots through photonic density of states control. By enhancing the spontaneous emission, heat dissipating non-radiative relaxations can be suppressed

therefore resulting in greater light emitting efficiency and provide a possibility of extracting multi-exciton energy by emission process. In order to study the radiative control of quantum dots, it is important to be able to incorporate these emitters without perturbing the optical properties of the cavity. As proposed, we explore controlled deposition of quantum dots into high Q photonic microcavities and study the modification of their optical properties.

Moreover, by replacing the PMMA polymer matrix with conjugated polymer, such as poly-3-thiophene (P3HT), charge transfer across the interfaces of Au NPs and this polymer will be interrogated, using a combination of I-V measurement and Raman spectroscopy. With scanning Raman spectroscopy, the Raman scattering intensity, as well as frequency has been mapped, for Au NP/P3HT monolayer arrays transferred onto a discovery platform (DP) with pre-deposited interdigitated electrode arrays (IDA). This can lead to a new way to find the route of charge transfer in this system.

Interactions between semiconductor and metallic nanoparticles are the subject of intensive investigations. Enhanced photoluminescence (PL) yield of quantum dots in the presence of notable nanoparticles or nanohole arrays has potential applications in light-emitting diodes (LED) and sensors. Surface plasmon resonances (SPR) are believed to either increase the PL efficiency by enhancing the local exciting field or cause nonradiative damping due to energy transfer through an inverse route. By transferring one monolayer of QD film onto another monolayer of metallic NP film we will be able to quantitatively analyze the PL enhancing or quenching effect, in case the spacing between two layers can be precisely controlled.

Materials with controlled catalytic and transport properties are needed in diverse areas of emerging technologies of interest, including membrane-based separations and sensing, fuel cells, artificial photosynthesis, petrochemical and fine chemical synthesis, combustion, and mitigation of environmental pollutants. The focus of our research is the design, synthesis and understanding of model self-assembled materials whose controlled nanocomposite architecture could reveal how nanostructuring and nanoconfinement influence transport (energy, electronic, and molecular) and catalysis and to investigate the interplay between transport and catalysis. Materials synthesis efforts exploit expertise in multicomponent self-assembly to form model composite and porous materials integrated into platforms allowing their structural and functional characterization (e.g. catalysis and transport) and providing electronic, optical, fluidic, and spectroscopic addressability.

Nanostructure	Size	Material
Clusters Nanocrystals Quantum dots	Radius: 1–10 nm	Insulators, semiconductors, metals, magnetic materials
Other nanoparticles	Radius: 1–100 nm	Ceramic oxides
Nanobiomaterials Photosynthetic reaction center	Radius: 5–10 nm	Membrane protein
Nanowires	Diameter: 1–100 nm	Metals, semiconductors, oxides, sulfides, nitrides
Nanotubes	Diameter: 1–100 nm	Carbon, layered chalcogenides
Nanobiorods	Diameter: 5 nm	DNA
2D arrays of nanoparticles	Area: several nm^2–μm^2	Metals, semiconductors, magnetic materials
Surfaces and thin films	Thickness: 1–1000 nm	Insulators, semiconductors, metals, DNA
3D superlattices of nanoparticles	Radius: several nm	Metals, semiconductors, magnetic materials

Figure 1.1 Nanostructures and their assemblies and dimensions. [2]

Chapter 2. Interfacial assembly and transfer of nanoparticle array

2.1 Introduction

Ordered nanoparticle (NP) monolayers are of fundamental interest as 2D artificial solids in which electronic, magnetic and optical properties can be tuned through electron charging and quantum confinement of individual NPs mediated by coupling interactions with neighboring NPs. They are also of technological interest for a diverse range of applications including photovoltaics, sensors, catalysis, and magnetic storage. To date a myriad of techniques including Langmuir-Blodgett (LB) deposition,[57-59] droplet evaporation,[60-63] and interfacial assembly have been used to organize monosized, hydrophobic NPs into ordered 2D arrays.[64] It is generally agreed that for all these approaches NP assembly is driven by attractive van der Waals interactions balanced by steric repulsion. However, under attractive conditions, depending on the competing effects of NP diffusion, convection and solvent de-wetting, a variety of patterns can emerge including ordered 2 and 3D arrays as well as fractal aggregates, 'coffee rings' and percolation clusters.[65-68] For this reason maintaining NPs at a fluid interface – either in evaporation droplets or at a water surface - has been successful in creating rather large scale, ordered NP monolayers. van der Waals interactions confined to NP interstices confer to these monolayers a high Young's modulus allowing them to be prepared as free-standing membranes spanning 500-nm apertures and to be transferred from a water surface to a solid substrate via micro-contact printing using a pre-patterned poly(dimethylsiloxane) (PDMS) stamp.[69,70]

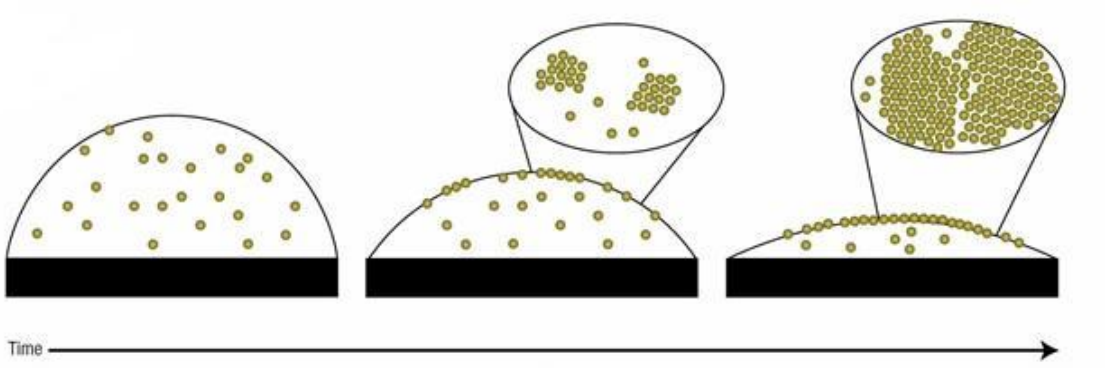

Figure 1 Self-assembly of Au NP monolayers by drop evaporation.

Here we extend the burgeoning work on NP monolayer fabrication in three substantive respects. First, we assemble hydrophobic gold NPs on a water interface from toluene containing PMMA. In this case solvent evaporation concentrates the thinning film in NPs and PMMA, leading to NP self-assembly and solidification into an ordered NP/polymer nanocomposite monolayer with physical dimensions of up to $10cm^2$ (see Figure 3a). Second, the NP/PMMA monolayer can be transferred to arbitrary substrates and remains stable as a free-standing membrane suspended over cm-sized holes - even with free edges (Figure 3a). Third, the PMMA serves as a photoresist enabling two modes of electron beam (e-beam) NP patterning. Lower e-beam doses direct differential NP solubility and result in NP patterns with somewhat diffuse interfaces as shown previously for e-beam patterning of 1-dodecanethiol ligated Au monolayers deposited on silicon nitride[71] (Figure 16 a,b). At higher e-beam doses the PMMA serves as a negative resist resulting in sub-micrometer patterns with edge roughness comparable to that of the NP diameter (Fig 16 c,d). In combination these extensions contribute to the ability to integrate NP arrays into robust micro- and macro-scale devices. Additionally this

approach represents a new means to attain very highly loaded yet flexible particle/polymer nanocomposite,[67] which have eluded most synthetic efforts to date.

2.2 FABRICATION, TRANSFER, CHARACTERIZATION, AND PATTERNING OF 2D NP/POLYMER MONOLAYER ARRAYS

2.2.1 Fabrication of 2D NP/polymer monolayer arrays

In this section we take Au NP/polymer monolayer array as an example to demonstrate the fabrication process. Monosized 1-dodecanethiol-ligated Au NPs (about 5.5nm in diameter) were synthesized by a modified single phase method[72] (see Supporting Information). For monolayer self-assembly, 60 mg of NPs were dissolved in 6mL of toluene containing 100mg of PMMA (M_w = 996000, Aldrich). To prepare the NP/polymer monolayer, one drop (about 2-3 μL) of the NP/PMMA/toluene solution was carefully dispensed onto the surface of de-ionized water contained in an uncovered beaker. The droplet quickly spread onto the water surface (within ~1s) forming an approximately 50-micrometer thick film with area of ~5-cm. Evaporation-driven polymer solidification of the film perimeter establishes the maximum extent of spreading and pins the three phase liquid/solid/vapor interface. Further evaporation necessarily thins the film maintained at constant area (at the very last stage of drying a slight radial contraction is observed). Based on the progression of optical interference fringes, we know that the film thins from the perimeter and imagine that, correspondingly, NP self-assembly and solidification proceed in a radially-directed manner. If, as recently shown for hydrophobic Au NPs assembled within an evaporating droplet of toluene on a solid support,[63] NPs are captured and preferentially localized at the liquid/vapor interface,

nucleation and growth of ordered NP array islands could proceed to a large extent within this fluid interface before evaporation-driven polymer solidification, explaining the formation and stabilization of the large area NP arrays we observe.

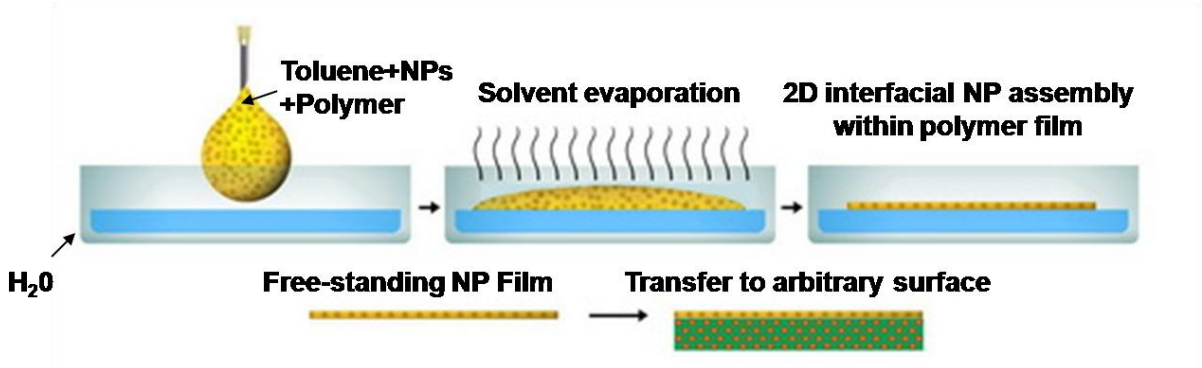

Figure 2 Schematic diagram for formation of NP/polymer 2D array by interfacial EISA

2.2.2 Transfer of 2D monolayer arrays to solid substrates

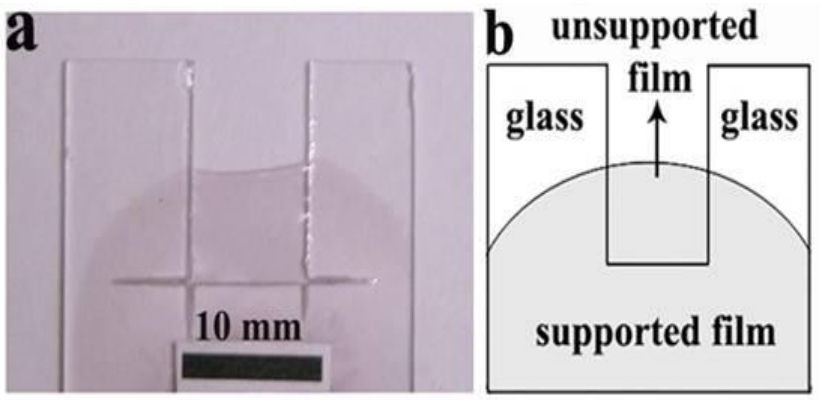

Figure 3 a) Optical image of large scale, 2D Au NP / PMMA array captured on glass plate with 1cm gap b) Schematic of (a).

NP/polymer monolayer films were transferred to solid and porous substrates by lowering the substrate through the water surface, contacting the film edge, and vertical withdrawal. As shown in Figure 3a, large areas of homogeneous, supported and free-standing films can be formed in this manner.

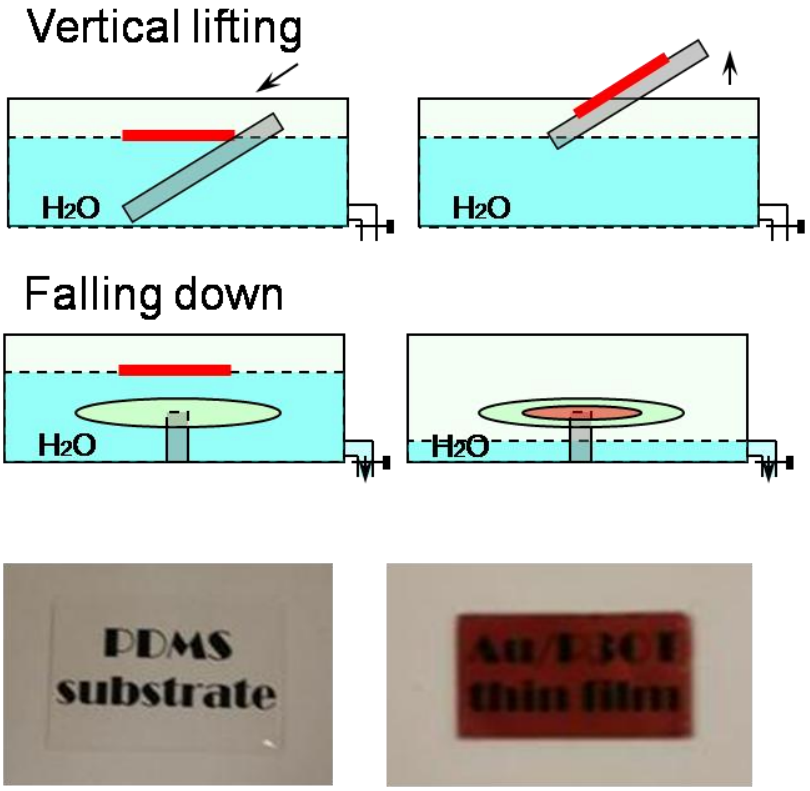

Figure 4 Method for transfer the film onto substrate and Au/P3OT monolayer array transferred onto elastic PDMS substrate.

To avoid any vibration from manual capturing of film from water surface, a trough with immersed support for substrate was designed, thus the film can fall down naturally to the substrate after water in the trough drain away.

Since the original film was formed on fluid surface, theoretically we are able to transfer this film onto arbitrary solid surfaces. For different purposes, we have successfully transferred the film onto holey carbon TEM grid, single-hole copper grid, PDMS substrate (see Figure 4), silicon wafer, glass cover slide, interdigitated electrode arrays, as well as 2D photonic crystal.

2.2.3 Characterization (TEM, SEM, AFM, GISAXS, PL and UV-Vis spectroscopy)

Physical properties of the Au NP/PMMA monolayer were characterized by standard electron microscopy and UV-visible spectroscopy along with grazing incidence small angle x-ray scattering (GISAXS).

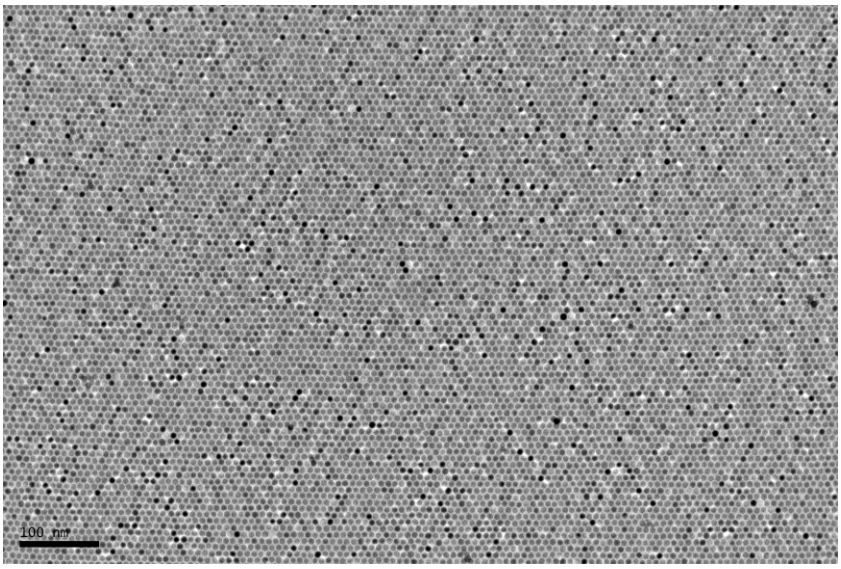

Figure 5 High resolution TEM images of Au NC/PMMA monolayer arrays.

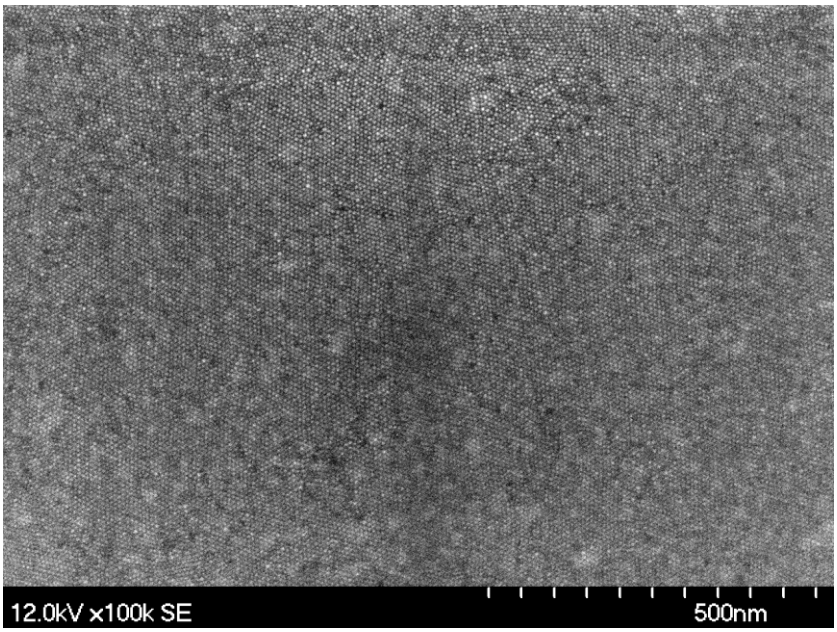

Figure 6 SEM image of Au NP/PMMA monolayer array.

SEM images of Au NP/PMMA array transferred onto Si wafer were taken at high resolution. Contrary to TEM images, the Au NPs appear as bright spots from scattering of electrons. This verified that large area, highly ordered NP array could be prepared with interfacial assembly.

This facile method can be extended to various kinds of hydrophobic NPs. For example, we prepared PbSe QD/PMMA monolayer array, CdSe NR/PMMA monolayer array, and Au NP/Fe_2O_3 QD/PMMA binary monolayer array with precise control on the ratio between different NPs.

Film thickness can be determined either by profilometry or ellipsometry or by scanning across a scratch on film transferred to hard solid substrate with AFM. Results from different methods for same sample were surprisingly consistent. It's indicated that the film to be about 20-70nm thick, dependent on the experimental condition.

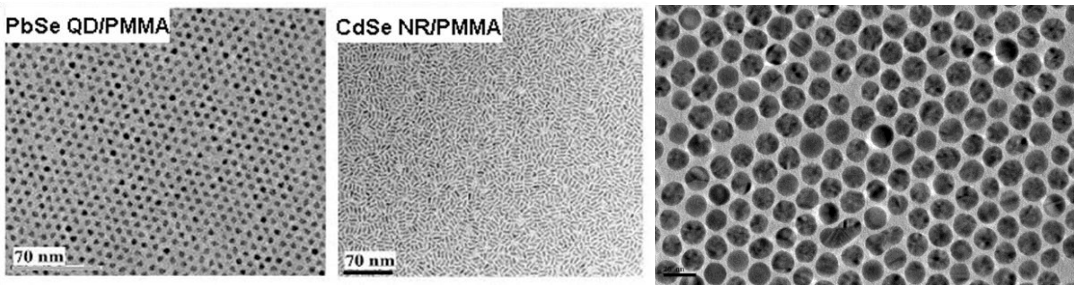

Figure 7 High resolution TEM images of PbSe QD/PMMA monolayer array and CdSe NR/PMMA monolayer array and Au NP/P3HT monolayer array.

Figure 5 and Figure 6 show representative TEM and SEM images of solid-supported and free-standing NP/PMMA monolayers, respectively. Ordering is commensurate with that observed previously for pure organic-ligated NP arrays formed on solid or fluid surfaces.[69,72] However comparison of center-to-center NP spacing of monolayer arrays assembled without and with PMMA shows a reduction from 7.5-nm (TEM not shown) to 6.3-nm (analysis of the GISAXS data, Figure 8c), respectively. This

contraction is perhaps unexpected in consideration of the added PMMA. Conceivably the PMMA is at both interfaces and its evaporation-driven solidification serves to compress slightly the monolayer at the final stage of drying.

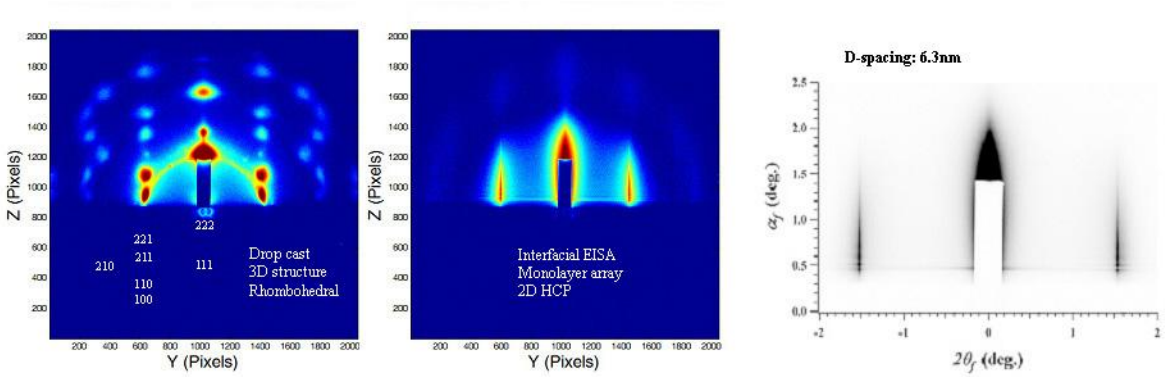

Figure 8 GISAXS pattern showing 3D (left) and 2D (center) ordered NP arrays and mathematical determination of the D-spacing for Au NP array (right).

The GISAXS pattern in Figure 8 shows exclusively vertically modulated diffraction lines (as opposed to spots associated with 3D superlattices) consistent with long-range in plane order expected for a 2D monolayer. UV-visible spectroscopy of the Au NPs in bulk toluene versus self-assembled in a PMMA composite monolayer show an approximate 40-50nm (~0.2eV) shift of the plasmon resonance frequency to lower energy (see Supporting Information). Based on a classical model of the plasma frequency, this shift can be interpreted as arising from the higher dielectric constant of the medium surrounding an individual NP due to its six in plane NP neighbors.[58]

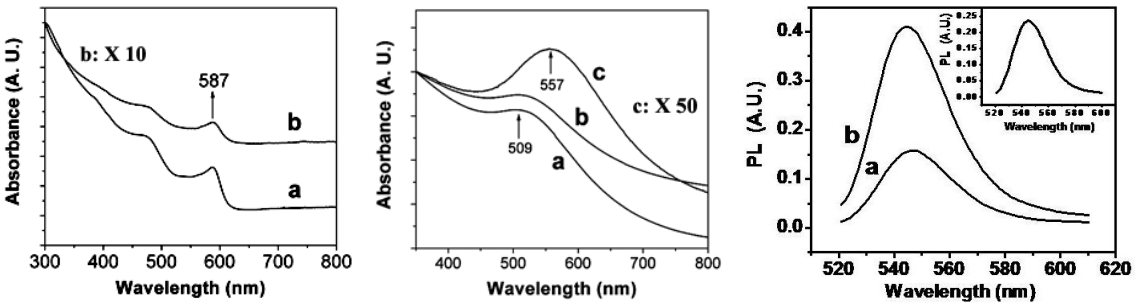

Figure 9 Left: Visible absorption spectra for the CdSe NRs/polymer in toluene (a), and the CdSe

NR/polymer ultra-thin film (b). Center: Visible absorption spectra for the Au NPs in toluene (a), Au NPs/polymer in toluene (b), and the Au NPs/polymer ultra-thin film (c) Right: Photoluminescence (PL) spectra for the CdSe QDs in toluene (inset), the CdSe-QDs/polymer monolayer (a), and 5 stacking layers of the CdSe-QDs/polymer monolayer (b).

Optical properties of NPs are generally preserved in transparent polymer matrix. However, UV-visible spectroscopy of the Au NPs in bulk toluene versus self-assembled in a PMMA composite monolayer show an approximate 40-50nm (~0.2eV) shift of the plasmon resonance frequency to lower energy (see Figure 9). Based on a classical model of the plasma frequency, this shift can be interpreted as arising from the higher dielectric constant of the medium surrounding an individual NP due to its six in plane NP neighbors.[58] Linear relationship was found for photoluminescence measured for monolayer and 5 stacking layers of CdSe QD/PMMA.

Multilayer of alternating Au NP layer and CdSe NR layer was also fabricated. Firstly, a monolayer thin film of Au NP was fabricated and transferred onto a glass substrate according to the above procedures. After the film was dry at room temperature, another monolayer of CdSe NR was transferred onto the pre-formed Au NP monolayer according to procedures described before. By repeating the above procedures, multilayer of Au NP and CdSe NR was fabricated. Similar procedures were performed to prepare multilayer ultra-thin film onto a TEM grid for TEM characterizations. To prepare ultra-thin film of different types of NPs in one single layer, Au NP and the other NP at an appropriate ratio were dissolved in a PMMA /Toluene solution, followed by same procedures to prepare the monolayer ultra-thin films.

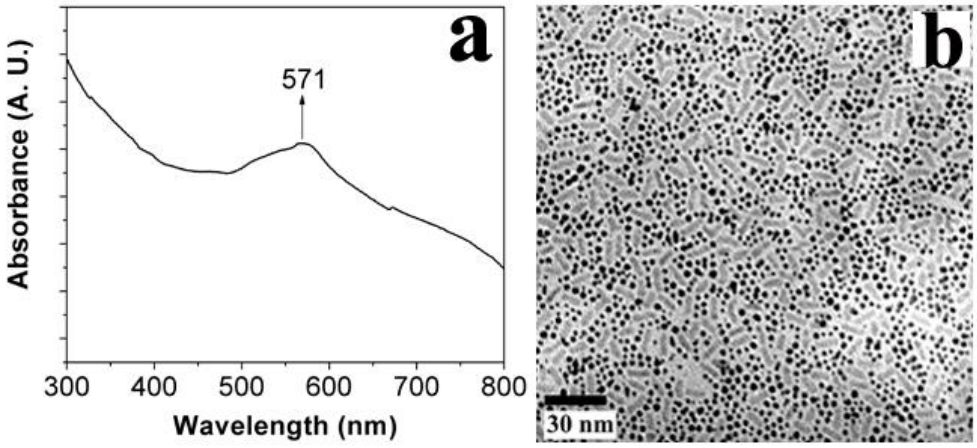

Figure 10 Visible absorption spectrum (a) and a representative TEM image (b) for the Au NP/CdSe NR/polymer monolayer ultra-thin film caught on a glass slide and a TEM grid, respectively.

Figure 10 shows the absorption spectrum (a) and a representative TEM image (b) for the Au NP/CdSe NR/polymer monolayer ultra-thin film. It shows an absorption peak at 571nm, which is between the absorption peaks of Au NP/PMMA monolayer film (557nm) and CdSe NR/PMMA monolayer film (587nm). As shown from the TEM image (Figure 12 b), the Au NP and CdSe NR are randomly but homogeneously organized in a monolayer manner. The Au NPs exhibit higher contrast (darker in color) than the CdSe NRs.

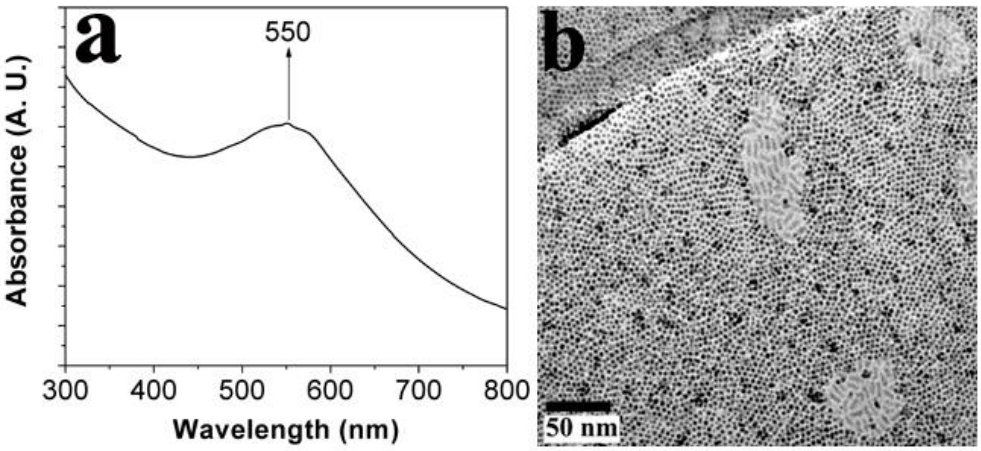

Figure 11 Visible absorption spectrum (a) for a Au NP/CdSe NR/polymer alternating four-layer film

caught on a glass slide and a representative TEM image (b) for a Au NP/CdSe NR/polymer alternating two-layer film caught on a TEM grid.

Figure 11 (a) shows a visible absorption spectrum for an Au NP/CdSe NR/polymer alternating four-layer film. It shows an absorption peak at 550nm, which is close to the absorption peaks of Au NP/PMMA monolayer film (557nm). This unique technique is very interesting for fabrication of complex and functional nanostructures for further applications, such as photovoltaic device. Figure 11 (b) shows a representative TEM image of Au NP/CdSe NR/polymer alternating two-layer film. The Au NPs are organized in a monolayer manner in the first layer. Since the contrast of CdSe NR is much lower than metallic Au NP, it is not easy to see a continuous monolayer film of the CdSe NR above the Au NP layer; however, from the domains without Au NP the monolayer of CdSe NR can be clearly observed. The up-left part of the film (Figure 12b) is supported by carbon of TEM grid, and most part of the film is unsupported.

2.2.4 AFM Nano-indentation of NP/polymer monolayer arrays

By incorporation of NPs, polymer films can be made stronger and desired electrical and optical properties are able to be implemented into the material. In the experiment that follows we briefly discuss the characterization of the mechanical properties of Au NP/PMMA monolayer arrays by nano-indentation with AFM tip.

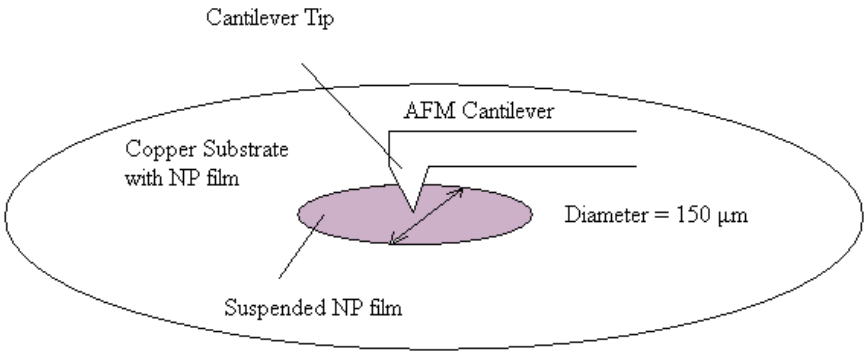

Figure 12 Schematic diagram showing nanoindentation of Au NP/PMMA film with AFM tip.

Au NP/PMMA monolayer array films were made by evaporation induced self-assembly at fluid interface. The films were then transferred onto a copper substrate, with a single-hole (150μm in diameter) in the center. The film was laid over the hole where nano-indentation could be performed. The film thickness was found to be approximately 100nm which was measured by an ellipsometer and verified by a scratch test using the atomic force microscope. Using an atomic force microscope to perform the nano-indentation, the deflection in the middle of the suspended film was found. The force was found using the spring constant of the atomic force cantilever beam. The young's modulus can be calculated using the equation for a circular plate under a center point load, assuming there is no residual stress in the film and the poison's ratio is between .35 and .45 which is typical for most polymeric materials. The young's modulus of the film was found the be between 7.80 and 8.58 GPa.

$$E = \frac{3Fa^2(1-\upsilon^2)}{4\pi\omega h^3}$$

Equation-1

where ω is the deflection, F is the force applied to free-standing film, a is the diameter of AFM tip, υ is the poison's ratio of PMMA, and h is the film thickness.

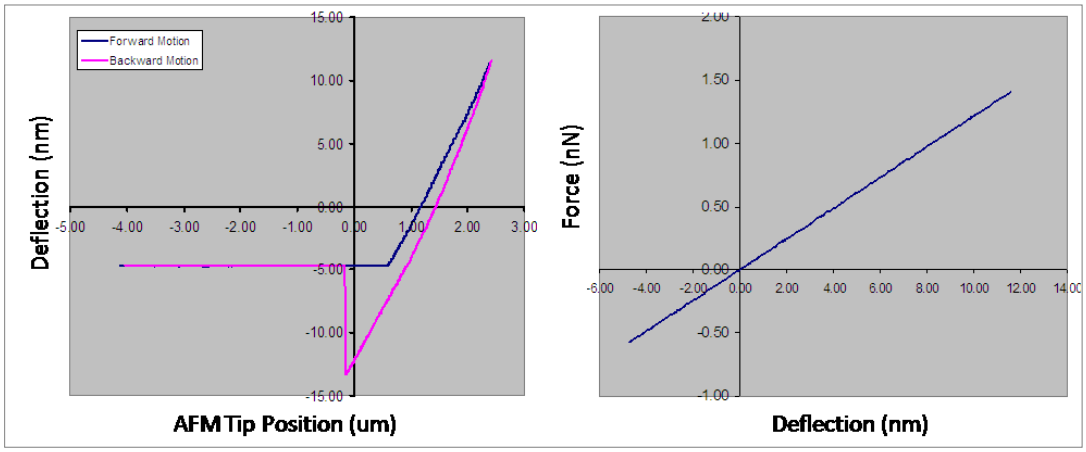

Figure 13 a) Deflection of the film with the AFM tip position as the tip contacts the film and then retracts. b) Force vs. deflection of the film. It is linear since the deflection in the film is very small.

Comparing the determined young's modulus of the NP/polymer film and comparing it to that of the bulk polymer PMMA by itself, which has a young's modulus of around 1.8 to 3.1 GPa, one can see that the NPs increase the film's robustness significantly.

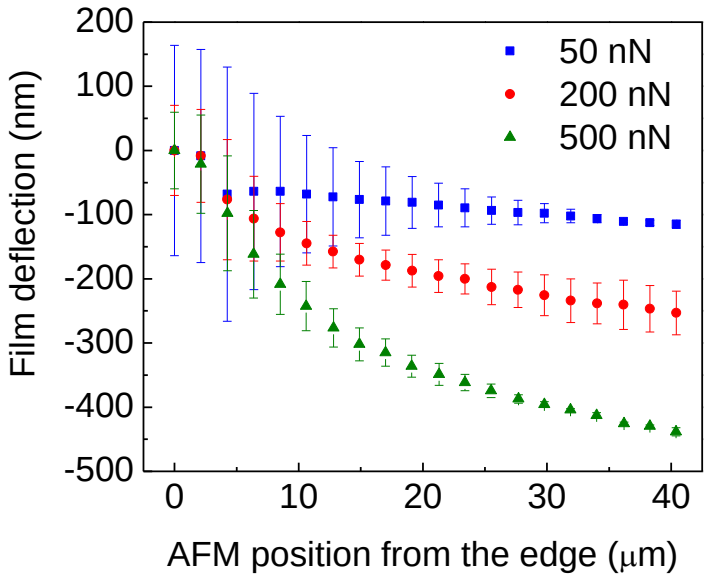

Figure 14 Deflection vs. position of the film. Different traces are corresponding to different forces applied.

2.2.5 Patterning

The ultra-thin monolayer NPs/PMMA films supported on a substrate were patterned by electron beam lithographic technology using a JEOL 848 scanning electron microscope (SEM) with NPGS-1 lithography software. Exposure doses were in the range of 100 to 200 μC/cm^2 at 40 keV. The films were developed in Methyl isobutyl ketone (MIBK) diluted 1:3 with isopropanol for 60 seconds.

Since the monolayer NPs are embedded in a polymer framework, this monolayer NP fabrication technique is promising to be combined with other lithographic techniques to make complex monolayer NP patterns which are very interesting for microdevices. For example, these ultra-thin films were successfully patterned by electron beam lithographic technology using a SEM. The optical microscope image (Figure 15a) shows well-defined

concentric rings of 0.25, 0.5, 1, and 2 μm linewidth. The width for the narrowest straight line is 100nm, although it is not well developed as the 200nm and 300nm width lines. Furthermore, the polymer can be replaced by other hydrophobic lithographic and functional polymers for some specific applications and functionalities.

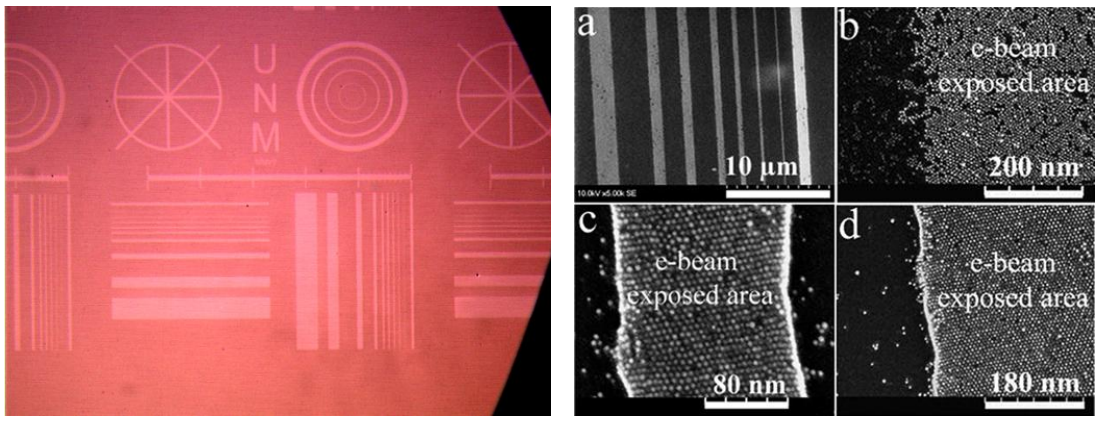

Figure 15 a) Nomarsky micrograph of part of the e-beam patterned ultra-thin Au NP/PMMA film on a silicon substrate b) SEM image showing the two modes of E-beam lithography patterning of Au NP/PMMA monolayer array.

For many anticipated uses, it is desirable to pattern the NP arrays in arbitrary shapes, spanning a range of length scales. PMMA can be used as either a positive or negative e-beam photoresist. Here we demonstrate two types of negative mode patterning (e-beam exposed regions are preserved). NP/PMMA monolayers supported on Si (100) wafers or glass slides were patterned using a JEOL 848 SEM (40 keV acceleration voltage) with NPGS lithography software. Two exposure dose ranges were investigated. For the range 300 to 3000 $\mu C/cm^2$, we find that NPs in the exposed regions are insoluble in hexane (5 min immersion) relative to the unexposed regions (Figs 15 right a,b). Presumably this dose strips the dodecane-thiol groups as reported for Au NPs assembled on solid supports[71] – the interface in this case is somewhat diffuse, and some Au NPs are dissolved from PMMA in the exposed areas (PMMA remains in both areas). For doses

ranging from 10000 to 30000 $\mu C/cm^2$, PMMA is cross linked to become toluene insoluble,[73] serving as a negative resist when developed in toluene (Figure 16c,d). In this case the edge roughness is reduced and the Au NPs are largely retained in the exposed areas.

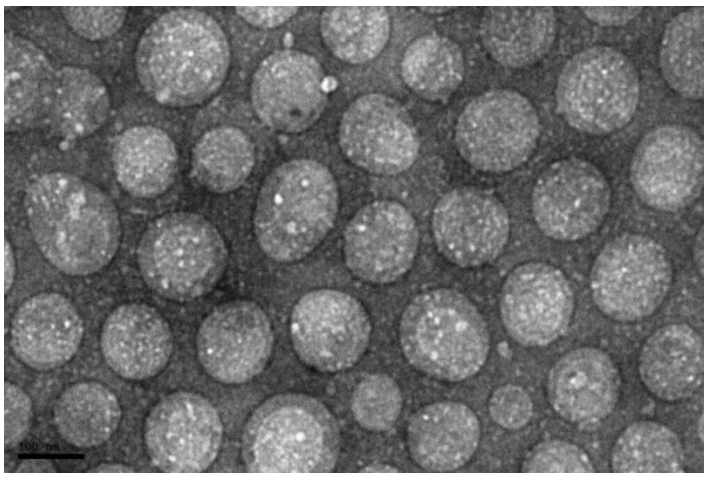

Figure 16 TEM image of polystyrene-co-polyacrylic (PS-co-PAA) acid pattern formed by interfacial assembly. The dark area represents the polystyrene phase while the light area refers to the poly (acrylic acid) phase.

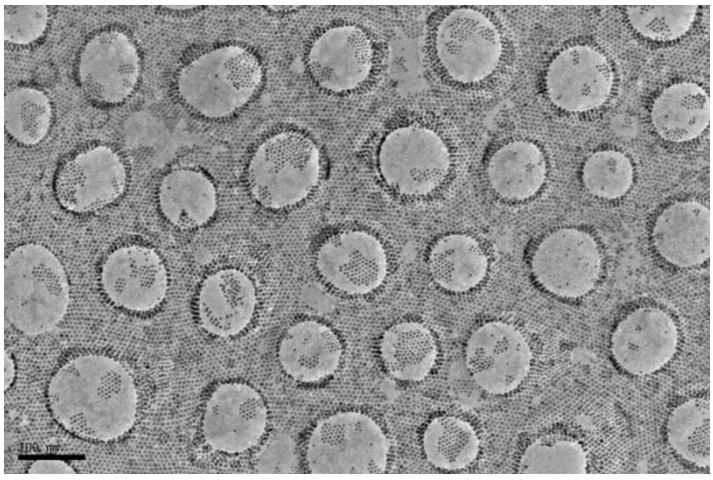

Figure 17 Au NP/polystyrene-co-poly (acrylic acid) monolayer array. The dark area represents the polystyrene phase while the light area refers to the poly (acrylic acid) phase.

Other than lithographic patterning, block co-polymer templates have also been used to pattern the NP array. With different hydrophobicity regarding the two blocks of co-polymer, it formed reverse-micellar structure on the air/water interface. PAA phase

are surrounded by PS phase. Along the Z direction, it appears as a cylinder structure (Figure 17).

While Au NPs are co-assembled with the polymer, it's observed that the NPs are confined in the PS phase (PAA phase in circular shape, with diameter about 100nm, in a hexagonal packing geometry), still remaining as an ordered monolayer array (Figure 18).

By changing the molecular weight of each phase of co-polymer, we were able to easily change the dimension of PS and PAA domains. The significance is that NPs are highly ordered, indicating this can be an alternative high-throughput route to lithographic patterning of NP array.

2.3 Electron Transfer / Transport in NP / Polymer Monolayer Arrays

NP (NP) / Polymer composites exhibiting advantageous optical, electrical and mechanical properties are of interest and under intensive investigation for a variety of applications. Recently we have extended our interfacial self-assembly process to the conjugated polymer system. Poly- (3-hexylthiophene), or P3HT was selected as the matrix material, as it's the most often used hole-transport material in organic photovoltaics (OPV),[74] organic light emitting diodes (OLED),[75,76] and organic thin film transistors (OTFT).[77]

One such application utilizes the polymer as the sensitizer for a nanoparticle solar cell, harvesting light and transferring electrons to the inorganic semiconductor nanoparticles. However, this system is quite different from the intensely studied dye-sensitized nanoparticle solar cells. Therefore work needs to be done to investigate charge

transfer in the polymer/nanoparticle composite. The electron transfer is monitored using ultrafast pump-probe spectroscopy measuring the mid-IR absorptions of the injected electron and polymer polaron. We investigated differences in the rate of transfer depending on the identities of the two components in the composite. Interfaces govern important electronic processes, such as energy and charge transfer, which ultimately determines device functionality and efficiency.

By transferring the NP/polymer films onto discovery platforms with pre-deposited interdigitated electrodes (by "lift off" with a shadow mask almost identical in size to the electrode area), electron transfer at the metallic NP/polymer interfaces and electron transport across the composite films have been studied through a combination of electrical and spectroscopic techniques.

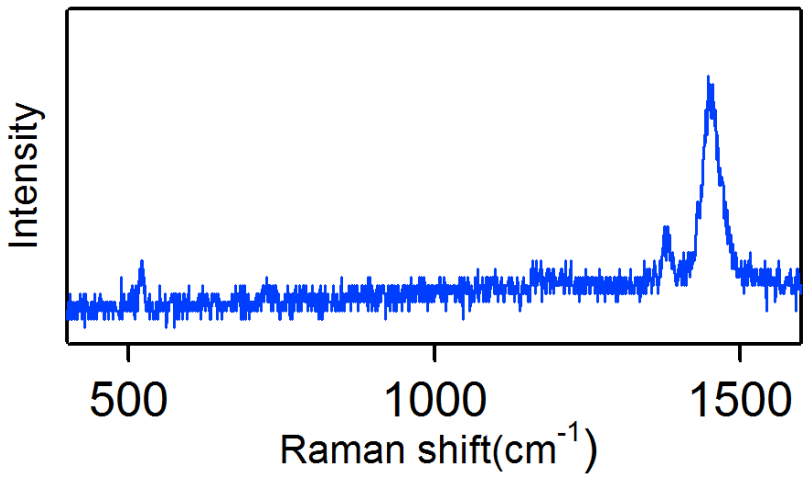

Figure 18 Typical Raman spectrum of composite film on interdigitated electrodes excited at 488 nm: there are three peaks at ~520 cm^{-1}, ~1380 cm^{-1} and ~1450 cm^{-1}.

Figure 4 shows a typical Raman spectrum of composite film on interdigitated electrodes excited at 488 nm. There are observable three peaks at ~520 cm^{-1}, ~1380 cm^{-1} and ~1450 cm^{-1}. Peaks at ~1380 $cm^{-1}$and ~1450 cm^{-1} have been assigned to C-C

stretching mode and C=C symmetric stretching mode of P3HT. The ~520 cm^{-1} peak is tentatively assigned to the Si substrate. This peak didn't show up in a composite film transferred to a cover glass and this peak disappears due to existence of Au nanoparticles in the sample when the scanned region moves to electrode.

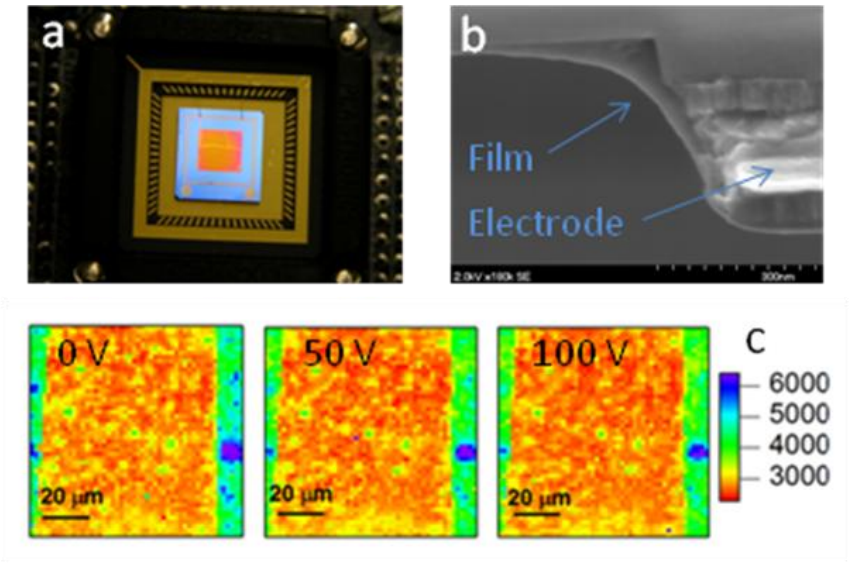

Figure 19 Photograph of the patterned Au NP/P3HT composite film transferred onto discovery platform and wire bonded to sample carrier (a); cross-sectional SEM image showing Au NP/P3HT composite film conformal to the electrodes (b); scanning Raman spectrascopic image (C=C stretching mode of P3HT) on a selected area across the interdigitated electrodes under different bias (0V, 50V, and 100V) (c). The color mapped comparative intensity of Raman spectra in arbitrary units. Green is referred to the electrode area.

The discovery platform was wire bonded to a carrier, which allowed for bias voltage to be injected through the device. Raman Spectroscopy was then used to measure variances in scattering intensity as an indirect method of detected charge movement across the device. Three Voltages: 0 V, 50 V, and 100 V were used on the device sample by a function generator and amplifier. A laser of 488 nm generated by an Ar-Kr ion laser head was used to excite the sample. The Raman scattering light was then collected by a sensitive EMCCD. For a single Raman spectrum, acquisition time was ~500 ms.

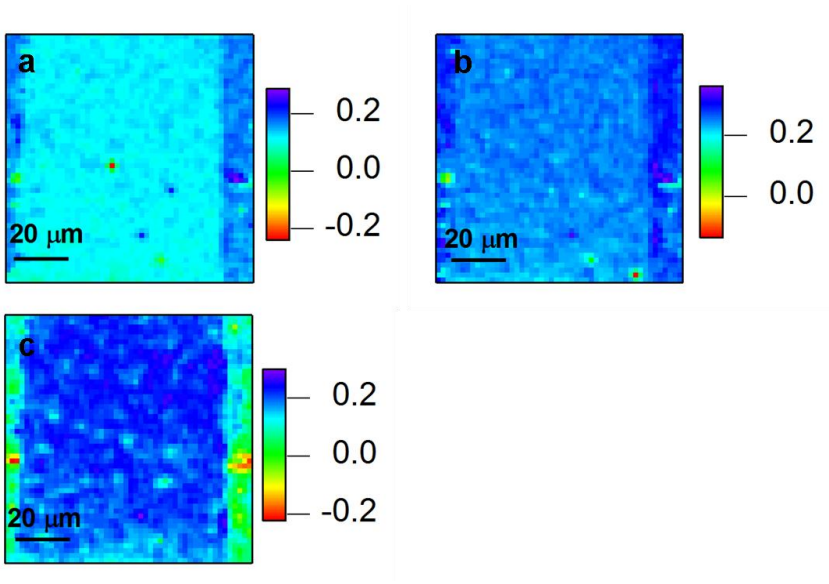

Figure 20 Difference image of C=C mode scan: a) 0-50 V; b) 0-100 V; c) 0-150 V

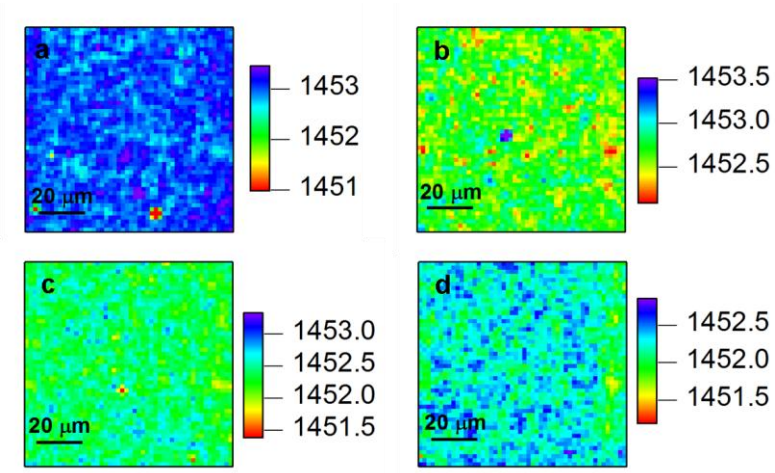

Figure 21 shows the Raman intensity images of the dominant peak, C=C stretching mode of P3HT on the discovery platform sample under different voltages with excitation 488 nm to understand charge transport. The scan range was set to be 100 µm and the region we selected purposely to cross two of the Au electrodes. The intensity drop of these images shown may be due to a photo degradation issue, since the same region exposed to high power intensity laser ~10^4 W/ cm^2 and air. The features here clearly show two electrodes surrounding a nearby region.

Lower intensity regions are indicated as red color and assigned to Au electrode because of the less P3HT in these regions; high intensity region are denoted as blue color and assumed to be between electrodes due to thicker composite layer.

We were able to successfully view changes in intensity of the C=C mode of the film indicating that there is some sort of charge movement on the localized level. Although we only have a cursory data set, it seems that we can conclude that bias-induced chemical changes occur at the molecule-electrode interface possibly from charge injection.

2.4 Conclusion

We have developed a universal, facile and robust method to prepare supported and unsupported ultra-thin films of monolayer nanoparticles that can serve as fundamentally interesting model systems for catalytic evaluation, optical investigation and magnetic study of metal, semiconductor and bimetallic nanoparticles, and this process is technologically important for the fabrication of ultra-thin monolayer or sandwiched multilayer film materials for nanotechnology applications such as optical devices, photovoltaic device, sensors, nano-catalysis, and magnetic storage. This kind of film can be easily transferred onto various substrates, such as glass slides and silicon wafers, and sticks very well on the substrates. The nanoparticles are closely packed in a monolayer manner, and are strong and stable enough to partially stand without any support. This facile method can be extended to various kinds of hydrophobic nanoparticles, such as metallic Au nanocrystals, semiconductor CdSe nanorods and nanoparticles, and magnetic FePt nanoparticles. Binary superlattices created may have application in electrochemical catalysis or fuel cells.

Transparent polymer matrix allows the optical properties of nanoparticles to be preserved. With AFM indentation experiment, we applied the Reiner theory and

estimated the Young's modulus of the composite film suspending on holey substrate, which explains the robustness of the free-standing film.

By extending to other polymers, both the structure and function of this composite material have been enriched. In the co-assembly of nanoparticles and block copolymer, we were able to control the distribution of metal nanoparticles inside polymer thin films. We investigated both the depth profile and the in-plane spatial correlation of gold nanoparticles in an asymmetric polystyrene-b-poly (acrylic acid) block copolymer film. These copolymer films self-assemble into alternating, nanometer-sized domains that are selectively decorated by thermally evaporated metal nanoparticles to form metal/polymer composites. More importantly, the ultra-thin nanoparticle films supported on substrates were successfully patterned by e-beam lithography while using a photoresist as the polymer matrix material. Moreover, we transferred the Au nanoparticle/P3HT array onto interdigitated electrodes and studied the Raman spectroscopy as a indicator of electron transfer within the conjugated polymer film with or without applying potential bias.

Chapter 3. In-Situ and Reflectivity Grazing-Incidence Small-Angle X-Ray Scattering Study (GISAXS) of Interfacial Assembly of Nanoparticle/ Polymer Monolayer Array

3.1 Introduction

Time-resolved Grazing Incidence Small Angle X-Ray Scattering (GISAXS) was used to investigate the structural development during evaporation induced self-assembly (EISA) of Au nanoparticles with a homopolymer on the air/water interface. The assembly of nanoparticles took place at air/polymer interface in the confined area determined by polymer solidification following spreading of organic phase. Symmetric scattering peaks composed of two scattering angles indicating different packing fashions were observed as transient phase. From in-situ GISAXS only the sharp peak related to hexagonal close-packing was preserved by the end of EISA. We further discuss the reflectivity GISAXS measurement revealing preferential residence of a monolayer array of Au nanoparticles on top of the thin polymer film.

Nanoparticle (NP) array as ordered 2D quantum solids are of interest for a variety of applications due to quantum size effect as well as easiness and universality based on the solution processability.[78,79] Metallic[80], semiconductor[81] and magnetic NPs[82,83] have been synthesized through colloidal chemistry and assembled[61,69,84-87] into nanostructures for fluorescent biomedical imaging[88], photovoltaics[89], sensing[90] and catalysis[91]. In many

cases, it still remains as a challenge to couple this nanostructure to traditional lithographic nanofabrication to create functional devices[92] for collective electrical/optical property. An obvious obstacle resides at that the assembly often takes place on specific substrates[72] thereby the transfer to other surfaces is not allowed.[61] In comparison, in interfacial EISA polymer molecular layer acts as a floating substrate thus no repulsion exists between NP and water surface.[93] NP array supported by thin yet robust polymer film transferred from fluid interface is insensitive to substrate material and topography. Principally this method can be extended to any hydrophobic NPs that are miscible with the polymer. Moreover, the polymer matrix further lends us a variety of functions for applications such as hybrid solar cells[89] or organic light emitting diodes (OLEDs)[94]. If not needed, in some cases, the polymer layer can be further etched by plasma or wet chemical methods.

Intensive study of NP/polymer interfacial assembly indicates this process is different from pure NP array assembled on water surface.[63] Unlike Langmuir-Blodgett method,[58] this is no need here to use a moving barrier to pack the NPs by pushing to a threshold surface pressure. On the other hand, compared to assembly on evaporating water drop, herein there are no NP islands formed as transient phase[63]. Evaporation of solvent can be divided into different stages and there was a transient phase indicated by the secondary broad diffraction peak (see figure 1). X-ray reflectivity measurement was performed and the formation of layered NP/polymer thin film on the air/water interface was verified. This further converge the interfacial assembly to drop-casting method on solid substrate, however, existence of residual solvent until the end of NP assembly (see M1 in supporting information) exclude the necessity of excess amount of capping ligand for surface dewetting[72].

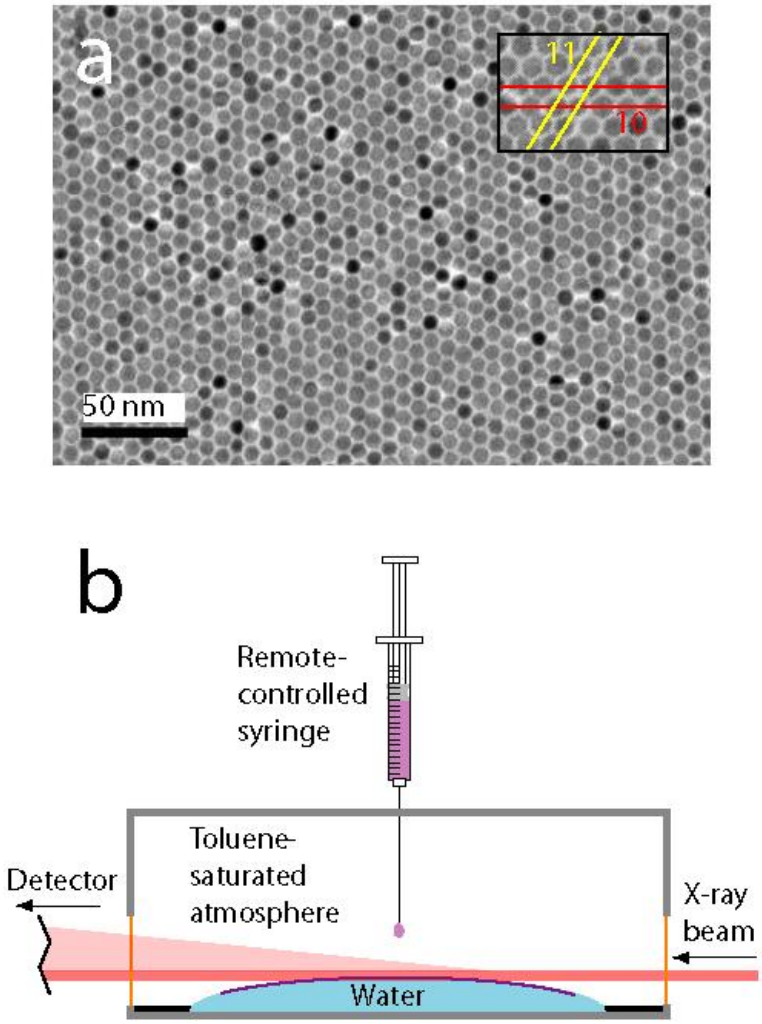

Figure 1 TEM image of monolayer Au nanoparticle/PMMA array assembled on fluid interface (top) and a sequence of GISAXS image captured for monolayer array on water surface at 10, 40, 60, and 80sec after release of oil drop (bottom).

3.2 GISAXS experiments and discussion

In-situ GISAXS study was performed in beam station 8ID-E of advanced photon source in Argonne National Labs. The X-ray wavelength was set to 0.1675nm, with a beam size of 100×200μm. To accommodate the X-ray footprint, a curved water subphase was prepared by trapping a small amount of de-ionized water (ca. 2ml) on a homemade substrate. Plasma treated Si wafer was first cleaned up with acetone, methanol and IPA

with the aid of sonication. Then we wrapped the edge of the 3×3 cm wafer with the Parafilm in order to make a steep contact angle. This Parafilm wrapping was annealed in oven to further promote adhesion to substrate. Dispense of oil drop was operated by remote control on a motor driven syringe and synchronized to the GISAXS CCD imaging system. A saturated atmosphere was designed to slower down the solvent evaporation thus the temporal evolution of NP assembly can be captured. This was achieved by putting a solvent reservoir aside to the sample in a closed chamber. Nevertheless, a water reservoir was also used to maintain the water level so that we do not lose the collimation with the X-ray. Kapton window on two sides of the chamber allowed X-ray transmission.

GISAXS diffraction images were acquired for every 10 seconds to monitor the nanostructure formed by evaporation induced self-assembly on fluid interface. The integration time for each cycle was 5 seconds and the CCD detector was set to sleep for another 5 seconds. The NP/polymer oil drop was released from the second cycle so that a background image can be taken as control. For comparison, we conducted the in-situ experiment for solutions made from different NP and polymer concentration.

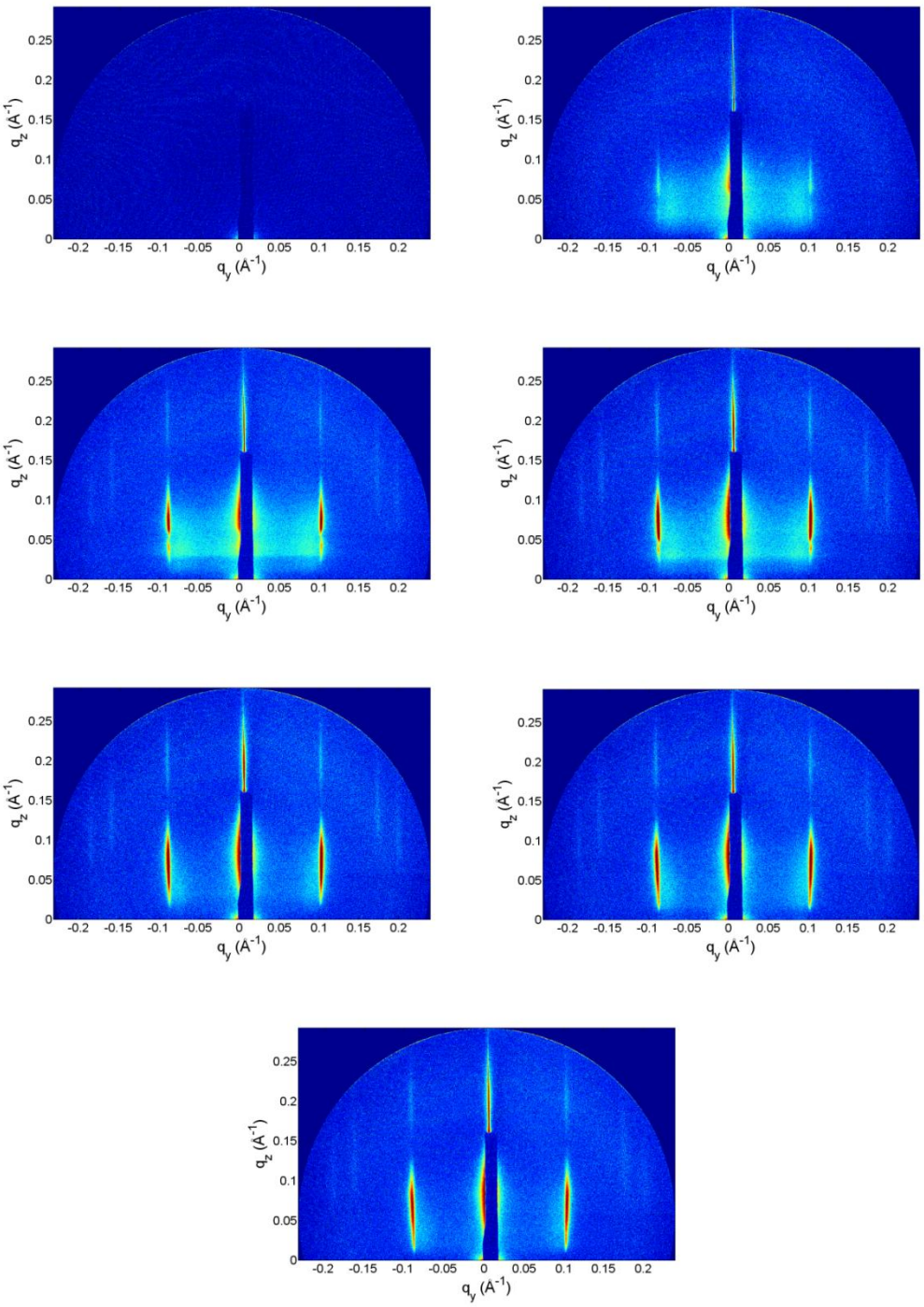

Figure 2 A sequence of GISAXS image captured for monolayer array on water surface at 10, 40, 60, and 80sec after release of oil drop (polymer: nanoparticle =1:1).

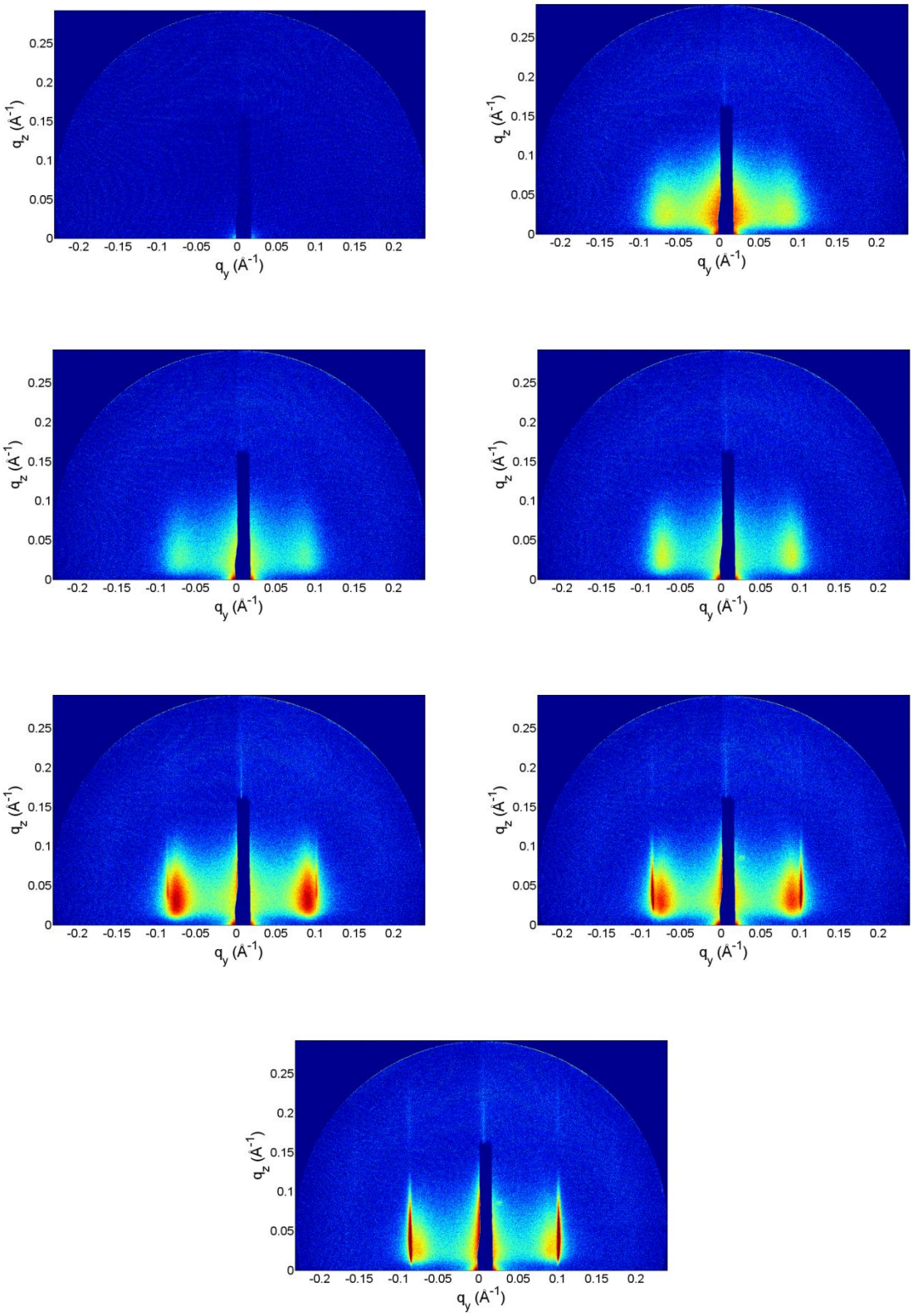
0.25
0.2
0.15
0.1
0.05
0
q_z (Å^{-1})
-0.2 -0.15 -0.1 -0.05 0 0.05 0.1 0.15 0.2
q_y (Å^{-1})

Figure 3 A sequence of GISAXS image captured for monolayer array on water surface at 10, 40, 60, and 80sec after release of oil drop (polymer: nanoparticle =2:1).

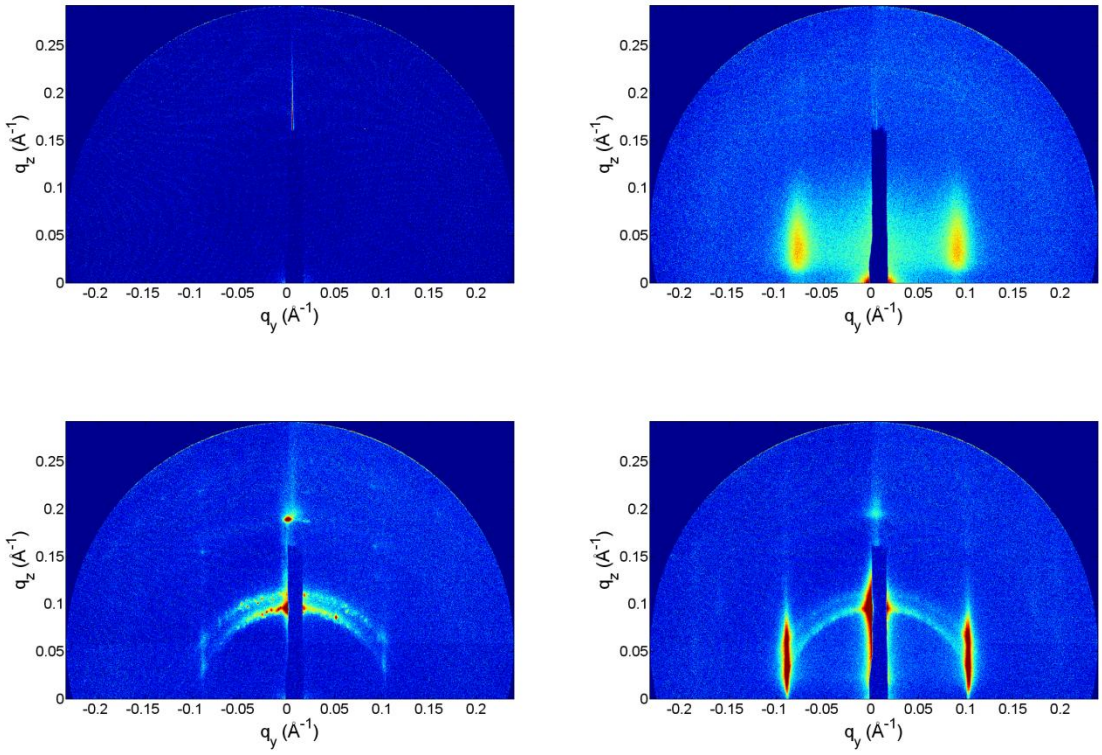

Figure 4 A sequence of GISAXS image captured for monolayer array on water surface at 10, 40, 60, and 80sec after release of oil drop (polymer: nanoparticle = 1:2).

The self-assembly of the close-packed NP/polymer monolayer array was based on the procedure we recently reported. For the first step, dodecane-thiol protected Au NPs (6nm in diameter) were dissolved in toluene containing polymer (PMMA, M_w = 996,000). Second, one drop (about 6 µl) of the NP/polymer/Toluene solution was dispensed quickly by a syringe onto the water surface. In the typical interfacial assembly process, the droplet immediately spread into a film of ca. 1.5 cm diameter on the water surface. Solvent evaporation drives NP self-assembly followed by solidification within polymer, the residual solvent interface maintaining the required NP mobility needed to achieve a highly ordered low defect NP monolayer. A NP/polymer thin film was visible floating on

the water surface after the GISAXS characterization. A TEM image of a representative film was taken and the ordered structure can be verified as shown in figure 1.

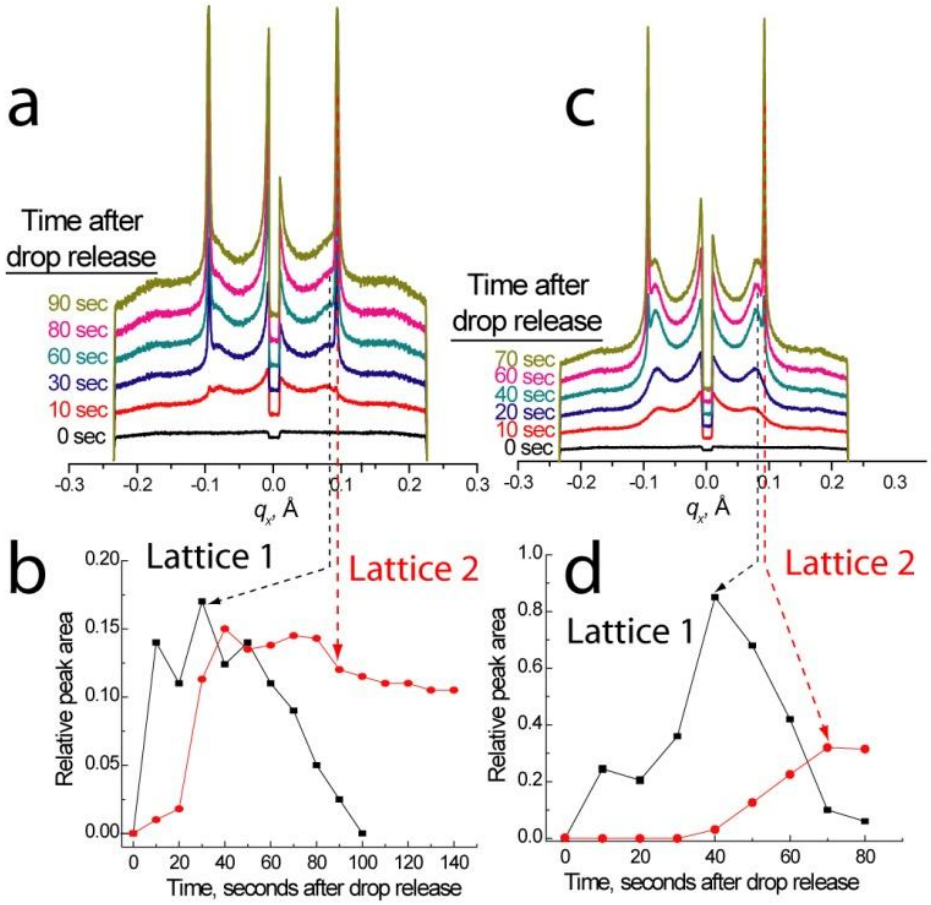

Figure 5 Line scan of GISAXS images at different time point for NP/polymer assembly on fluid interface (a, NP:polyemr =1:1; b, NP:polymer =1:2). Temporal evolution of fitted peak area (lattice 1, liquid-like packing; lattice 2, hexagonal close-packing) of for NP/polymer assembly on fluid interface (c, NP:polyemr =1:1; d, NP:polymer =1:2).

From the sequence of GISAXS images captured we find the diffraction pattern started to show up from 40 seconds after release of oil drop (see figure 1). The diffraction lines were broad at the beginning and became well defined after another 40 seconds. Line scan at constant q_z clearly show the evolution of diffraction peaks. What's interesting is that while the polymer concentration is increased there are two diffraction peaks observed in

the course of assembly and eventually the second peak disappeared (Oriented diffraction lines come from the curvature of water subphase).

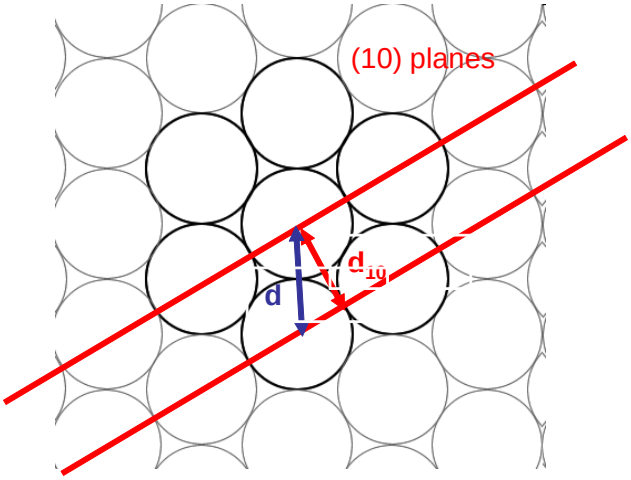

Figure 6 Two different packing style of NP array on air/liquid interface

Polymer acts as intermediate between hydrophobic NPs and hydrophilic water surface. Although the particle-particle interaction still plays an important role as well as the evaporation kinetics, the absence of particle-interface repulsion further rules out the formation of islands. Assuming that the majority of solvent evaporates during the solidification of polymer film perimeter, residual solvent trapping in polymer matrix continues to escape, thus the liquid phase of NP assembly could maintain for a quite long period (>20s, see Figure 2). It's believed that in polymer rich case, the solvent took longer time to evaporate so the transition phase lasts longer during the self assembly. Further calculation of the position of the double peaks found that the $q_{//}$ratio (broad peak at ±0.0945; sharp peak at ±0.0809) is exactly 2/ sqrt (3). The 1st broad peak with smaller $q_{//}$ corresponds to the interparticle distance of a disordered packing (liquid like). As the particles are being rearranged to form hexagonal packing, the scattering from (10) planes (Bragg diffraction) grow thereby the 2nd sharp peak starts to show up. As time evolves, the disordered liquid-like peak becomes weaker and the Bragg peak becomes stronger,

meanwhile the higher order peaks (20) start to show as the ordering gets better. Domains/clusters of random orientations over the X-ray footprint of illumination mean that (11), (21) should also exist. Two kinds of packing coexist for about 20-40seconds. Finally as all (or most of) particles are ordered, the broad liquid-like peak disappears. This leads to a very important finding of lattice growth mechanism: NPs get closer first to form a disordered liquid-like close-packing, and then particles rearrange to form domains of 2D hexagonal packing with interparticle distance kept constant, instead of forming 2D ordered packing in the very beginning of the kinetics. We did not observe the position shift and merging of broad peak into the sharp Bragg peak, further indicating that the broad peak and the Bragg peak arise from different packing style.

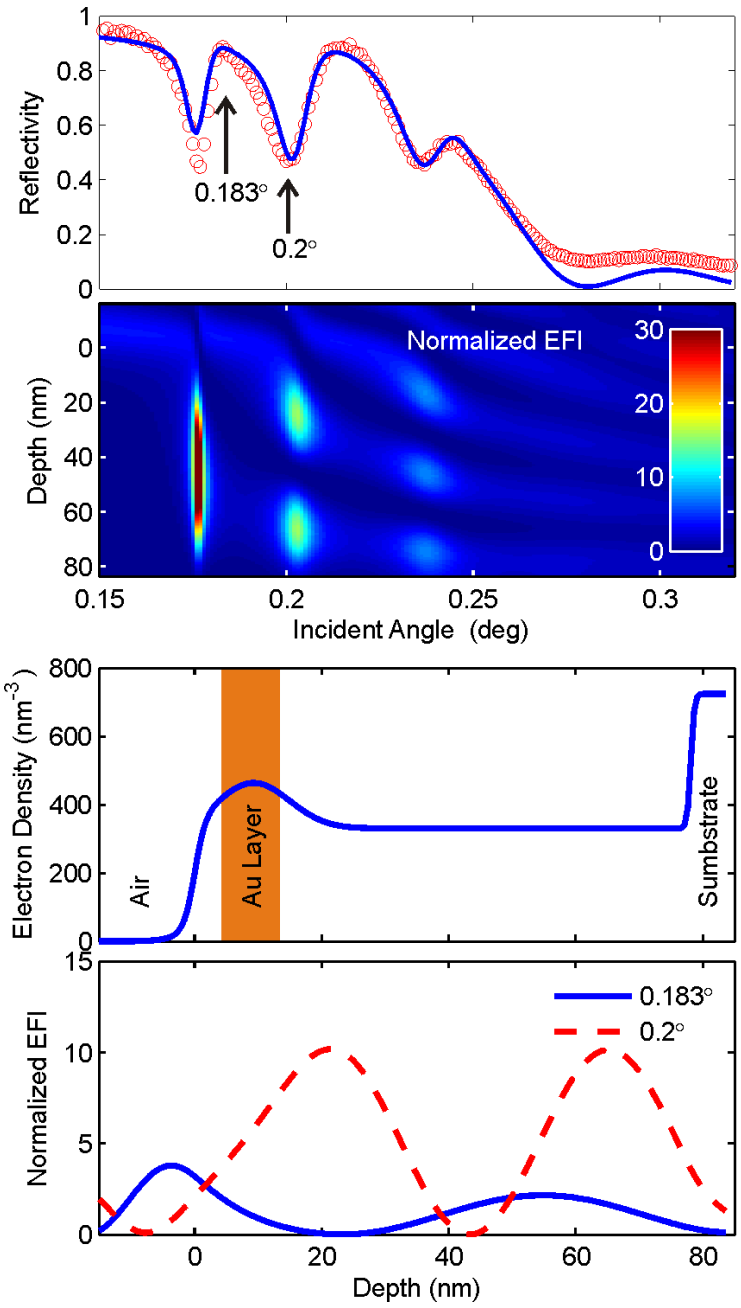

Figure 7 Reflectivity measured for NP/polymer monolayer array transferred onto Si substrate and fitted EFI indicating the NP depth profile.

Monolayer of NPs together with solid substrate could be treated as a 2D X-ray waveguide[95]. To determine NP depth profile, a monolayer NP/polymer sample was prepared by interfacial assembly and the thin film was transferred to a piece of Si wafer

for X-ray reflectivity measurement. The thickness of Au NP/polystyrene film has been characterized by ellipsometry to be 80nm. X-ray reflectivity was scanned from 0.16 degree to 0.25 degree of incident angle, and reflectivity data show oscillation peaks. The first peak at 0.183 degree is corresponding to the critical angle of polymer matrix, while the reflectivity valley at 0.2 degree is assigned to the critical angle of Si substrate.

Based on the reflectivity fitting, the electric field intensity (EFI) distribution is calculated as functions of incident angle and film depth. White dotted line is the position of the NP monolayer, while red dotted line indicates the incident angles for GISAXS measurement. Since EFI is lower at 0.183 degree than at 0.2 degree, the scattering from Au NP monolayer in the GISAXS image is slightly weaker at 0.183 deg. This is confirmed by GISAXS images. The total film thickness is found to be 78nm, which is in great consistence with measured result from ellipsometry; au layer is found to locate at 9.3nm below the top surface with a vertical Gaussian distribution of σ = 5.7nm. This fitted electron density profile clearly show that Au NPs are almost at the top of film.

3.3 GISAXS of binary nanoparticle superlattices

Recent work on nanoparticle superlattices, and notable recent publications by Murray et al. on binary nanoparticle superlattice (BNSL) geometries[68], represents a new step forward in soft-colloid processing and the field of "bottom-up" or directed-assembly in general. Colloidal nanoparticle superlattices can theoretically be used to tailor the directed-assembly of scalable, arbitrarily complex and interconnected multi-layered structures composed of a multiple particle types each having custom chemical,

biologically or environmentally-responsive, electronic, or optical properties[68,96]. Tuning the sizes, shapes, and particle compositions in BNSLs has been shown to be a fast and inexpensive path for interface-driven order in NP colloids, and many lattice geometries have been demonstrated corresponding to various ratios of nanoparticle radii (for spherical particles) or variety in the NP shapes. Colloidal nanoparticle lattice geometries can be partially predicted by classical crystallographic space-filling and space-group theory, while simulation of soft-particle colloids, clustering and order analysis, FFT plots, and GISAXS experiments and simulations are all valuable characterization tools which can yield insight into underlying physical processes and possible device design avenues. We demonstrate a matching of experimental and simulated GISAXS intensity and FFT plots for a BNSL formed by EISA of 14.5nm diameter Fe_3O_4 and 5.3nm diameter Ag particles in a toluene/PMMA solvent. Linear analysis (plots across row or column) of the GISAXS intensity data can be used to match theorized structures to experimental structures to verify and characterize particle lattice geometries. The software tools we use for our visualizations, simulated GISAXS[97] and FFT[98] plots are widely available, and demonstrated to be applicable for research involving nanoparticle superlattices, and directed-assembly in general.

In an EISA experiment performed by us, 14.5nm diameter Fe_3O_4 and 5.3nm diameter Ag particles coated with alkanethiol in a toluene/PMMA solvent were deposited by pipette onto a water surface and the PMMA set up into a thin film as the toluene evaporated from the system. The Fe_3O_4 and Ag particles are known to be located at or near the solvent-air interface, and are thought to be trapped from diffusing away from the interface once they reach it because of evaporative/convective flow as the toluene leaves

the system, polar/non-polar hydrophobic-like repulsive mixing interactions between the alkane coatings and the toluene, and capillary forces. GISAXS experiments were conducted on colloids containing just the Fe_3O_4 particles, and colloids containing the mixture of Fe_3O_4 and Ag particles. The structures are thought to form the AB2 crystallographic lattice geometry.

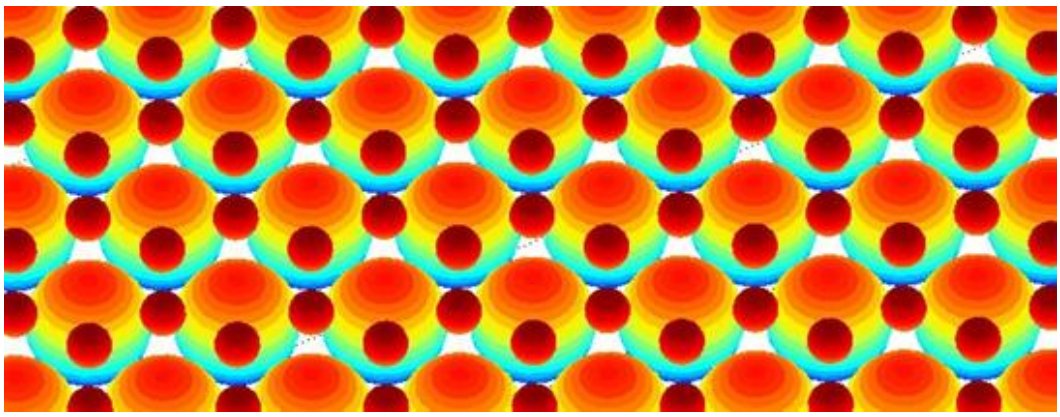

Figure 8 MATLAB 'bubble plot' of the 3D geometry of an AB_2 lattice composed of 14.5nm particles and 5.3nm particles with 1.8nm particle spacing

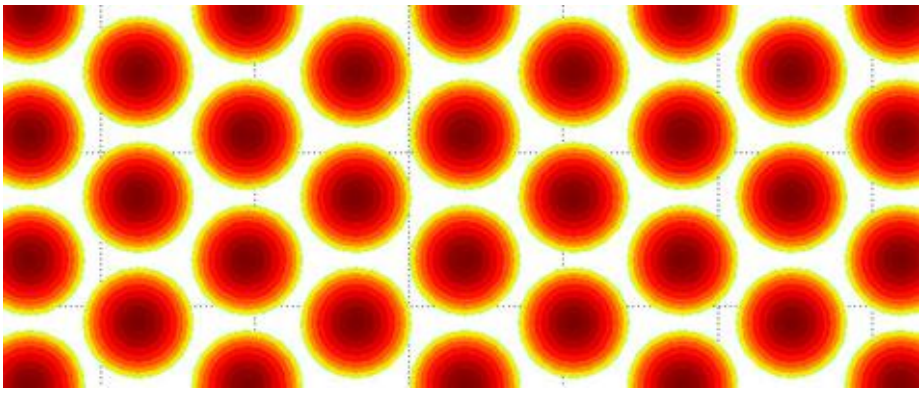

Figure 9 MATLAB 'bubble plot' of the 3D geometry of a hexagonally-packed monolayer of 7.5nm diameter Fe_3O_4 particles with 1.8nm interparticle spacing

Figure 8 shows a 3D visualization (made using MATLAB) of the Fe_3O_4 / Ag BNSL structure, where the particle spacing between each neighboring Fe_3O_4 particle pair has been set to 1.8nm, a reasonable approximation for a such a soft-particle colloid assuming a 12C alkanethiol particle coating. The particle spacing between neighboring Fe_3O_4 / Ag

particle pairs has also been set to 1.8nm under the same approximation. The distribution of the Ag particles is not defined by a single distance, but by their positions in the interstices of the underlying hexagonally-packed lattice of larger Fe_3O_4 particles (according to the AB2 crystallographic unit-cell geometry).

Our goal is to confirm the AB2 lattice geometry and approximate particle spacing via matching of simulated GISAXS and experimental GISAXS. It is instructive to start with the simpler case of the system containing just the Fe_3O_4 particles, shown in Figure 9. Figure 9 represents the approximate geometry that the Fe3O4 particles are theorized to assume during the EISA experiments, whether or not the Ag particles are present.

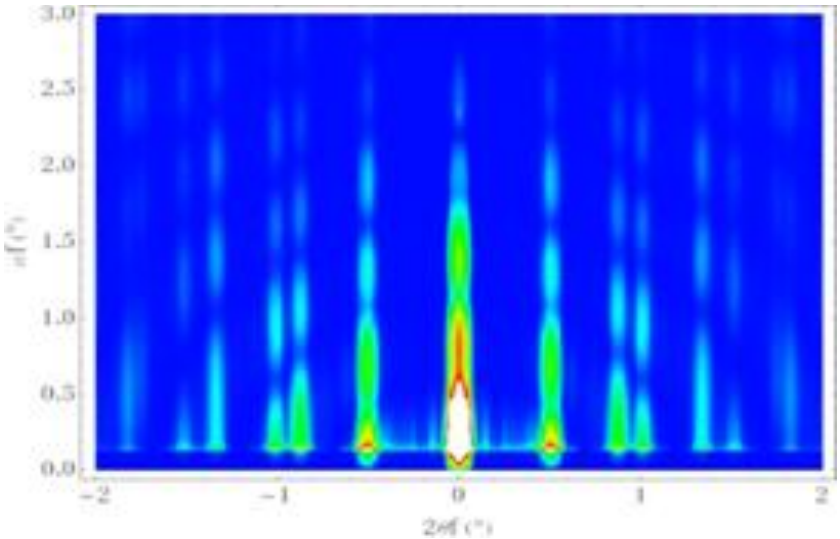

Figure 10 Simulated GISAXS of a hexagonally-packed monolayer of 7.5nm diameter Fe_3O_4 particles with 1.8nm interparticle spacing

Figure 10 is the simulated GISAXS plot for the structure (shown in Fig 9), generated using the NANODIFT extension to Mathematica and some custom C++ scripts by Molecke. A qualitative agreement can be observed between figure 10 and 11, which is the actual plot of experimentally measured GISAXS intensities for this system. The experimental system shows more 'noise' because, presumably because the particles are not in perfect order whereas our simulated particles are set in perfect order. The main

features, such as relative peak heights and intensity gradations, indicate that our simulation represents the correct lattice geometry and approximate spacing between the particles.

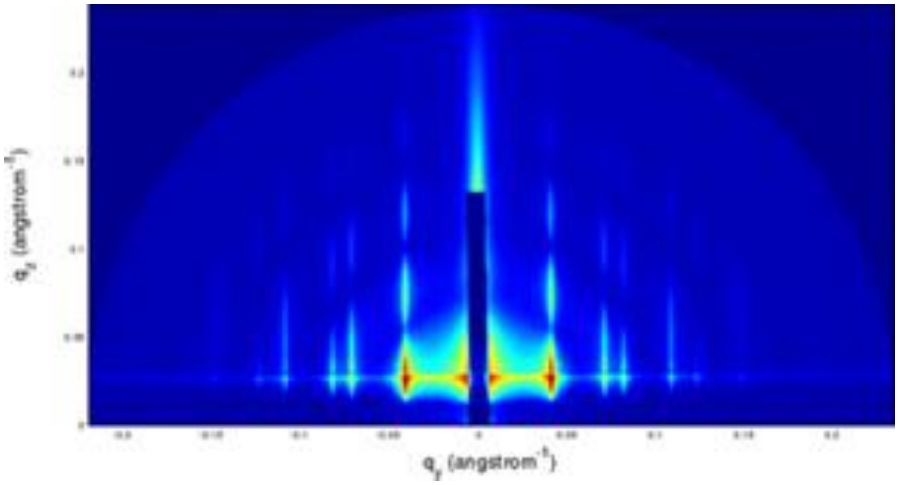

Figure 11 Experimental GISAXS from EISA experiment with alkanethiolated 7.5nm diameter Fe_3O_4 particles in toluene/PMMA solvent

Figures 12 is a row plot of the simulated GISAXS intensities from the simple hexagonally-packed structure (shown in Figure 11), taken at the value of $\alpha f(°)$ corresponding to the bright 'baseline' in the GISAX intensity plot. Figure 13 is a column plot taken at the value of $2\theta f(°)$ corresponding to the first intensity peak right of center. The extension of our graphical analysis to include these linear "cuts" from the GISAXS intensity data allows us better precision and another graphically intuitive tool for matching theorized and experimental geometries and interparticle distances.

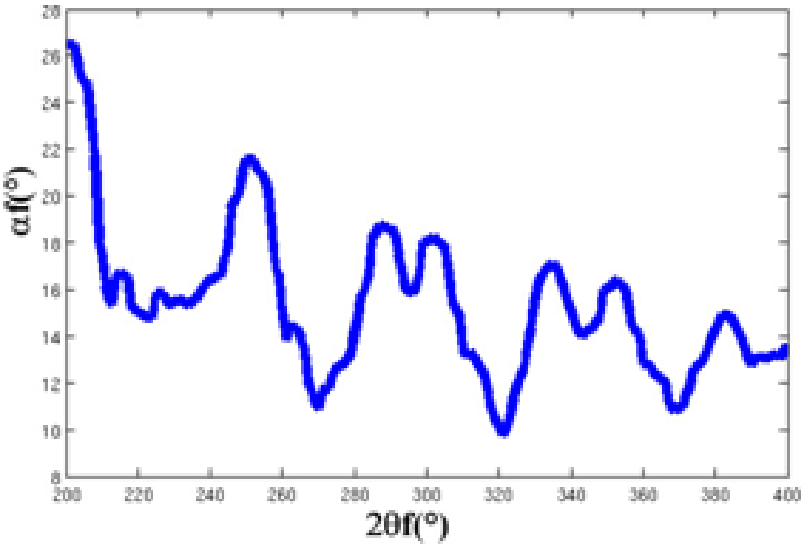

Figure 12 row slice from the 'baseline' of the simulated GISAXS of a hexagonally-packed monolayer of 7.5nm diameter Fe_3O_4 particles with 1.8nm interparticle spacing

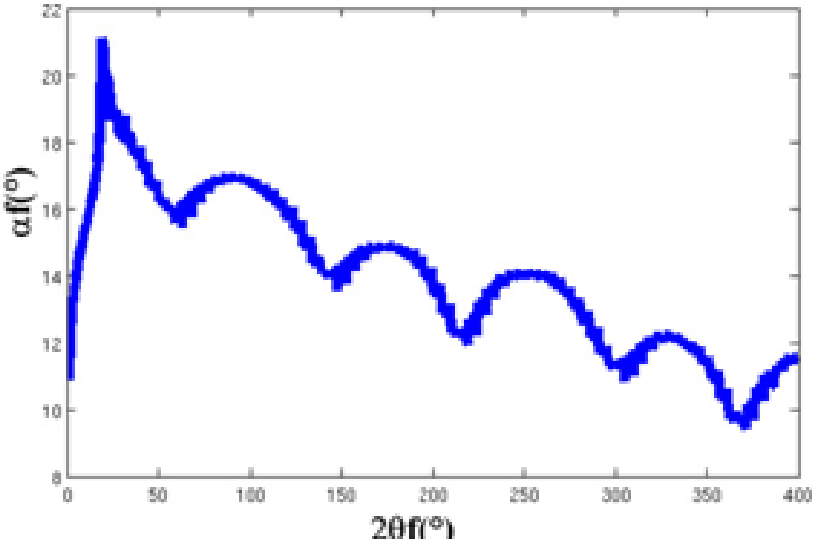

Figure 13 row slice from the 'baseline' of the simulated GISAXS of a hexagonally-packed monolayer of 7.5nm diameter Fe_3O_4 particles with 1.8nm interparticle spacing

Figures 12 and 13 illustrate linear plots through horizontal rows and vertical columns of the simulated GISAXS intensity plot, which are useful for analysis of GISAXS intensities and close comparison between actual and simulated GISAXS intensity plots. Figure 14 demonstrate the geometry of just the Ag particles, where we

have composed the particle coordinates according to the AB_2 lattice geometry with 1.8nm interparticle spacing and we subsequently removed the larger Fe_3O_4 particles. Figure 14 demonstrates that we can also simulated GISAXS intensities from such theoretical particle coordinate sets.

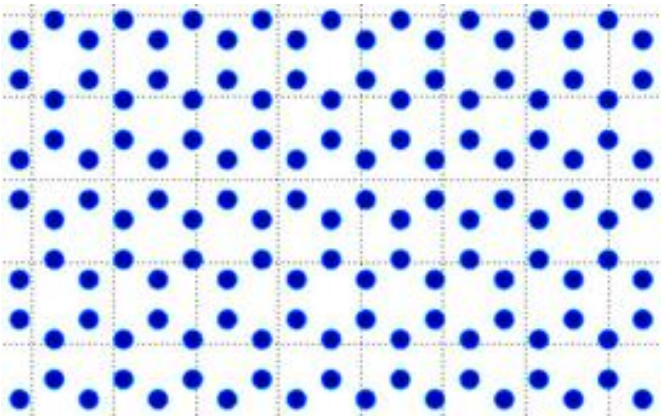

Figure 14 MATLAB 'bubble plot' of the 3D geometry of the 5.3nm diameter Ag particles from an AB_2 lattice with complementary (but removed) 7.5nm Fe_3O_4 particles and 1.8nm interparticle spacing.

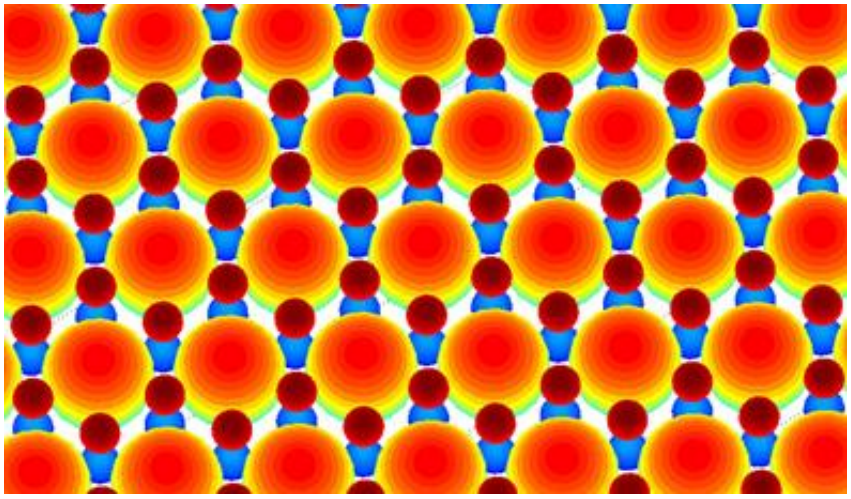

Figure 15 MATLAB 'bubble plot' of the 3D geometry of an AB_2 lattice, with Ag particle layers ABOVE and BELOW the Fe_3O_4 particle layer

Note the distinct lack of intensity gradation in the peaks (in figure 16) characteristic of smaller particle size relative to interparticle spacing. When it comes to characterizing the full AB_2 structure with both Fe_3O_4 particles and Ag particles, we have three choices for how to set up our virtual GISAXS simulation. We can let the layer of Ag particles layer

rest above the Fe_3O_4 particle layer, below the Fe_3O_4 particle layer, or create layers of Ag particles both above *and* below the Fe_3O_4 particle layer. Each yields slightly differing GISAXS plots, and the intensity variations can be used to postulate on the actual physical structure, which may be hard to characterize via TEM in this case because of the potentially multi-layer nature of the structure. Precise matching of structure is achieved via linear analysis of simulated versus experimental GISAXS intensities, as described above.

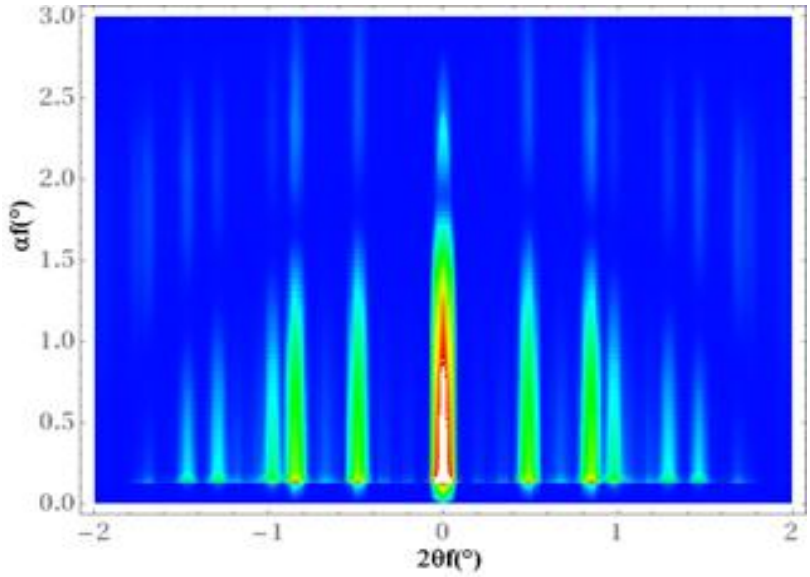

Figure 16 (left) Simulated GISAXS of 5.3nm diameter Ag particles from an AB2 lattice with complementary (but removed) 7.5nm Fe3O4 particles and 1.8nm interparticle spacing.

For brevity we show only the MATLAB visualizations of the structures, Figures 15 and 16, and the best-match simulated GISAXS and experimental GISAXS in this case, Figures 17 and 18, which represent the "ternary" case with layers of Ag particles above *and* below the Fe_3O_4 particle layer.

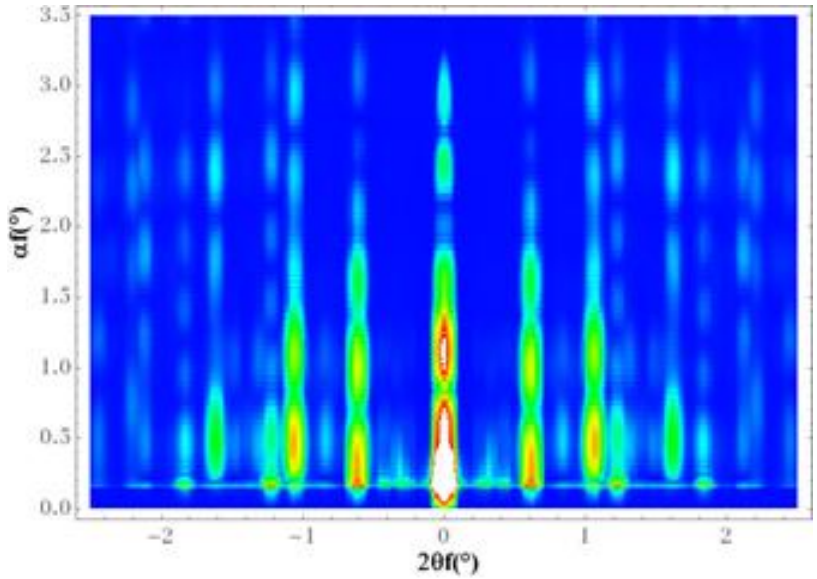

Figure 17 Simulated GISAXS of an AB_2 lattice, with Ag particle layers ABOVE and BELOW the Fe_3O_4 particle layer

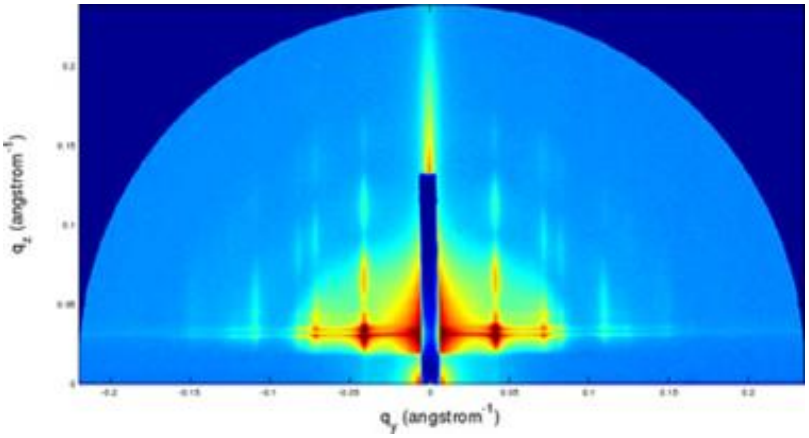

Figure 18 Experimental GISAXS from EISA experiment with alkanethiolated 7.5nm Fe_3O_4 particles and 5.3nm Ag particles in toluene/PMMA solvent

The correspondence between simulated and experimental GISAXS of AB_2 BNSL structures is not quite as close as for the simpler case of a monolayer of hexagonally packed particles, but still close enough that we can confirm that the AB_2 lattice geometry, and we can say that there are most likely layers of Ag particles in the interstices above *and* below the Fe_3O_4 particle layer, and our approximation of 1.8nm interparticle spacing is not necessarily extremely precise but generally valid. Thus we have successfully

verified the crystallographic order and geometry of several nanoparticle lattices and a general approximation by matching simulated GISAXS of theorized structures to experimental GISAXS of actual structures. This demonstrates the use (and usefulness) of the NANODIFT GISAXS simulator and FFT calculator (extension to Mathematic) and the method of linear analysis of GISAXS intensity plots for characterizing nanoparticle superlattices, and for research in direct-assembly via interface-driven order in soft-particle colloids in general.

3.4 Conclusion

In Summary, In-situ GISAXS study of interfacial EISA of monolayer NP/polymer array revealed that the assembly can be divided into two stages: Firstly the NPs mitigate to the air/polymer interface and form a liquid-like disordered packing while the majority of the solvent was evaporating, second the NPs assembled into hexagonal close-packed fashion and the transient phase disappeared. This superlattice growth mechanism differs from the pure NP assembly on liquid or solid surface where isolated NP islands generally formed before collapse of islands either by mechanical squeezing or natural integration through water drop evaporation. Using reflectivity GISAXS, we confirmed that the nanoparticle layer is phase separated from polymer matrix and reside on the air/liquid interface. Nevertheless, in combination with simulation tools, we studied the interfacial assembly of binary superlattices and reasoned the packing morphologies of two types of nanoparticles.

Chapter 4. Transformation of a close-packed Au nanoparticle/polymer monolayer into a large area array of oriented Au nanorods via e-beam promoted uniaxial deformation and room temperature sintering

4.1 Introduction

Two-dimensional (2D) nanoparticle arrays or superlattices are of physical and chemical interest as analogs to their crystalline counterparts assembled from atoms. To date, well developed colloidal chemistry enables fast and facile synthesis of metallic,[99] semiconductor,[81,90,100] and magnetic nanoparticles (NPs)[83] with precise size and shape control. Further entropy driven self-assembly of monosized and binary NPs[6-9] has resulted in ordered arrays in which collective electronic, magnetic and optical properties can be tuned through electron charging and quantum confinement of individual NPs mediated by coupling interactions with neighboring NPs. Despite considerable progress on developing structural perfection of NP arrays, their analogy to atomic solids breaks down with respect to electron transport. Because NPs are stabilized with dielectric organic ligands, NP arrays are insulators and behave as an array of isolated Coulomb islands unless sufficient field strengths are applied to achieve electron tunneling.[101-103] To facilitate electron transport for optoelectronic applications, tremendous effort has been aimed at: modifying the insulating organic capping layer by ligand exchange[104], thermal annealing to neck adjacent nanoparticles,[90] or even metal chacogenide complexation and

conversion to semiconductor phases upon gentle heating, generating inorganic nanocrystal solids[105].

An alternative approach to achieve efficient and directed energy or electron transfer is the assembly of one-dimensional nanoscale building blocks, nanorods or wires. Reported methods include electric-field assisted alignment,[55,106] interfacial compression with Langmuir-Blodgett troughs,[107,108] stream alignment with microfluidics,[109,110] blown-bubble-films,[111,112] "knocking down" motion,[113] and contact printing.[114-116] Although significant progress has been made,[117] oriented assembly of nanowires over a large area with side-by-side registry and high density remains a significant challenge.

Here we report the formation of a large scale, ordered, and oriented Au nanowire array by transformation and coalescence of an ordered close-packed gold nanoparticle/polymer monolayer via constrained uniaxial deformation and room temperature sintering induced by electron beam irradiation. This approach results in high densities of integrated single crystal like nanowires that exhibit directional metallic conductivity on the macroscale.

4.2 Experiments and discussion

We start from 2D monolayer nanoparticle array self-assemblies,[93] which are easier to fabricate, and then apply external stimulus to drive directional deformation of polymer matrix, thus alter the arrangement of nanoparticles in the composite. Specifically, with Au nanoparticles, we have achieved transformation from particulate units to wire-like anisotropic units by coalescence at room-temperature, which provides a new strategy toward oriented and aligned anisotropic assemblies in solid phase.

2D Au NP/poly (methyl methacrylate) (PMMA) monolayer arrays were prepared by dispersion of 5.5-nm diameter, alkane-thiol stabilized Au NPs dissolved in a solution of toluene plus PMMA on a water surface. Evaporation induced self-assembly confined to a fluid interface results in a large area ordered NP/PMMA monolayer[93] that was transferred[118] to a trenched structure, resulting in a constrained, freely suspended film with one free edge (see Schematic Figure 1) aligned in the trench. AFM and x-ray reflectivity experiments determined that the NPs reside exclusively at the original polymer/air interface (as opposed to within the 50-nm thick polymer film or at the original polymer/water interface). The suspended films were then subjected to E-beam irradiation employing current densities in the range of 30-200 pA/cm^2 and an accelerating voltage of 200 kV. TEM imaging (Figure 2) showed that E-beam irradiation causes uniaxial contraction in the direction normal to the free edge, accompanied by only a modest expansion in the corresponding normal direction (Figure 2B). After about 1 min, the NP d-spacing was reduced by 20% in the unconstrained direction, forming chain-like aggregates (Figure 2B). Sometimes quasi-square planar NP arrangements were formed, depending on the NP orientation of parent film, as shown in Figure 4 and simulated in Figure 10). Further aging at room temperature without E-beam irradiation resulted in a more uniform and fused nanowire-like array, with rod lengths extending up to several hundred micrometers (Figure 2C).

Figure 1 Schematic showing the E-beam irradiation of free-standing nanoparticle/polymer array and the resulting retraction

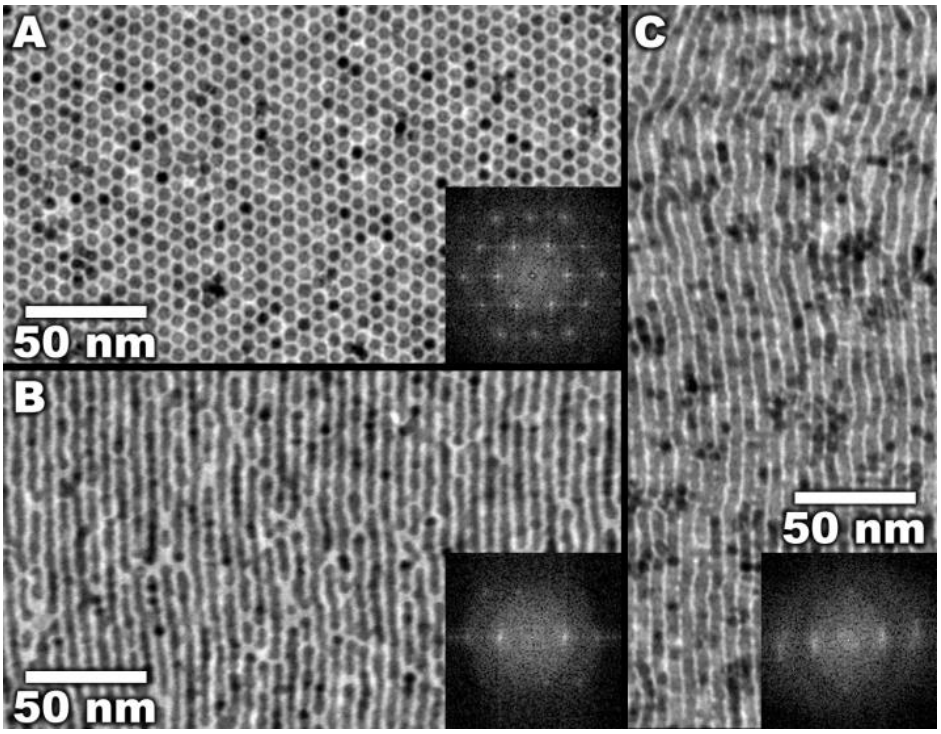

Figure 2 a) TEM image showing large-area hexagonal close-packed Au NP/PMMA monolayer array prepared by interfacial assembly. b) Typical pearl-chain-like nanostructure formed by irradiating the free-standing NP/PMMA monolayer array under E-beam. c) Ordered Au nanowire array formed.

Thin film sample was irradiated by e-beam with current density in the range of 30-200 pA/cm^2 and accelerating voltage of 200 kV for minutes. The e-beam irradiation dose thus applied is comparable to that utilized in regular positive-tone patterning of PMMA. The E-beam dose effect has also been investigated.

When we focused the beam and irradiate the film with high current intensity above 1000 pA/cm^2, random coalescence took place and generally network structure formed (Figure 3).

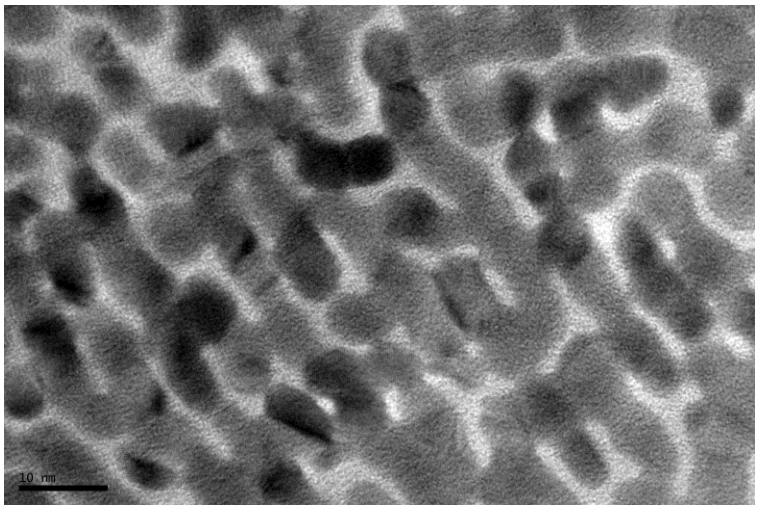

Figure 3 Random sintering of Au nanoparticles under E-beam irradiation

After E-beam irradiation at mediate dose for about 1 min, d-spacing has been reduced in one direction, while remaining constant in the corresponding normal direction. In the course of this deformation, quasi-cubic close-packed phase as transition state was found to form. Further retraction of the film induced linear aggregation of nanoparticles in a specific direction until the nanoparticles are brought into proximity and some attached to each other. For free-standing film without free edge, similar retraction was observed, while d-spacing change took place in all directions. However, for supported film on substrate, the hexagonal arrangement has always been preserved.

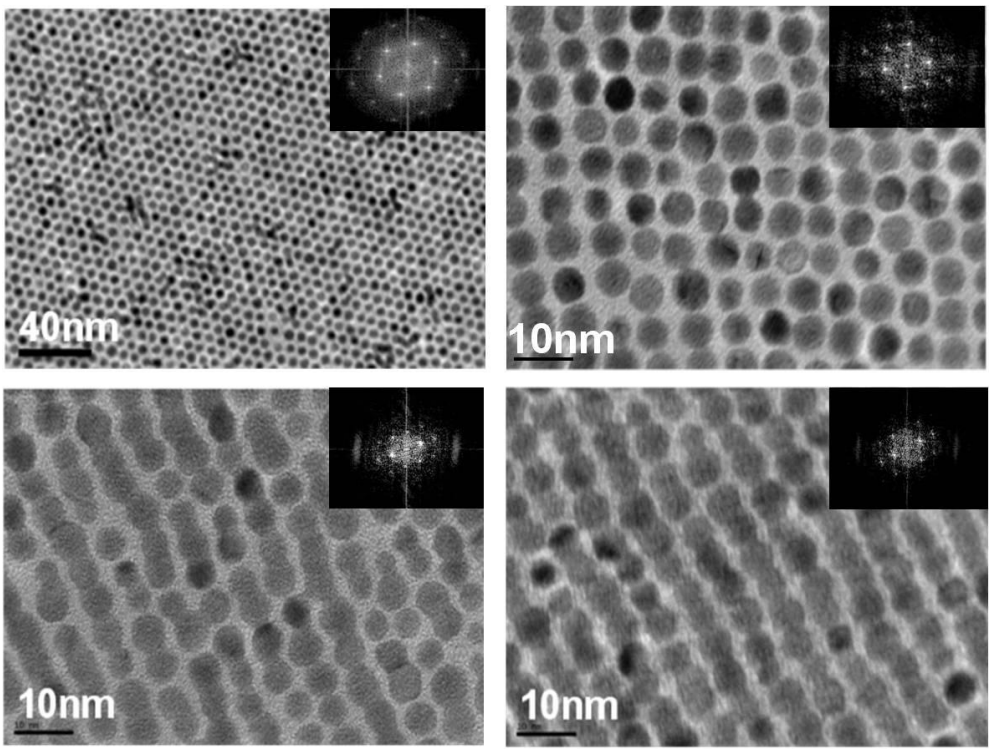

Figure 4 Evolution of Au NP/PMMA monolayer array under E-beam irradiation.

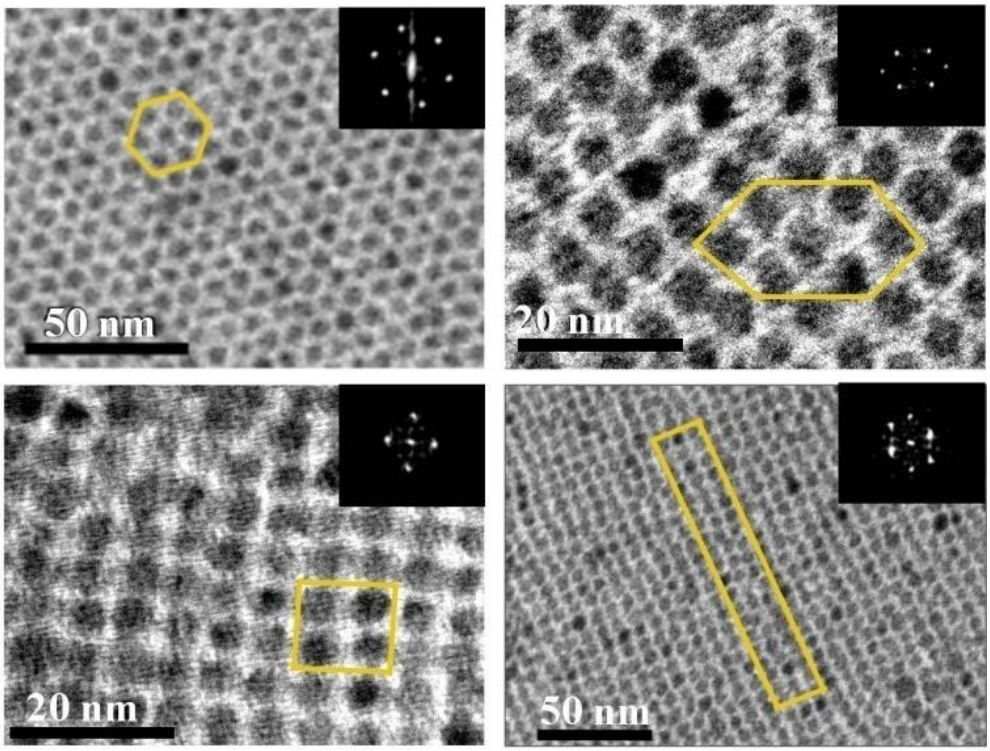

Figure 5 Evolution of PbS/PMMA monolayer array under E-beam irradiation (PbS capped with oleic acid, 5nm core size). The inset shows the FFT of respective TEM images.

PbS QD/PMMA monolayer arrays were also prepared using the same method as Au NP/PMMA monolayer arrays and then transferred onto a trenched glass slide, then irradiated under E-beam. The arrangement of PbS QDs changed accordingly. Hexagonal close-packed (HCP), deformed HCP, and quasi-cubic close-packed, as well as large area of pearl-chain structure were observed dependent on different compression angle. Unlike the Au NPs, there was no sintering going on due to higher melting point of PbS QDs.

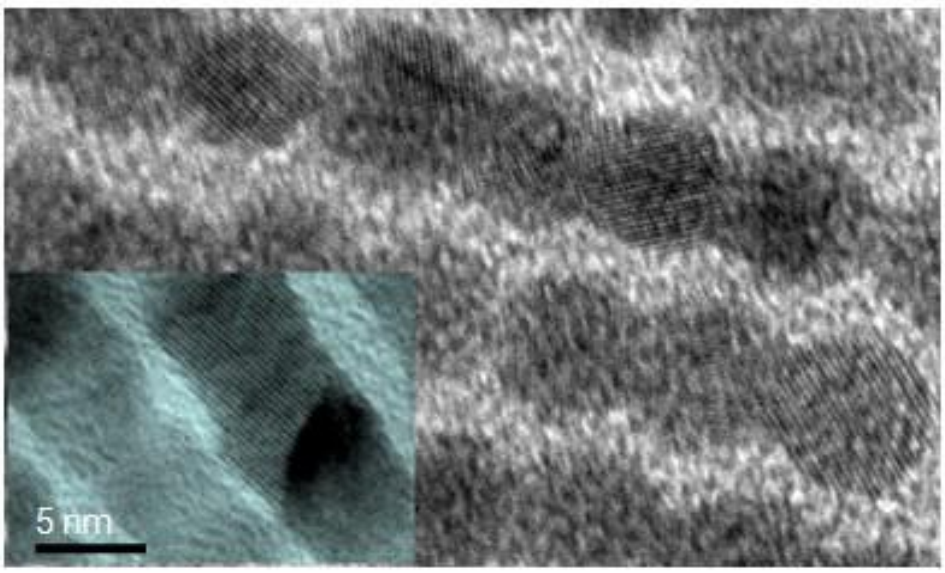

Figure 6 High resolution TEM images demonstrating the rotation of Au nanoparticles during sintering. Inset: single crystalline domain with dimension larger than the diameter of nanoparticle.

High resolution TEM imaging showed that the nascent NP aggregates were randomly oriented (Figure 6), but upon aging they coalesced and re-oriented into uniform nanowires (Figure 6 inset). In comparison, for completely unconstrained free-standing films, similar retraction was observed, but the d-spacing decreased uniformly in all directions, preserving the original hexagonal arrangement of the NPs.

To explain our experimental results, we propose that E-beam irradiation of PMMA, a positive tone E-beam resist, results in chain scission, reducing its molecular weight and modulus of elasticity. The reduced modulus allows residual stresses that develop upon drying of the transferred film[119] and capillary stresses acting on the protruding NPs to direct aggregation in the unconstrained direction normal to the free edge. Conservation of volume is achieved by expansion in the interchain spacing and polymer and thiol transfer to the underlying polymer film or overlying NP/air interface. Given such a short irradiation time, mass loss of polymer is neglectable.[120]

Suspended and supported Au nanoparticle arrays formed by transfer on to a holey carbon grid reacted differently under E beam irradiation (Figure 7). NPs incorporated on the free-standing, suspended polymer underwent one-dimensional compression to form chain-like aggregates, while solid (carbon)-supported NP/polymer arrays retained their original close packed configuration after E-beam irradiation.

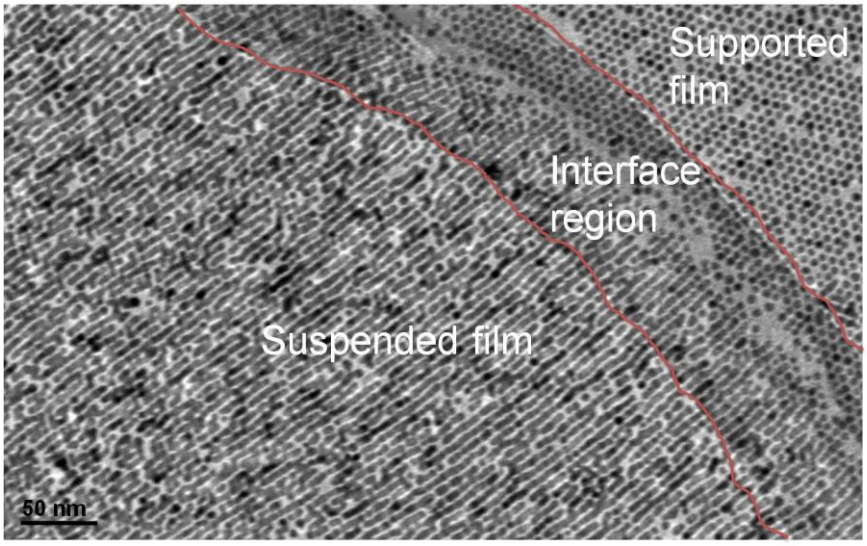

Figure 7 Different behavior of suspended and supported nanoparticle arrays under E beam irradiation. Anisotropic structure formed for the free-standing part due to compression and the hexagonal close-packing in supported region was preserved.

4.3 Simulation

"Large-scale Atomic/Molecular Massively Parallel Simulator" (LAMMPS) was used to simulate the Poisson compression of nanoparticle array. 2D / 3D runs with up to 13K particles was performed on the "nano" linux cluster at the UNM Center for Advanced Research Computing, with an average simulation time in scale of ms, and hours of run time.

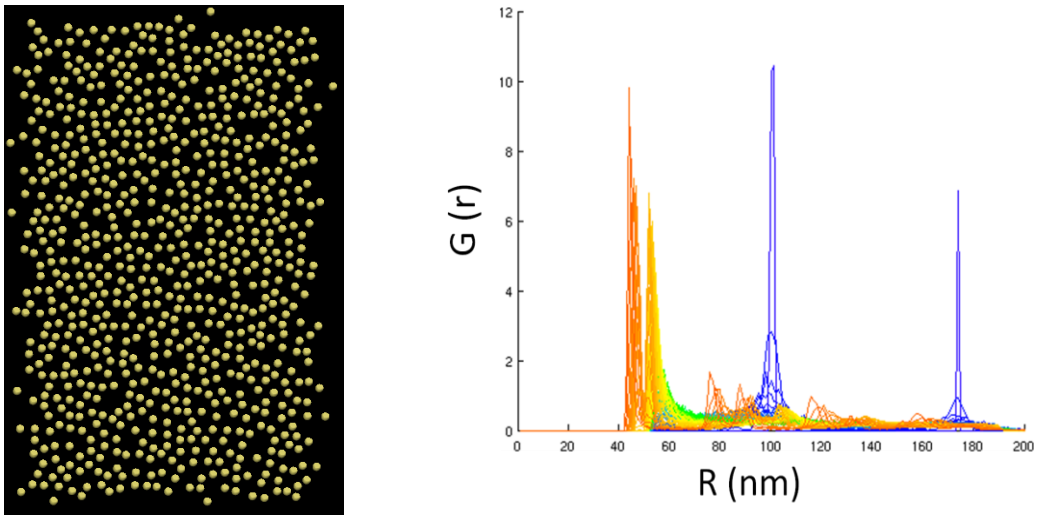

Figure 8 Left: the equibration snapshot of nanoparticles before the evaporation-induced self assembly at interface. Right: the RDF plot over evaporation stage.

The amount of "linearity" in the nanoparticle chains is a function of the poisson ratio and the viscosity. The length, (and molecular weight, density, coating percentage, chi param, etc...) of the alkanes are all set as parameters within LAMMPS, and they control the coarse-grained particle interactions. The interparticle energy actually goes to NAN (not a number) in this simulation since the particles are allowed to overlap, and the theoretical models have a force asymptote at 0 separations (hard-sphere potential). We are capping the interparticle force at around 1 nN, which allows them to overlap. The

viscosity is also artificially high, like by 20,000X, to make the particles move into each other rather than slide around each other.

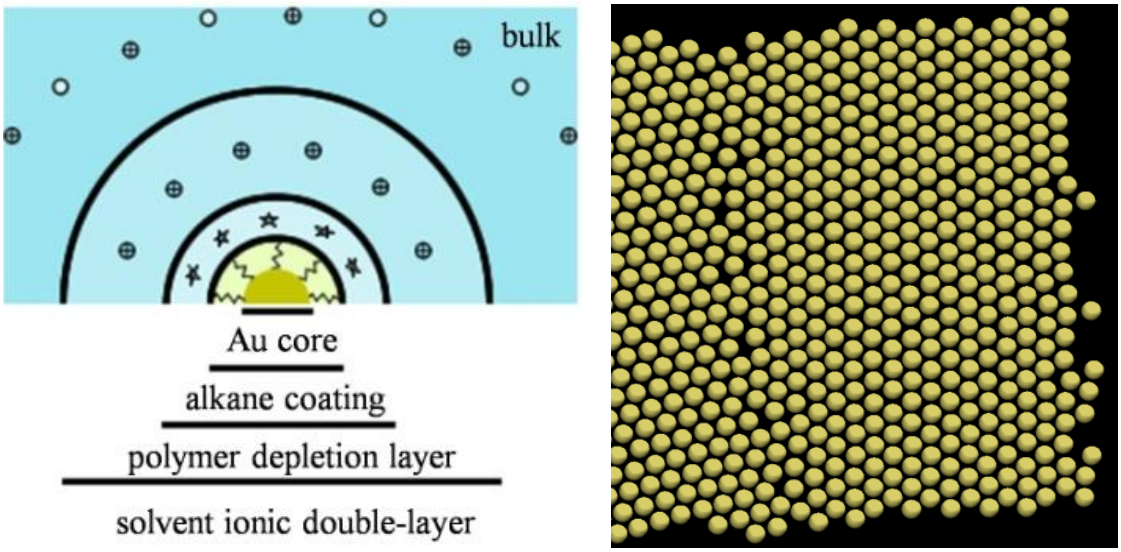

Figure 9 LAMMPS simulation of evaporation-induced nanoparticle assembly

Finite element simulations of the bench-scale process reveal a substantial area of uniform, constrained uniaxial compression, with edge effects (where substantial mixed, shear deformation occurs) confined to the outer perimeter. The simulations were of a quasistatic elastic solid material of the dimensions of the pre-irradiated film (100 nm x 3 mm x 5 mm). The process of drying and residual stress redistribution was predicted using pre-stress and mass-loss terms in a Lagrangian framework. The mesh, being Lagrangian in nature, follows the motion of the elastic network, indicating a uniform compression over a large portion of the film (as shown is Figure 11B). Because the Au NPs reside at the polymer surface, we expect their trajectories to be well predicted by the simulation.

To visualize the one dimensional deformation of the close-packed NP monolayer at the NP scale, we used a molecular dynamics code LAMMPS[121] with polymer/solvent/particle

interactions incorporated in the Vincent potential, based on Flory-Huggins theory derived for spherical, polymer-coated particles and accounting for 1) bulk-polymer induced depletion, 2) polymer-polymer steric repulsion, and 3) polymer-polymer elastic repulsion. DLVO, polymer, and lubrication forces are all coarse-grained to enable multi-scale simulations much larger than DFT or molecular methods can permit. In order to simulate the aspect of sintering, particle diffusivity is artificially restricted and maximum inter-particle force is limited during compression such that the particles are forced to overlap slightly. Figure 11C shows a simulated 2D close-packed array of 5.5-nm diameter, alkane-thiolated Au nanoparticles formed from a dilute solution of NPs in toluene/PMMA by solvent removal and equilibration at 298K. Subjecting the closed packed monolayer to a simulated one-dimensional Poisson compression with Poisson ratio 0.1 (based on the surface aspect ratio of the deformed Lagrangian mesh) and corresponding to that of a nearly incompressible solid, results in the formation of chain-like aggregates whose orientation depends on that of the parent close packed array. Comparison of TEM and FFT of both the experimental and simulated systems (Figures 2 and 11) show good agreement (considering the finite size of the simulation), suggesting that the simulation captures the essential physical parameters of self-assembly and one dimensional deformation into chain-like aggregates.

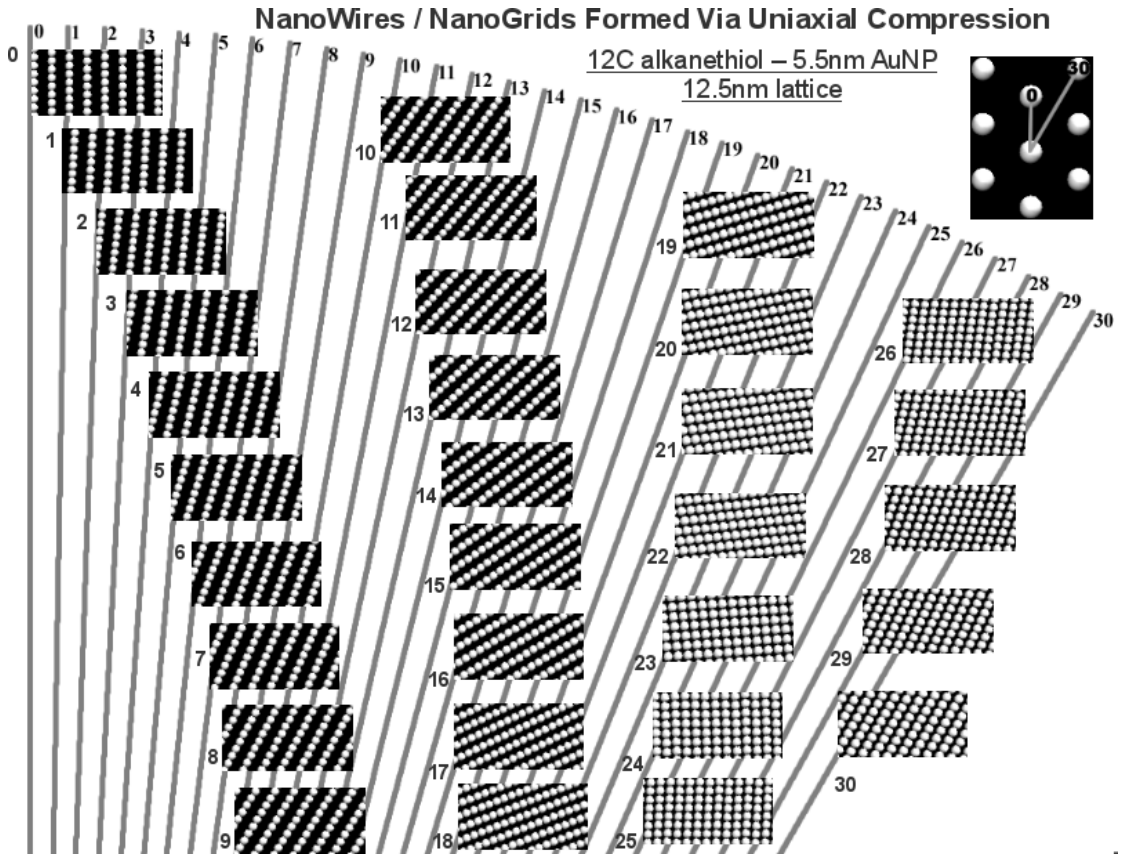

Figure 10 Morphology of 2D nanoparticle array after uniaxial compression along different angles (from 0 to 30º). Original array with angles indicated is shown in inset.

Figure 10 shows the results from a set of 30 simulations of uniaxial compression, with Poisson ratio 0.05, of a thin film of Toluene/PMMA with a hexagonal-packed lattice of 5.5nm Au NPs with adsorbed 12C alkanethiol on the top surface; with lattice constant 12.5nm (The lattice constant was expanded here compared to real experiments to enable easier visualization). In these simulations the minimum compression percent needed to form nanowire structures is 50% corresponding to 0 degrees lattice angle to the compression, and as much as 80% compression is needed to form the grid-like structures seen at 24-25 degrees lattice angle to the compression. Figure 10 illustrates that either nanowire or nanogrid structures can form depending on the angle of the hexagonal lattice with respect to the free edge of the film and uniaxial compression direction. Because the parent NP/polymer monolayer forms by an evaporative self-assembly process (similar to

convective assembly) whereby a liquid-solid-vapor interface recedes from a pinned free edge, we propose the zero degree orientation which aligns the nanoparticles normal to the free edge to be most favorable. This alignment is preserved in the transferred film as the free edge is oriented in the notch (Figure 11A) –one dimensional compression leads to oriented nanowires. As the simulations indicate, if interfacial assembly leads to other monolayer orientations or if the transferred film is misaligned in the notch, other NP assemblies can form upon contraction as we see in Figure 10.

To understand the further particle coalescence into single crystal-like nanowires at room temperature, we emphasize that the location of the NPs at the polymer vapor interface reduces mechanical constraints and facilitates depletion of thiol ligands from regions between the approaching particles.[118,122] This allows nascent particle-particle contact (Figure 2C and 11) and NP re-orientation into energetically favored configurations with crystallographically aligned NP-NP interfaces. Ensuing sintering and coarsening driven by the high NP curvature that increases surface tension of Au and accordingly the associated driving forces[123-125] continue during room temperature aging (without e-beam irradiation) until a wire-like structure evolves (Figure 6 and 6inset) that minimizes differential curvature and interfacial energy.

LAMMPS simulations also provide insight into the effect of orientation of the NP monolayer array with respect to the free edge on the ensuing array morphology after uniaxial compression. The original array has 6-fold symmetry; thus the possible compression angles are limited to be in the range from 0° to 30° (0 to -30˚are mirror images). Figure 10 shows a ‘map’ of hexagonal NP arrays, with original orientations

ranging from 0 to +30˚with respect to the uniaxial compression direction, at the point of initial particle-particle contact leading to chains, e.g. 0 or 30˚, or 2D, quasi-square grids, e.g 25˚. In the 0˚ orientation, chains form with ~20% compression with only a modest expansion in NP-NP spacing in the direction normal to the compression direction. This simulated result corresponds closely to our experimental results, suggesting that the original NP arrays are preferentially oriented with respect to the free edge. As the free edge forms by interfacial NP assembly at a retracting three-phase liquid/solid/vapor interface,[93] we argue that the 0˚ angle configuration that aligns the NPs normal to the interface is most probable, thereby orienting preferentially the NP array in the transferred film and enabling consistent formation of NP chains and wires. The 0˚-oriented contraction is captured by TEM in Figure 6, which shows the interface between NP chains and the parent NP monolayer array and how chains form by 1-dimension contraction in the 0˚ orientation. Other initial orientations are possible and edge effects are anticipated near the boundaries of the suspended films (Figure 11B), These could form quasi-square lattices as shown in Figure 5 or wires inclined with respect to the free edge. It is interesting to note that the nanowire arrays have analogies to a quasi-2D thermodynamically-defined lamellar mesophase[126,127] and defects like dislocations and disclinations are occasionally observed.

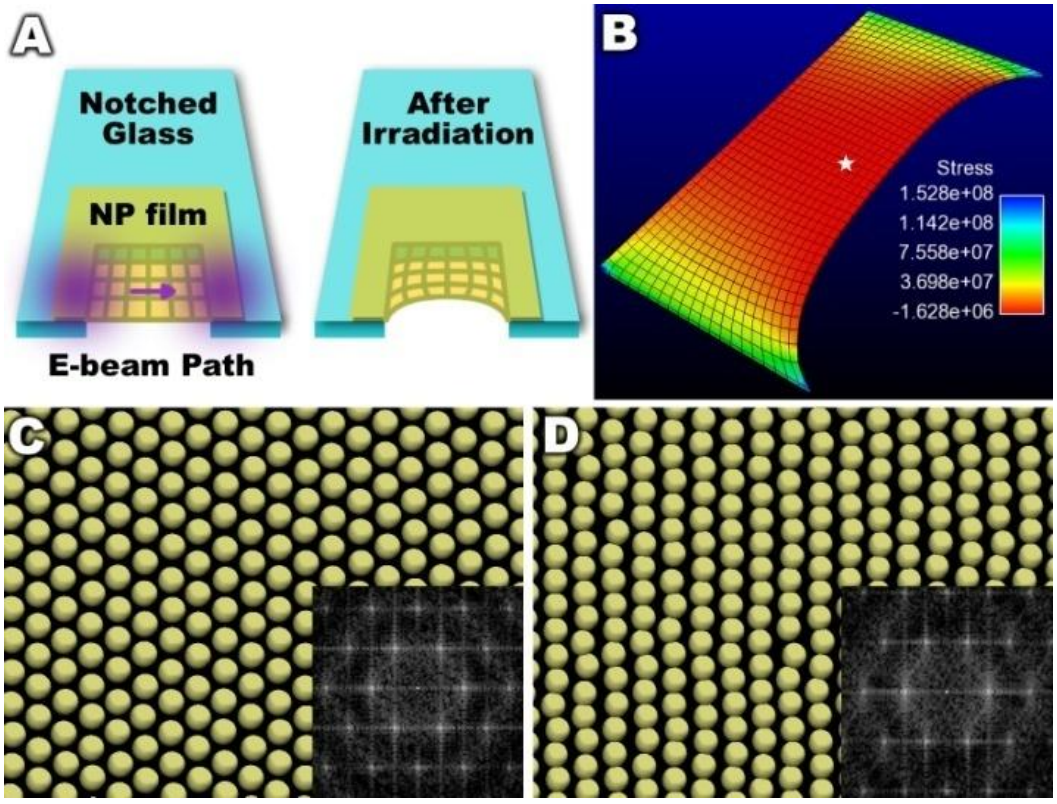

Figure 11 (A) Schematic shows original film configuration and the retraction (upon E-beam irradiation) of the suspended nanoparticle/polymer monolayer array with a free edge.(B) In plane axial normal stress in receding direction as predicted from a Lagrangian finite element simulation of residual stress relief due to volume change (Dot shows area of MD simulation).(C) Molecular dynamics simulation of original self-assembled NP/polymer array and (D) Formation of nanowires by anisotropic Poisson compression.

The anisotropic rod-like Au nanostructures formed by E-beam irradiation and room temperature aging as in Figure 2C were characterized electronically with a linear four-probe setup over the temperature range, 80 to 300K. For these measurements the inside two probes were separated by about 50~200 μm. The I-V plot (Figure 12 inset) acquired at room temperature shows linear, Ohmic behavior in the direction parallel to the rod orientation with resistivity determined to be 5kΩ·nm (nearly comparable to that of polycrystalline Au nanowires: 1kΩ·nm),[128] while in the normal direction the array was insulating over the measured range of potential bias (for this probing distance, a much

greater voltage needs to be applied to reveal the Coulomb blockade effect[103]). The irradiated sample showed a dramatic change in conductivity before and after the room temperature aging process. The Ohmic I-V behavior and conductivity of the anisotropic nanostructure after complete sintering and coarsening is independent of temperature, as expected for a metal. However, for the as-irradiated sample without aging, log (σ) was found to vary nearly linearly with 1/T, corresponding to an effective activation energy of 3.8meV. This is consistent with that of electrons hopping across the grain boundaries of chain-like aggregates, which behave as a one-dimensional array of quantum islands.

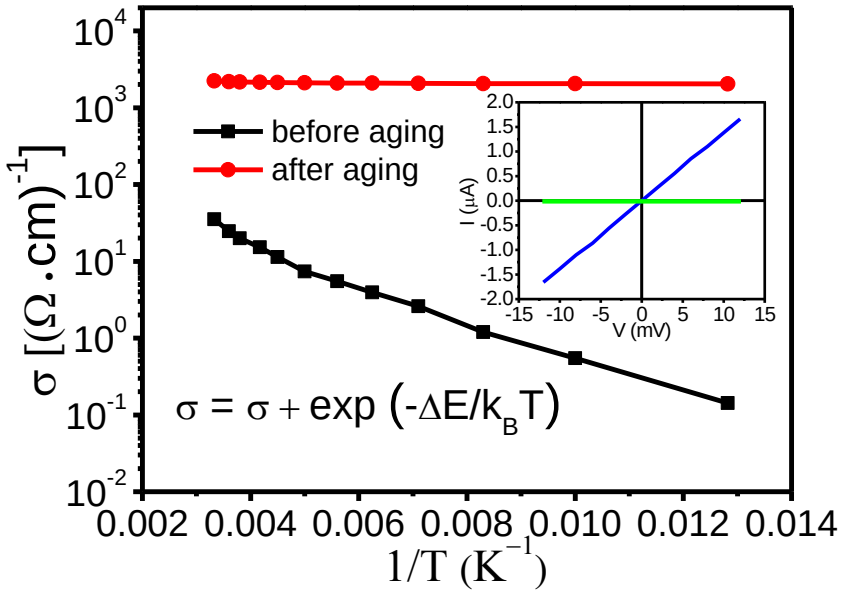

Figure 12 Temperature dependence of conductivity measured for E-beam treated NP film before and after aging process. Inset: I-V behavior (at 300K) for irradiated and aged film along the retracting direction (in blue) and in the normal direction (in green).

4.4 Conclusion

Large scale ordered and oriented metallic nanorod arrays, exhibiting highly anisotropic electrical conductivity, were formed by one-dimensional deformation, re-orientation, and

sintering of a free-standing close-packed gold NP/polymer monolayer at room temperature. As the individual unit operations, viz. self-assembly, transfer, and e-beam irradiation are all scalable and compatible with traditional semiconductor miniaturized platforms, this approach might be generally applicable for the fabrication and integration of dense, large area, anisotropic nanostructures.

Chapter 5. Integration of a Close-Packed Monolayer with a Photonic-Crystal Cavity via Interfacial Self-Assembly and Transfer

5.1 Introduction

Nanoparticle (NP) assembly into ordered 2- and 3-D superlattices has stimulated enormous recent interest as a means to create new artificial solids whose electronic, magnetic, and optical behaviors can be tailored by the size dependent properties of the individual NPs mediated by coupling interactions with neighboring NPs,[129,130] suggesting applications in a diverse range of technologies including photovoltaics,[131] sensors,[132] catalysis,[91] and magnetic storage.[82] To date superlattice assembly has been demonstrated for monosized[63], binary[68], and even ternary systems[133], allowing development and interrogation of a range of collective behaviors: electron transport within 2- and 3-D arrays of Coulomb islands[103,134], Forster resonance energy transfer between superlattice monolayers in close proximity[135], switchable optical properties through regulation of NP d-spacing[129], and new magnetic behaviors based on binary superlattices[136]. Superlattice fabrication is performed principally by droplet evaporation[72] or convective assembly on an inclined plate[137,138]. These techniques are often slow, restricted in the size and topography of the substrate, and result in van der Waals solids with limited mechanical behaviors. To address these issues，we recently reported a general, rapid method to prepare large area, free-standing, NP/polymer monolayer superlattices by interfacial NP

assembly within a polymer film on a water surface.[93] The ultra-thin superlattices are highly robust and transferable to arbitrary substrates.

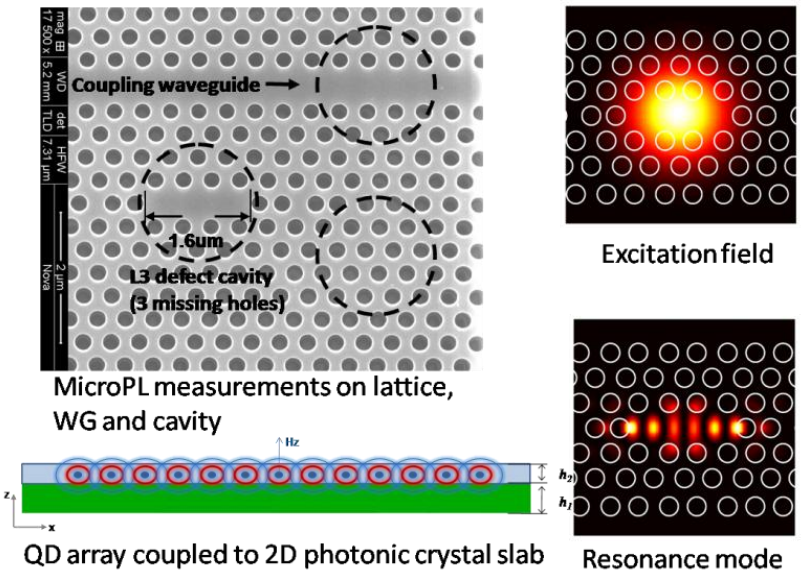

Figure 1 Illustration of L3 defect cavity of 2D photonic crystal and the coupling of photo emitters

Here we demonstrate interfacial self-assembly and transfer as an approach to address a long-standing technology challenge: how to integrate colloidal light emitters (e.g. semiconductor quantum dots) with a nanophotonic structure in a manner that achieves good quantum dot (QD) coupling with anti-nodes of the optical microcavity and avoids significant Q factor degradation. Enhancement of spontaneous emission from photo emitters coupled to the photonic crystal microcavity based on the Purcell effect [139] provides an ideal test for the integration of bottom-up self-assembly with top-down nanofabrication and means to study emitter behavior in microcavities. Standard spin-coating cannot achieve a high QD density, uniform film thickness, or controlled uniform separation between QDs over the photonic crystal surface[140]. Fabrication of a photonic crystal cavity around a single pre-screened Stranski-Krastanow grown QD with the desired optical properties is laborious, although exquisite control in position and

wavelength is possible.[141] Templated growth of single quantum dots on GaAs (111)B surfaces has been demonstrated to provide good spatial control[142], but suffers from low QD density and the requirement for precise control of the emission wavelength for high Q cavity applications.

5.2 Experiments and results

For photonic crystal and microcavity fabrication, the starting material is 150 mm diameter silicon-on-insulator (SOI) wafer with 250nm thick silicon device layer with 3μm thick buried-oxide (BOx) layer. The pattern is a triangular lattice with lattice constant in the Γ-K direction of a=415nm and holes diameter of 240nm. A cavity is created in the photonic crystal lattice by three missing air holes (L3) shown in Figure 1a-c. The cavity has the end-hole positions shifted away from the cavity by a nominal value of 0.18a, 0.025a, and 0.18a, as in the design by Akahane et. al.[143]. Devices fabricated thereby have 100-300 holes in the Γ-K direction with a waveguide along this direction and 15 holes in the Γ-X direction. We use commercially available, mass-production semiconductor processing tools throughout the fabrication process. A waveguide is also fabricated thus can be used to couple an external source into the microcavity. The coupling strength is controlled by the number of holes between the waveguide and the cavity. In particular, we will discuss result associated with the $1.1W_1$ waveguide which has a width 10% larger than it would have been with a row of missing holes.

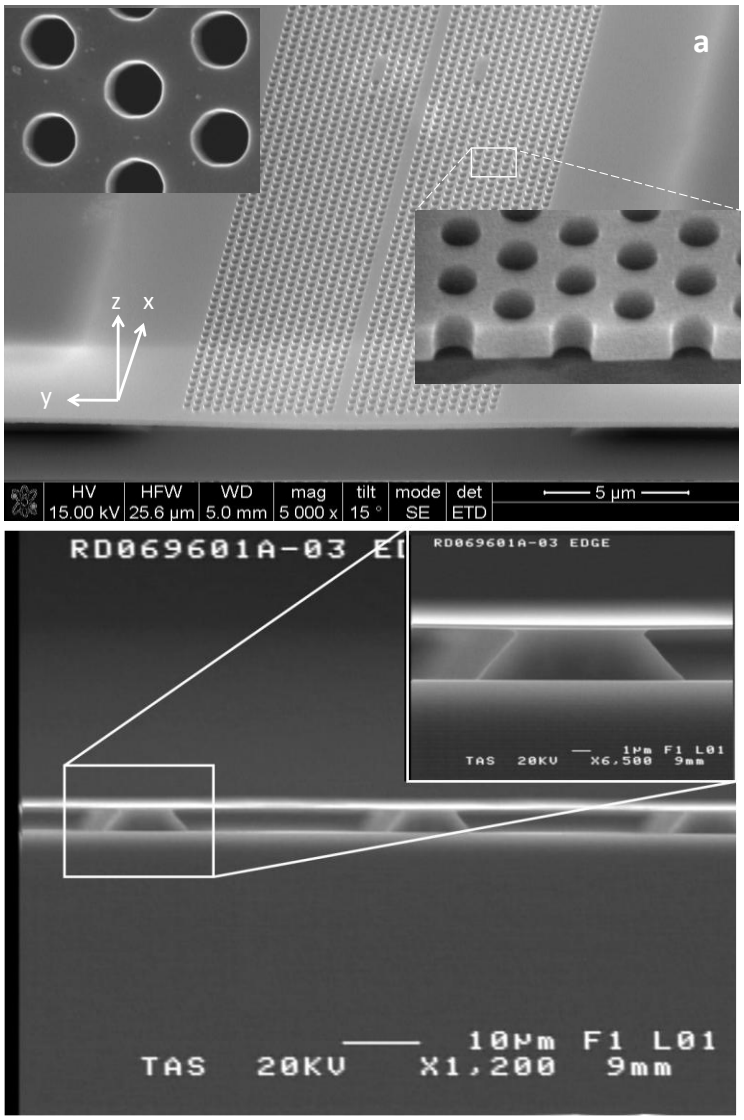

Figure 2 (a) SEM image of a 2D silicon membrane photonic crystal device consists of two L3 cavities and a waveguide supported with SiO_2 anchors. The top left inset shows the top view of the holes on the silicon membrane. The lower right inset shows the side wall profile of the holes. (b) Cross view showing the anchor supporting the Si membrane.

All lithography was performed on an ASML PAS 5500 Step-and-Scan system, and all dry etching was performed with Applied Materials Centura platform tools. The first lithographic layer defines the photonic crystal by patterning 240nm holes in the photoresist. This pattern is transferred into the device layer using reactive ion etching

(RIE), optimized for straight vertical sidewalls. A second mask level was used to etch the substrate on either side of the device for optical access. A deep reactive ion etch (DRIE) was used to create roughly 80μm deep grooves into the silicon to provide optical coupling of the lens fiber to the waveguides. To protect the photonic crystal that had been etched into the device layer, an 8.5 kÅ polysilicon film was deposited on top of a 2μm thick oxide film and then patterned with a photoresist mask. The polysilicon hard mask was used for the oxide etch steps because relatively thick oxide films were employed (2μm hard mask, 3μm BOx). The oxide film served as a hard mask for the DRIE Si etch. During the BOx etch, the photoresist mask is consumed and the polysilicon hard mask is used to define the pattern. During the DRIE handle etch, the polysilicon mask is also consumed so that the underlying 2μm oxide film now acts as the mask to protect the silicon photonic crystal device. Finally, hydrofluoric acid (HF) was used to strip the remaining oxide hard mask, as well as to undercut the SOI buried oxide below the lattice. A timed etch was used so that the oxide was stripped below the lattice to produce an air-clad photonic crystal, but sufficient oxide remained at the edge of the device to anchor the structure to the substrate. Figure 2 shows SEM images of a fabricated photonic crystal device.

A micro-photoluminescence (PL) setup (see Figure 3) was used to characterize the PL emission from PbS QDs on the photonic crystal cavity. A cw 830-nm fiber pig-tailed diode laser was used to generate excitons in the QD through non-resonant excitations. The output of the laser was delivered by a single-mode 5.6-μm core fiber collimated to match the entrance pupil of a Mitutoyo 50X NIR HR objective (NA = 0.65),

producing a diffraction limited spot size of 1.6 μm $1/e^2$ diameter on the measured sample. The out-of-plane PL from QDs was collected by the same objective and spectrally resolved by a 0.3-m imaging spectrometer (Acton SP2300i) equipped with an OMAV InGaAs array detector (Princeton Instruments). To avoid photo-oxidation of PbS QDs, the sample was mounted in a thin hermetically sealed cell assembled in a glove box purged with dry nitrogen. A microscope cover glass with a 12 mm clear aperture was used as the window for optical access. With the above setup, we measured the PL spectra of PbS QDs on over 100 different photonic crystal cavities and consistently observed the enhanced PL of QDs due to the coupling from photonic crystal cavities. We have not noticed any significant difference in the enhancement factor when switching between these two laser sources. However, 904nm laser appears to have a smaller photo-bleaching effect. A diffraction limited spot size of ca. 1.6μm $1/e^2$ diameter is produced on the sample. The out-of-plane PL is collected by the same objective and coupled to a 0.3m or 0.5m imaging spectrometer through a 50um diameter multimode fiber with a spectral resolution of 0.4nm and 0.1nm respectively equipped with an OMAV InGaAs array detector.

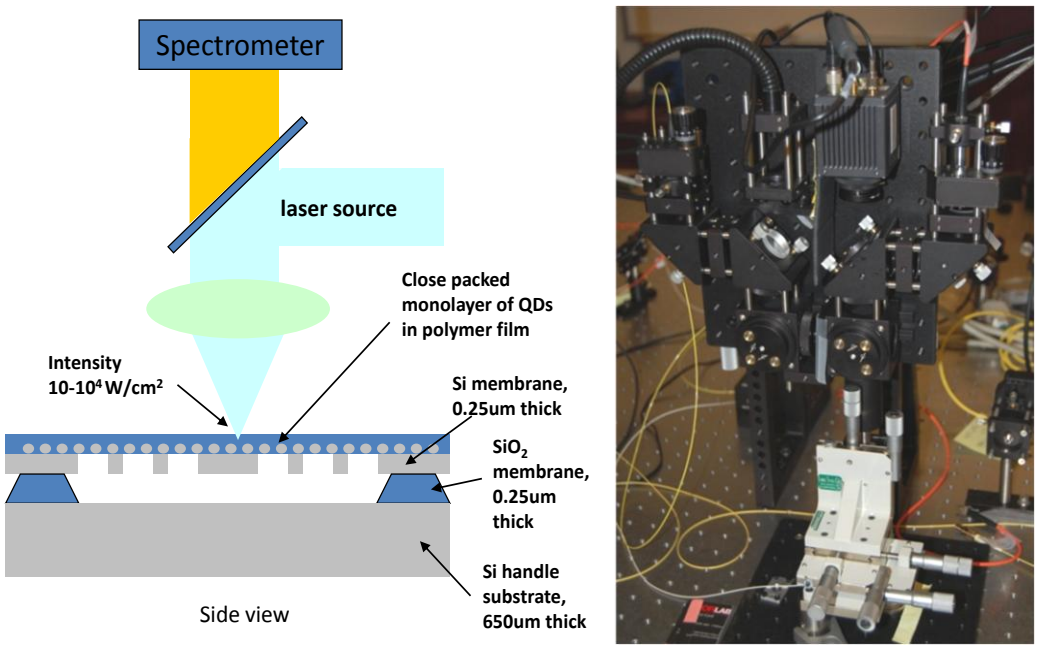

Figure 3 Experimental setup for micro-PL measurement of PbS QDs coupled to 2D photonic crystal cavity.

5.3 Interfacial assembly and transfer

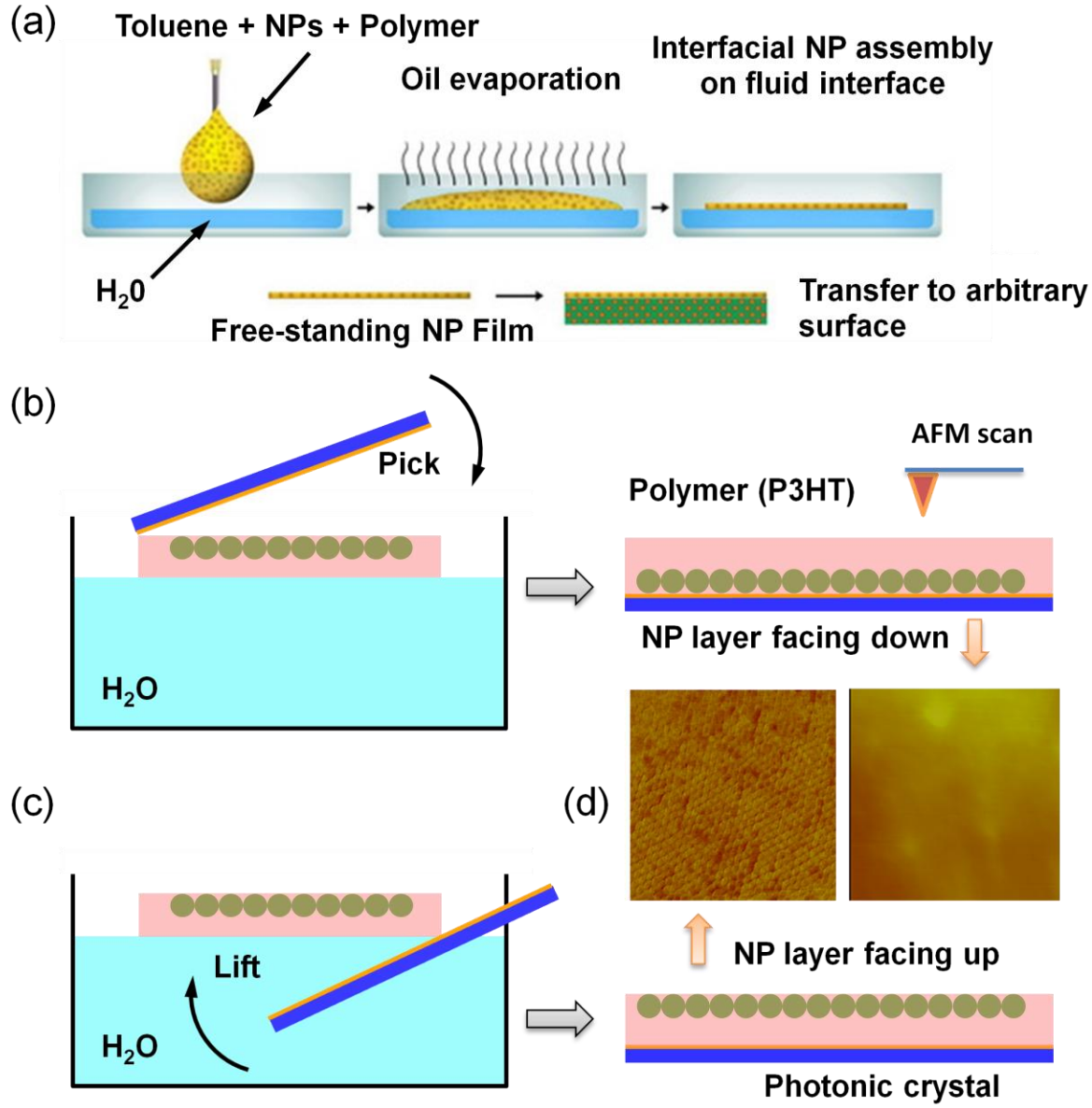

Figure 4 (a) Schematic of the evaporation induced interfacial assembly and transfer process. (b) Film transfer to the photonic crystal cavity by picking process results in a monolayer where the QDs are in close contact with the photonic crystal surface. (c) For lifting, the QDs are about 20-nm away from the photonic crystal in the vertical direction. The AFM images (d) show the surface topography for the original vapor-side interface (AFM image of lifted monolayer) and for the original water-side interface. The dimension of the scanned image is 250 × 250nm.

Self-assembly of the close-packed PbS QD/polymer monolayer was based on the interfacial evaporation induced self-assembly (EISA) procedure we recently reported[93], and which we summarize briefly here. Oleic acid ligated PbS QDs (purchased from Evident Technologies) were dissolved in toluene containing polythiophene (P3HT) (interfacial assembly can be performed with many different polymers; P3HT is a representative example). One drop (about 8 µl) of the QD/P3HT/toluene solution was dispensed quickly by a syringe onto the surface of deionized water contained in a Petri dish. The droplet immediately spread into a film of ca. 5 cm diameter on the water surface. Solvent evaporation drives QD self-assembly followed by solidification within P3HT, the water interface maintaining the required QD mobility needed to achieve a highly ordered low defect QD monolayer. The resulting monolayer film is only 20-nm thick as determined by ellipsometry. The film thickness can be controlled by the polymer concentration in the solution (0.5-5mg/ml in the case of P3HT).

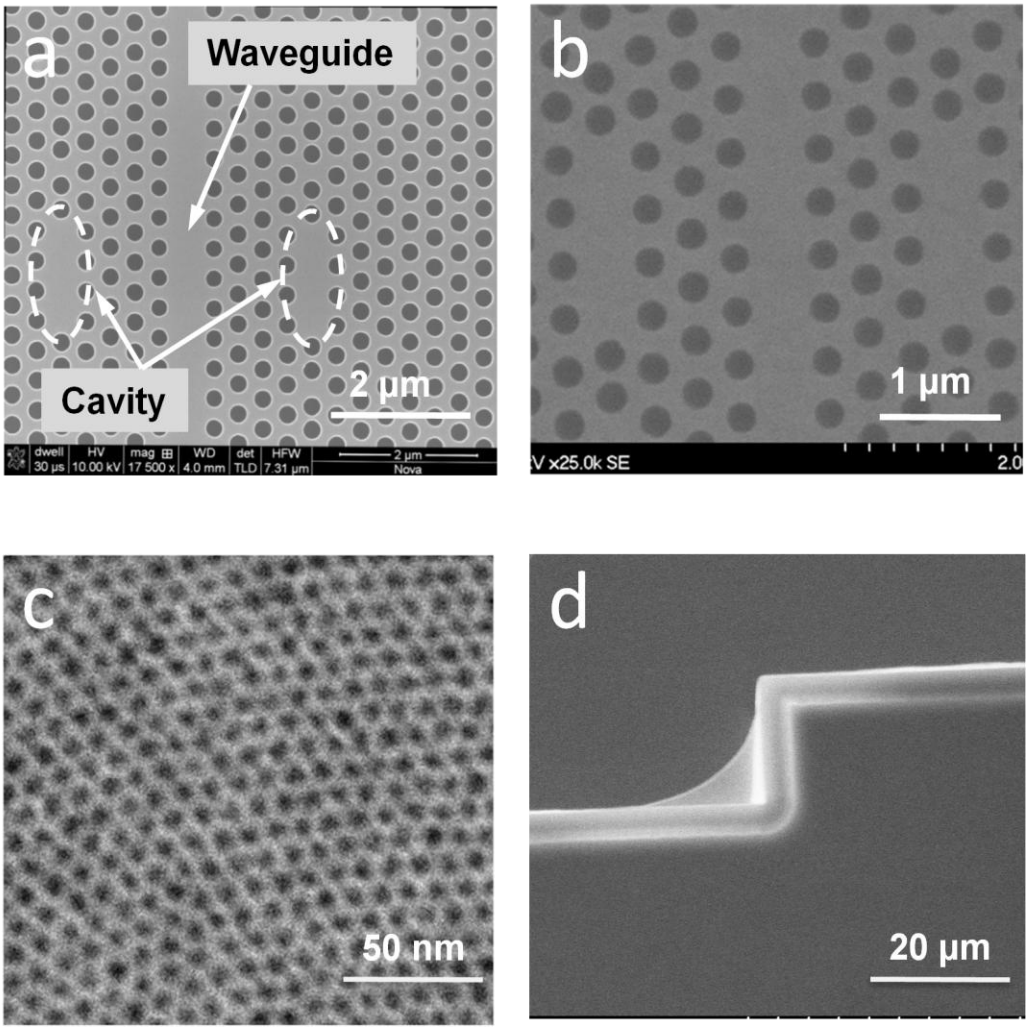

Figure 5 (a, b) SEM images of a photonic crystal device before and after coating with a PbS-P3HT composite monolayer film. (c) TEM image of the PbS-P3HT monolayer. (d) a SEM image of a freely suspended monolayer spanning a corner feature of the device (This freely suspended region is used as a control to monitor optical properties of the monolayer itself).

The hydrophobic PbS QDs reside preferentially at the air/polymer interface as determined by X-ray reflectivity measurements[144] and atomic force microscopy (AFM, see below). To transfer the monolayer to a photonic crystal or other device, we use the 'picking' or 'lifting' transfer procedures, respectively. As shown in Figure 4b, the picking process consists of lowering the photonic crystal device (see supporting information for fabrication process of the photonic crystal device; SEM images shown in

Figure 5a, b.) from the air side toward the floating monolayer with the functional surface of the photonic crystal face down as illustrated in Figure 4b. This enables the QDs to be in close contact with the photonic crystal cavity, since the QDs reside at the polymer/air interface of the interfacially assembled array. In this case, the QDs and the photonic crystal are separated by only the stabilizing oleic acid ligand. To remove any residual water that might have been trapped in the film, the device was annealed at 100˚ C for 5 minutes in air. For plasmonic applications where it is desirable to have a dielectric spacer between the QDs and the device surface in order to reduce the non-radiative damping[145], the 'lifting' technique is more suitable. In this case, the photonic crystal substrate is first lowered into the water without touching the floating film, and then the substrate is retracted capturing the floating film with the polymer side down (Figure 4c).). The proximity of the QDs to the original vapor or water interfaces of the interfacially assembled monolayer is evident from AFM images of films transferred to silicon substrates by lifting or picking (Figure 4d). We observe an ordered nanoparticle surface topography for the original vapor side interface (AFM image of lifted monolayer) and a featureless topography for the original water interface (AFM image of picked monolayer). Here AFM is of course probing the opposite side of the film topography in contact with the photonic crystal surface for both transfer procedures.

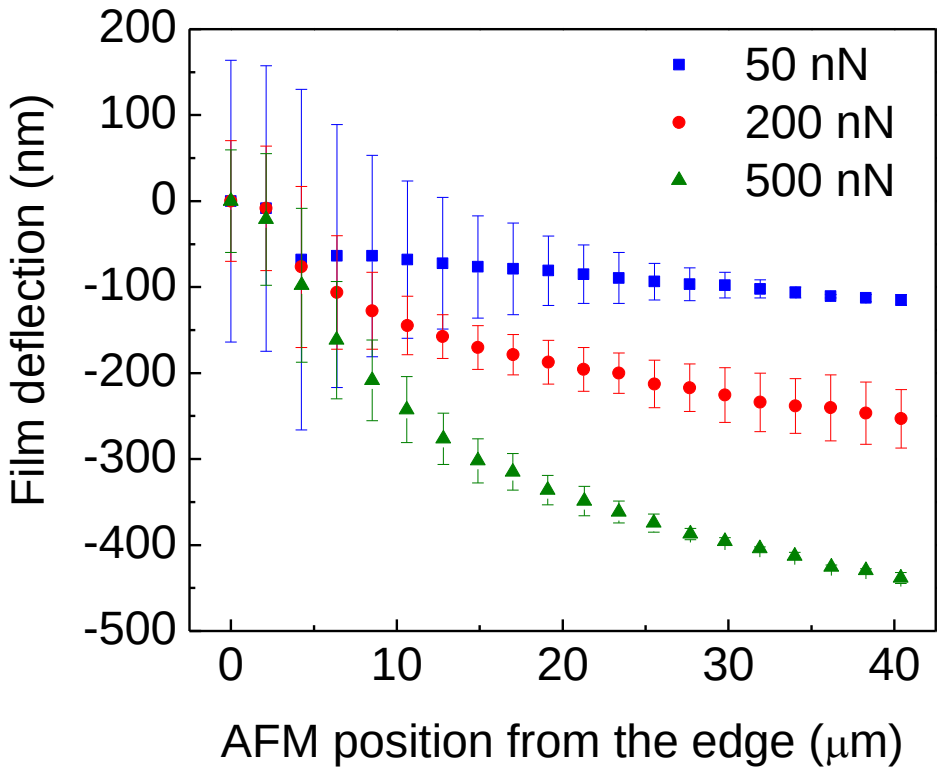

Figure 6 Film deflection as a function of radial distance from the hole circumference measured using AFM. Three different forces (50nN, 100nN, and 200nN) have being applied by the AFM tip. The Young's modulus determined from this data analyzed according to a simplified Reissner analysis is on the order of 10^9 Pa.

We have obtained high quality PbSe monolayer arrays using both P3HT and polystyrene polymers. It is important to note that, in both procedures the QD monolayer film remains freely suspended over the photonic-crystal surface without deforming and adhering to the side walls of the cavity. For example, Figure 5d shows a free-standing film suspended over a corner feature of the device. This is because the transferred QD/polymer film formed by this evaporation-induced interfacial assembly method is adherent and has a high elastic modulus. To directly measure the mechanical properties of the nanoparticle/polymer composite film, monolayer array was transferred to a copper

substrate with a single 150μm diameter circular hole in the center via the lifting process. The deflections of the film under different AFM nano-indentation forces are shown in Figure 6. The Young's modulus of PbS-P3HT film was determined to be about 10^9 Pa using a simplified Reissner analysis[146]. To confirm that the quantum dots are indeed in a close-packed configuration, the film can be transferred to a TEM grid and examined as shown in Fig 2c. The density of the PbS QD in our sample is estimated from the TEM image to be about $2x10^{12}$ cm^{-2} with film non-uniformity less than 20%. As determined by GISAXS[144] interfacial assembly and transfer procedure allows us to achieve an ordered (uniform) close-packed QD array over large areas.

5.4 Optical performance

To demonstrate the importance of having the QD array in close contact with the photonic crystal cavity, we compared the enhanced photoluminescence from samples prepared by the 'picking' and 'lifting' transfer processes. Figure 7a shows a dramatic enhancement in photoluminescence from the cavity mode for the QD film transferred to the photonic crystal by picking (blue curve) versus the supported QD film transferred by lifting (red curve). The difference between the two photoluminescence measurements is consistent with the fact that the 'picking' process allows the QDs to be in close contact with the photonic-crystal cavity, providing better coupling to the cavity and thereby yielding a larger enhancement. In contrast, for the 'lifting' process, the coupling is dramatically reduced despite the QDs being separated by only 20-nm from the cavity in the vertical direction. In both samples, resonances are observed at about 1460 nm with

the electric field polarized parallel to the waveguide axis. The broad background from the photoluminescence of QDs is similar to that obtained from a free-standing QD-polymer film (Fig 5d). In these experiments, we made no attempt to use more mono-dispersed quantum dots than those commercially available. We estimate on average there are 20 QDs per nm bandwidth residing on the antinodes of the microcavity. The highest Q factor observed with this deposition technique is about 8000 as shown in Figure 7(b), where the polarization of the photoluminescence is perpendicular to the waveguide axis To the best of our knowledge, this is the highest Q factor ever achieved using colloidal QDs coupled to a photonic crystal microcavity. We believe this Q factor reflects the quality of the photonic crystal rather than the transferred film. Numerical simulations have shown that theoretically the cavity Q with this polymer film can be as high as 25,000[147].

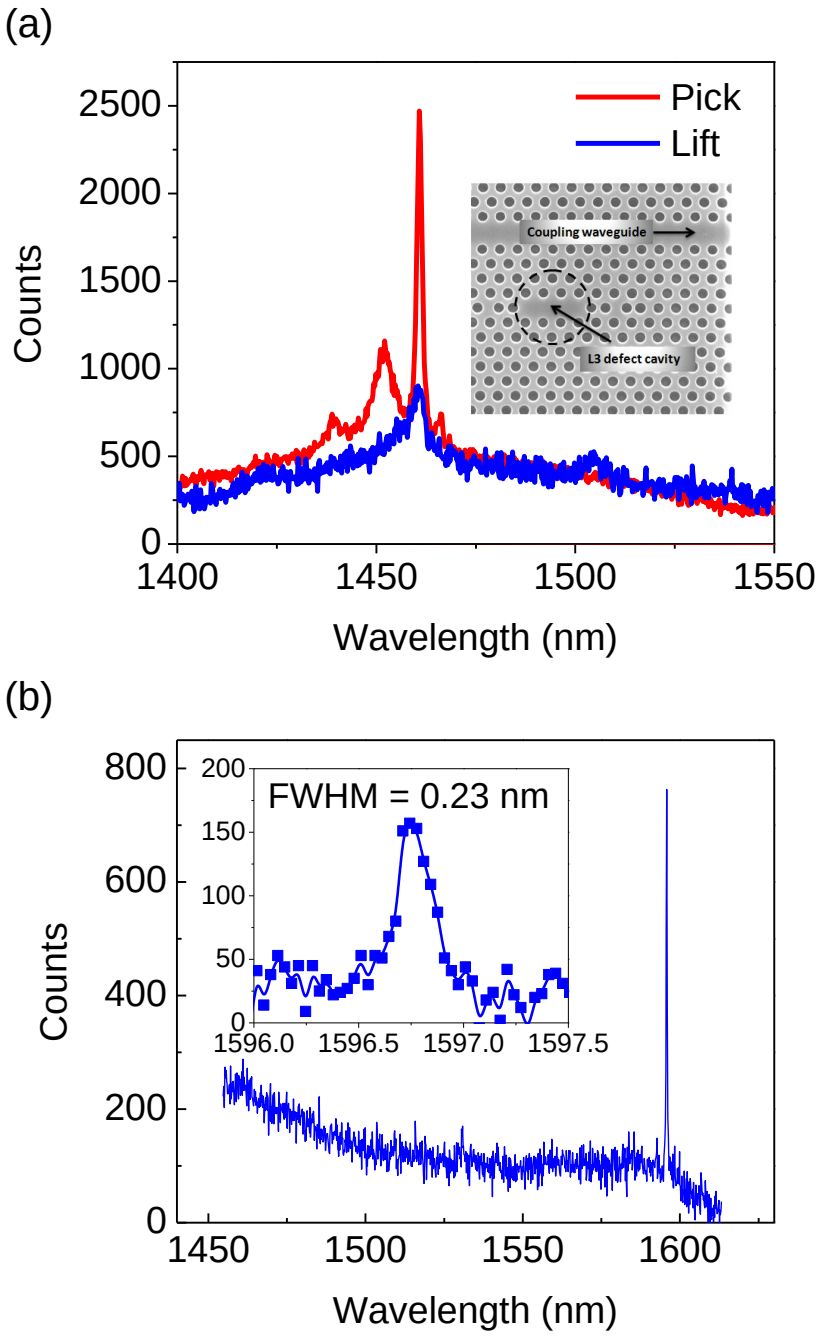

Figure 7 (a) Comparison of PL signals from the QD-photonic crystal cavity systems prepared by picking or lifting transfer processes. The inset denotes the region of excitation marked by a black dashed circle. This resonance is referred to as E_x resonance with its emission polarization parallel to the waveguide. The PL is collected by a spectrometer with a 300 g/mm grating and 50 µm slit width. (b) Enhanced photoluminescence spectrum of E_y resonance of a L3 photonic crystal microcavity collected by a spectrometer with a 300 g/mm grating and 50 µm slit width. The polymer used in the sample for this experiment is polystyrene. The inset shows a high-resolution measurement of the same resonance

measured with a 900 g/mm grating and a 10 µm slit width. The linewidth of the resonance is measured to be 0.2 nm and the corresponding Q factor is 8028.

5.5 Conclusion

In summary, we present a new and robust approach to deposit a uniform, densely packed and highly ordered QD/polymer monolayer onto a high Q photonic crystal cavity. A Q factor higher than 8000 has been achieved, indicating the compatibility of this technique with high Q cavities. This approach will enable applications that require integration of active nano-photonic emitting materials with passive micro-photonic structures.

Chapter 6. Study of Enhanced Emission of PbS Quantum Dots

6.1 Introduction

Quantum-dot (QD) emission in a microcavity has been intensively investigated recently due to rapid advances in achieving simultaneously high Q and small mode volume cavities [148]. Semiconductor quantum dot emitters in microcavities have the potential to realize practical devices such as zero threshold lasers[149], single and entangled photon sources[150,151], as well as quantum optics research[152-155]. In addition, the ability to enhance the emission rate by virtue of Purcell effect [156] is also important to silicon photonics[157], solid state lighting [158,159]and solar cell applications [159,160].

In the case of good emitters such as InAs quantum dots, in which the total dephasing and the radiative linewidth are both much smaller than the cavity linewidth, large enhancement in spontaneous emission have been clearly demonstrated in the weak coupling regime[156,161,162]. Recently, strong coupling behavior has also been demonstrated [163-165]. However, current understanding of non-ideal or "bad emitter" systems in which the dephasing width is much larger than the radiative width and the cavity linewidth, is less clear[140,166-171]. Examples of bad emitters are colloidal infrared PbS and PbSe quantum dots, Si nanocrystals and Er^{3+} ions in SiO_2 or silicon nitride. According to several theoretical studies[172-174], for emitter systems like PbS and PbSe quantum dots, the Purcell enhancement is negligible and is independent of the cavity Q factor but rather is determined by the emitter Q factor. Experimentally reported enhancement factors from

"bad emitters" have large amount of variation. A Purcell enhancement factor of 30 was reported by spin coating colloidal PbS quantum dots embedded in polymethylmethacrylate (PMMA) on photonic crystal microcavity with Q=400. An enhancement factor of 10 has also been reported with a cavity Q of 3000 [169] using selective chemical adsorption activated by AFM nanopatterning. In another case, PbS quantum dots were attached to the cavity by soaking which yielded an enhancement factor of 35 from a cavity with Q=775[167]. And for Er^{3+}ion in silicon nitride, a room temperature enhancement factor of 1.4 was reported from a cavity with Q=6000[175]. None of these studies have demonstrated linear dependence of enhancement factor to Q factor. In these PbS studies, the reported enhancement factor mechanism were attributed to Purcell effect even though the emitter linewidth of 100meV [176-178] clearly cannot support such a large enhancement factor. In addition, all these studies except for the AFM patterning case, the emitters are randomly distributed within the film, therefore the emitter distances from the surface of the photonic crystal are not well defined. There are also other unknowns such as the exact property of the quantum dots that are responsible for the enhanced emission and its interaction with the material of the microcavity.

6.2 Experiments

In this study, we attempt to eliminate one of these unknowns by placing a 20-50nm thick polymer film supporting a monolayer of close-packed PbS QDs onto the surface of a photonic crystal microcavity where these quantum dots are located only at the interface between the polymer and the photonic crystal. In this case, the surface of the cavity is uniformly covered with quantum dots and therefore there are an equal number of dots on the node and antinode region of the cavity [179]. The highest Q factor achieved with this

technique is greater than 8000. After studying a large number of cavity-emitter structures, our measurements show no clear linear relationship between the enhancement factor and the cavity Q has been found, which suggests that colloidal PbS QD is considered as "bad emitter" and previously observed enhancement may arise from different mechanism. In addition, the enhancement factor we observed is larger than the dielectric enhancement effect alone can produce. We will present our experimental results and speculate on possible enhancement mechanisms.

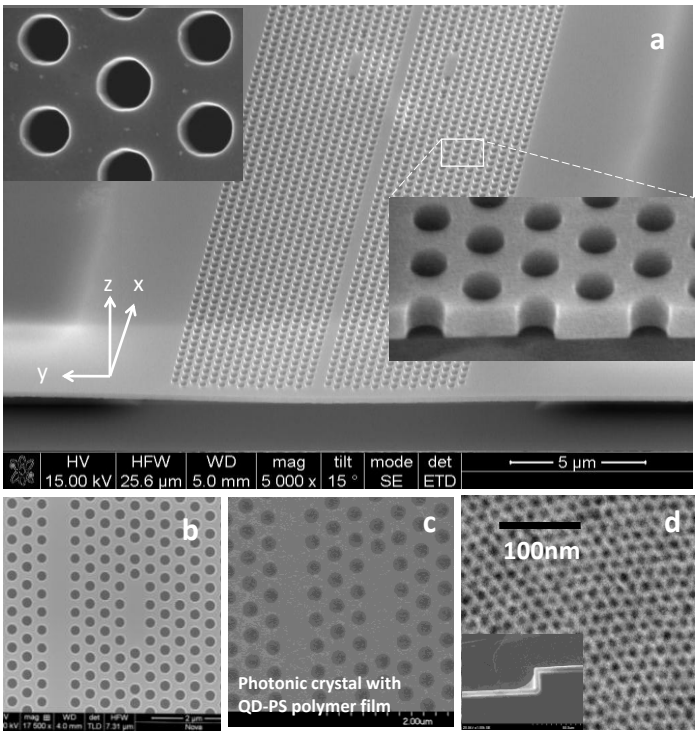

Figure 1. (a) SEM image of a 2D silicon membrane photonic crystal device consists of two L3 cavities and a waveguide supported with SiO_2 anchors. The top left inset shows the top view of the holes on the silicon membrane. The lower right inset shows the side wall profile of the holes. (b) Top SEM view of the L3 cavity created by three missing air holes. (c) SEM image of a cavity with polymer film on top. (d) TEM image of a monolayer of PbS in P3HT polymer. Lower left inset shows a free-standing film hanged by a corner feature of the photonic crystal sample.

6.3 Optical measurements and discussion

6.3.1 Spectroscopy of microcavity resonances

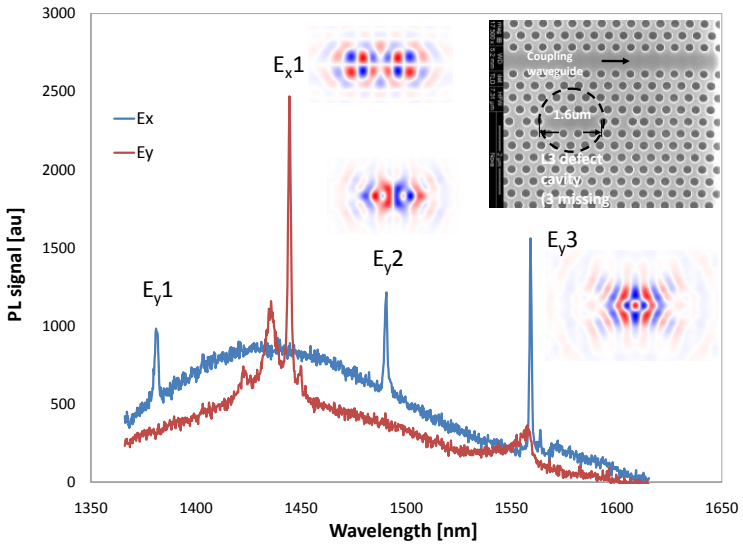

Figure 2. Measured photoluminescence (PL) spectrum taken from the same L3 cavity with polarization parallel (E_x) and perpendicular (E_y) to the long axis of the cavity. The calculated modal patterns are shown next to resonance peaks. The inset shows the excitation spot size relative to the cavity.

Emission comes mostly from the ground-state transition, involving states populated via collisional relaxation from higher lying levels in a picosecond time scale [180]. That fact that the PL signal has no dependence on the excitation polarization is consistent with this pump relaxation dynamics [181]. However, the PL from the cavity resonance is highly polarized and is present only when the quantum dots on the cavity are excited. The wavelengths of the resonances are expected to be slightly different from sample to sample due to variation in the polymer film thickness, but their relative positions are very reproducible and in agreement with Finite Difference Time Domain (FDTD) calculations. We have used both poly-3- hexylthiophene (P3HT) and polystyrene (PS) polymer for the deposition and the difference in performance turned out to be relatively

minor. A typical emission spectrum is shown in Figure 2. The highest Q factor observed from the E_y3 resonance is greater than 8000 using PS as the polymer matrix material. The broad background emission is from quantum dots that are either not coupled to the cavity or outside the cavity region excited by the laser. This emission is very similar to the one obtained from a free-standing film (free-film). The feature on the red trace at 1560nm is the $1.1W_1$ waveguide mode. The small features on the short wavelength side of the E_x1 resonance are hybridized modes caused by the coupling between the waveguide and the cavity. This coupling apparently has no effect on the E_y resonances.

Table 1: Calculated and measured wavelengths and Q factors of cavity resonances. E // WG means the electric field polarization of the PL is parallel to the waveguide (WG) and E X WG means the polarization of the PL is perpendicular to the WG.

$\omega a/2\pi c$	Identification	λ (*expt*/cal)	Q_{max} (*expt*/cal)	Experimental uncertainty (nm)
E X WG	Ex1	*1457.9*/1455.04	*600*/416	+/- 3
E // WG	Ey1	*1399*/1396	*720*/1214	+/- 10
E // WG	Ey2	*1512.44*/1511.7	*1257*/2182	+/- 11

For the photonic crystal band structure, wavelengths of micro-cavity resonances, and Q factors calculations, we use the MIT Electromagnetic Equation Propagation (MEEP) simulation environment[182]. The photonic crystal structure including the polymer film is discretized into a three dimensional computational supercell of 20 x 16 x 20 periods. Quantum-dot emission is simulated by an arrangement of multiple point current sources covering the waveguide and L3 cavity. For each point source, we use a Gaussian pulse centered at a reduced frequency of 0.273 (in unit of $c/2\pi a$) with a frequency spread of 0.05. To account for the existence of a bandgap in the transverse electric (TE) polarization of the L3 structure, the current sources are oriented in the z direction.

Computation of the Eigen modes together with their quality factors (Q) were performed with the harmonic inversion technique [183], which determines the resonant frequencies, decay constants, amplitudes, and phases of sinusoids composing a discretized time signal. Unlike the more commonly used Fourier transform, harmonic inversion describes the signal using an adaptive, finite length series of decaying and non-decaying sinusoids. The respective time series of the electric components for use with harmonic inversion were detected in the far field at 8 periods (computational unit cells) away from the sources to match the detection condition in the laboratory. These time series were later processed via the harmonic inversion method to identify the resonant modes. For the Q factor and modal field calculations, we use a narrower (than quantum dot emission) bandwidth for the point sources and tune the emission frequency around the neighborhood of the mode resonances. The modal patterns for E_x1, E_y2 and E_y3 are shown in Figure 2. The quantitative agreement between theory and experiment is to within 1.5% in the resonant frequencies as summarized in Table 1. For the E_x1 resonance, the measured Q factor is higher than the calculated value. This may be due to the sensitivity of the cavity geometry, a very slight difference between input and actual cavity parameters may result in noticeable discrepancies. Examples of sensitive parameters include side-wall straightness, hole locations and diameters[143]. In addition, the integrated PL signal from the cavity-free patterned region is comparable to that obtained from a free-standing film, indicating that the photoluminescence signal is not being trapped or scattered outside the field of view of the detection system.

6.3.2 Angular distribution measurements

In order to be able to determine the enhancement factor of the emission, it is necessary to normalize the cavity-resonance emission to the emission in the absence of cavity influences. We chose emission from a free film as the reference because 1) the angular distribution from the film is guaranteed to obey the cosine law; 2) the PL intensity is very stable and uniform to within 20%. While the emission from the cavity-free patterned region is typically used as a reference in other work [166], we find this to be less reliable since the angular distribution is not necessary a cosine law distribution and it can be affected by any buckling of the photonic crystal membrane structure. The two measured angular distributions are shown in Figure 3. In addition, the intensity from the

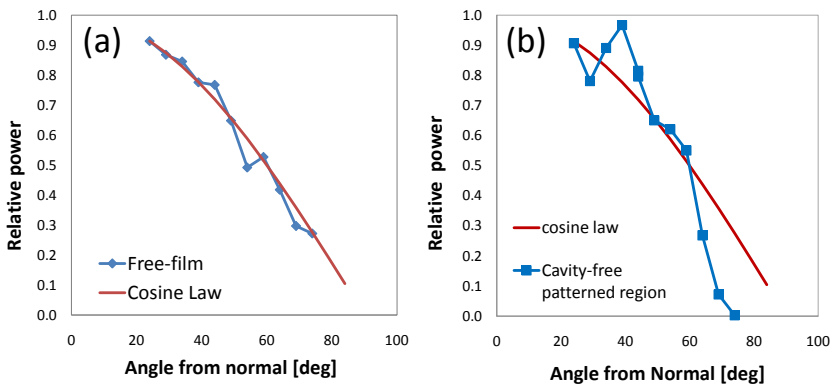

Figure 3. Measured angular distribution of photoluminescence from a free-film (a), and cavity-free patterned region (b) with a monolayer of close-packed quantum dots. All data are normalized to the value of cos(24°), which is the smallest angle the apparatus can measure. The inset of (b) is the calculated angular distribution.

cavity-free pattern region depends on conformity of the film to the photonic crystal surface.

As shown in Figure 4, a coarse measure of the angular behaviors and collection efficiencies of the cavity resonances is possible using different numerical aperture

focusing/collection objectives corrected for the transmission of the pump and signal wavelengths. The PL signals from 20x and 10x objectives are normalized to the collection efficiency value of 0.42 of 50x objective if it were a Lambertian source. To ensure this methodology is correct, we use the emission from a free-standing film (free-film) as a test case and obtained the expected Lambertian behavior. From these measurements, we determined that the emission from the free-film and anchor (pattern-free) regions have very similar behavior. Both E_x1 and E_y2 resonances do not have emission intensity peaked toward the normal direction due to significantly weaker signal than the Cosine law distribution when the 10x objective was used. These behaviors are consistent with the angular distributions obtained from numerical simulations shown in the insets of Fig 5c and 5d. Using an objective with a numerical aperture of 0.15, with an excitation spot size much larger than the cavity area, the PL signal is overwhelmed by the contribution outside of the cavity area and therefore no cavity resonance emission was discernable. Most importantly, these measurements show none of these emissions has a very directive behavior which can render gross errors in the enhancement factor estimates which will be discussed later.

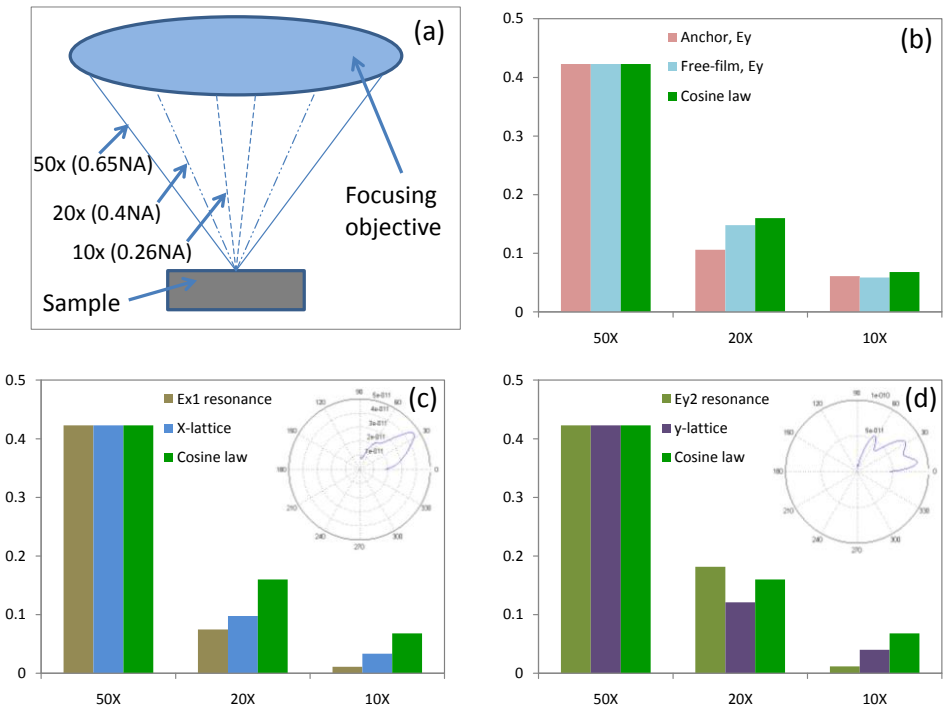

Figure 4. A schematic drawing depicts the collection geometries of different numerical aperture (NA) objectives (a). The PL signals from 20x and 10 objectives are normalized to the Lambertian collection efficiency valued 0.42 for 50x objective. The relative collection efficiency behaviors of the PL from free-film, anchor region and the Cosine law (b) show minor deviation from the Cosine law behavior. The relative collection efficiencies of E_x1 (c) and E_y2 (d) resonances using 10x objective are much smaller than Cosine law behavior indicating the emissions directed away from normal in agreement with simulation results (insets).

6.3.3 Enhanced emission from the Fabry-Perot-like waveguide resonances

Along the y direction, the waveguide can be viewed as a Fabry-Perot (FP) cavity bounded by two photonic lattice mirrors. The propagation vector of the FP cavity modes is along the y direction, and therefore its electric field is along the x direction. When the excitation source is focused on the waveguide, enhanced emission along x polarization is observed shown in Figure 5. This emission is 12 times larger than that of the free film. No distinct resonance is observed in the y polarization. The background emission arises from the emitters not coupled to the FP cavity resonance nor to the photonic crystal slab

scatteres to the free-space. The excitation area is defined by the excitation spot diameter along x direction and the width of the waveguide in the y direction, therefore this area is comparable to the L3 microcavity. Correcting for excitation area that can couple to the waveguide (area ratio = 5), the emission rate is approximately 50 times larger than free film even if one assume 100% collection efficiency[184].

As mentioned before, the Purcell effect is small because of the low emitter Q. However, dielectric enhancement mechanism does not depend on the Q factor of the emitter or cavity Q. It is known that the presence of high refractive index material enhances the emission rate by a factor of n in a conventional macroscopic field correction. This arises from the fact that the vacuum field amplitude is reduced by a factor of n, but the free space density of states increases as n^3. It was pointed out [185-187] that the local field effect can introduce significant correction to the macroscopic picture, the spontaneous emission rate of a dipole in a dielectric medium is given as $\Gamma_D = \left(nL^2\right)\Gamma_{vac}$, where Γ_D and Γ_{vac} are the decay rates of an emitter in a dielectric and vacuum respectively, L is the local field enhancement factor. In the absence of local field enhancement (L=1), the enhancement factor from the dielectric effect is n. There are many local field models: for the real-cavity model, $L=(3n^2)/(2n^2+2)$ [188]; virtual cavity, $L=(n^2+2)/3$[186,189]; and the Crenshaw model, $L=((n^2+2)/3n)^{1/2}$ [190]. Experimental studies in the index range of 1.3-1.7 have shown agreement with the real cavity model. Based on the real cavity model for silicon, a significant dielectric enhancement factor $EF_D=nL^2=7.3$ is obtained.

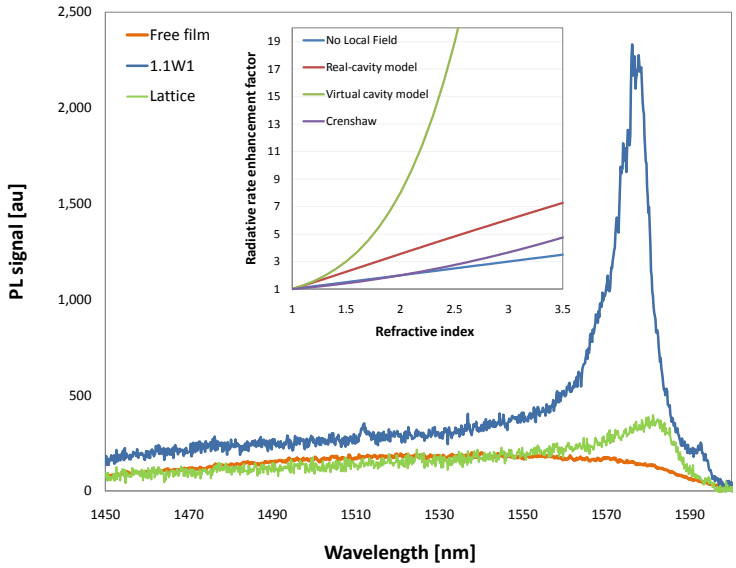

Figure 5. Enhanced emission from the Fabry-Perot-like resonance of the 1.1W$_1$ waveguide, free film and lattice regions. Subtracting the peak signal from the background at 1530nm, the enhancement factor with respect to the free film without area correction is 12. The inset shows the dielectric enhancement factor for different index enhancement models.

We determine the dielectric enhancement factor for the free film on a TEM grid to be 1.8. Since these quantum dots reside on the polymer-air interface emit to the polymer is enhanced compared to the other side. This measurement provides an independent confirmation that the film is indeed thin enough that there is no trapped modes that could render a poor choice of reference. The measured value is slightly smaller than the expected 2.26 based on real-cavity model, we believe this is due to the mean field effect because the film thickness is much smaller that the emission wavelength. To determine the expected enhancement factor, we include the effects of the emitter area (A), enhanced absorption factor (E_A), dielectric enhancement (EF_D), Purcell cavity effect enhancement (EF_{cav}), coupling strength to the photonic crystal cavity (β), coupling strength to the

Table 2: **Estimated enhanced emission factor based on dielectric enhancement only.**

	A	EF_A	EF_D	EF_{cav}	β	η_{FS}	η_C	S [au]	Measured ratio
Free-film	1	1	1.8	n/a	n/a	1	0.42	0.95	1
1.1W_1 Resonance	0.2	1.3	7.3	1.0	1	1	1	1.54	8-12
E_x1 Resonance	0.16	1.3	7.3	1.0	1	1	0.45	0.72	8-16

free-space from the cavity (η_{FS}), and collection efficiency (η_C). Therefore, we write the expected signal (S) as

$S = A \cdot E_A \cdot EF_D \cdot EF_{cav} \cdot \beta \cdot \eta_{FS} \cdot \eta_C$, and the values in this expression for the free-film, waveguide and E_x1 resonances are shown in Table 2.

An enhanced absorption factor E_A=1.3 takes into account that the quantum dots resides on the surface of Si experience another pass of the excitation beam because the reflectivity of silicon is about 30%. In the end the observed enhancement factor is still 6 times below what we observed. This discrepancy cannot be causes by possible enhanced absorption in the upper band of the photonic lattice[191] because the enhanced emission from the cavity-free patterned region (lattice) is consistent with the enhanced absorption effect, shown in Figure 6.

6.3.4 Enhanced emission from microcavities

As discussed before, we use free-film emission as the reference. The enhancement factor is determined by taking the magnitude of the emission peak above the background and dividing by the free-film emission at the same wavelength. The enhancement factors for E_x1, E_y1, E_y2 and E_y3 are shown in Figure 6. The data shown are composed of

measurements performed on different samples using both P3HT and PS polymer. Notice that the expected linear dependence of the enhancement factor on Q due to the Purcell effect is absent confirming that PbS belongs to the "bad emitter" class. The exact value of the homogenous linewidth of PbS is still under debate. Single quantum dots[177] and temperature dependent[176] measurements of PbS emitting at 800nm and 1100nm respectively, the homogenous width was determined to be 100meV. Based on this linewidth, the Purcell enhancement is negligible.

As discussed before, the dielectric enhancement provides only a factor of 7.3. Again as in the waveguide mode case, we assume a maximum value of 1 for the coupling factor and free-space coupling efficiency to free space, simulated collection efficiency of 0.45, the estimated emission strength is still more than a factor of 10 from our observation.

A remaining concern is whether the observed emission enhancement is actually from

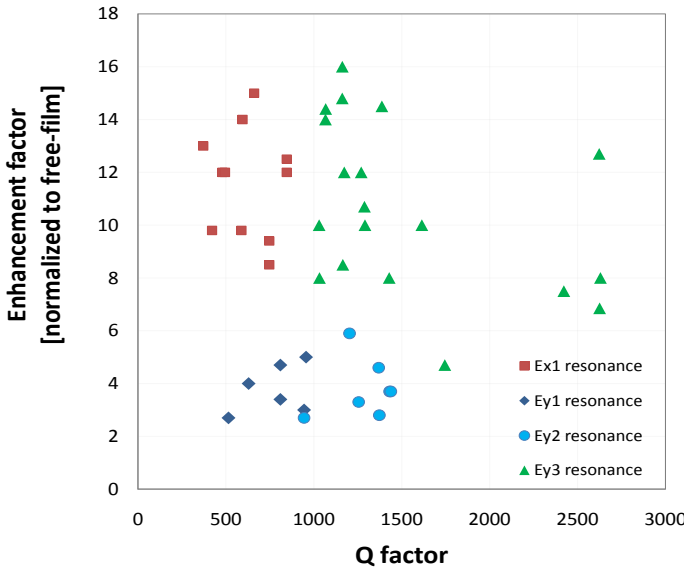

Figure 6. Measured enhancement factor of E_x1, E_y2, and E_y3 microcavity resonances with respect to the free-film. The enhancement factor is determined by the height of the resonance above the background emission divided by the emission of a free-standing film at the resonant frequency. The effect of excitation area to the cavity area is not included.

amplified spontaneous emission. To address this question, we performed intensity dependence studies and found three pieces of evidence to preclude this effect. First, with a change in excitation intensity from 10 W/cm^2 to 10^4 W/cm^2, we did not find an increase in slope in the emission intensity versus excitation intensity, which would indicate a transition from spontaneous emission to amplified spontaneous emission (Figure 8). In fact, they all show sub-linear behavior which can fit to a power law dependence of $y=a\ x^b$ very well; with b=0.73 for the E_x1 resonance at room temperature and b=0.78 for the E_y2 resonance at 105K. This sub-linear behavior[192] is commonly observed in colloidal quantum dots photoluminescence and is believed to be associated with the quantum dot blinking problem where quantum dot can be charged or carriers are trapped on the surface[193]. Second, the ratio between each emission peak and the background remains constant to within <20% over the same 3 orders of magnitude change excitation intensities, there is no spectral redistribution upon change in pump intensity. Third, we observed no linewidth narrowing effect for E_x1, E_y2 and E_y3 resonances.

6.4 Conclusion

We observed a more than 50 fold enhancement in the emission from both Fabry-Perot-like waveguide and microcavity resonances. Due to no apparent linear dependence of the enhancement factor to Q and the fact that it is a "bad emitter", we rule out Purcell effect as an enhancement mechanism. Since the dielectric enhancement effect can only account for a factor of 7.3, there remains more than a factor of 10 enhancement factor for the E_x1 resonance that cannot be accounted for. We are also able to rule out enhancement absorption based on the relative emission strength from the cavity-free

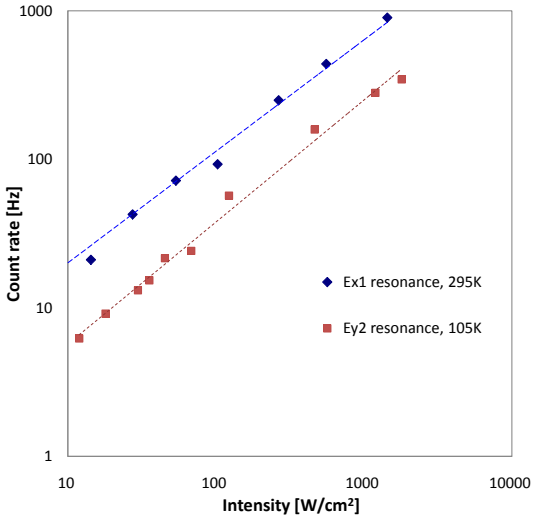

Figure 7. Intensity dependent behavior of E_x1 at 295K and E_y2 at 105K resonances. Both exhibit sub-linear intensity dependence of the form $y=ax^b$, where b=0.75 and 0.82 for E_x1 and E_y2 resonances respectively.

patterned region and free film. We are also able to rule out amplified spontaneous emission effect from the intensity dependent measurements. While conclusive confirmation of this enhancement factor requires lifetime measurements of emitters in these structures, and presently, this measurement is not feasible. It is worthwhile to point out that the quantum dots in this film are separated by only 1-2 nm gap in this

close-packed configuration which means that they are not strictly independent emitter. This may allow quantum dots outside the cavity to interact with the cavity which effective enlarge the area of influence of the cavity [194,195]. This effect will be investigated in future work.

Chapter 7. Summary and Future directions

7.1 Summary

Ordered 2D nanoparticle/polymer arrays have been fabricated by evaporation-induced interfacial self-assembly with controlled NP size, arrangement, spacing and symmetry. The monolayer array can be further transferred to arbitrary surfaces even with complicated topography. This represents a new route to couple bottom-up self-assembled nanostructure with traditional lithographic platforms, especially useful for electric and optical investigations.

In situ time-resolved Grazing Incidence Small Angle X-Ray Scattering (GISAXS) experiments were performed to follow the interfacial confined 2D NP assembly process driven by solvent evaporation. With increasing NP concentration we observe the system to transform from an isotropic state to a random close-packed state to a final highly ordered close packed monolayer, which is preserved within the polymer film. We observed the formation and decay of a transient random close packed configuration for two different NP to polymer ratios. The narrowness of the scattered lines is consistent with an ordered domain size of about 0.2 μm^2 (nearly the resolution limit).

X-ray reflectivity measurements were conducted to determine the NP depth profile in the final NP/polymer monolayer. The X-ray beam was scanned from 0.16 degree to 0.25 degree of incident angle, and the reflectivity data showed periodic oscillations. By fitting the reflectivity data, the electric field intensity (EFI) distribution is calculated as a function of the incident angle and film depth. The NP layer is located at 9.3nm below the

top surface with a vertical Gaussian distribution of $\sigma = 5.7$nm. This fitted electron density profile clearly shows that Au NPs are located near the very top surface of the transferred polymer film. Atomic force microscopy of the bottom/up surfaces of nanoparticle/polymer array confirmed this asymmetry due to phase separation. In combination with simulation tools, we studied the interfacial assembly of binary nanoparticle system and qualitatively determined the packing morphologies.

To transfer the monolayer to a photonic crystal or other device, we use the 'picking' or 'lifting' transfer procedures. The picking process consists of lowering the photonic crystal device from the air side toward the floating monolayer with the functional surface of the photonic crystal face. This enables the QDs to be positioned in close contact with the photonic crystal cavity, since the QDs reside at the polymer/air interface of the interfacially assembled array. If it's desired to space the NP array with a dielectric layer, the lifting procedure can be used.

We investigated the enhanced spontaneous emission from QD monolayer coupled to 2D Photonic crystal cavity. Comparison of PL signals from the QD-photonic crystal cavity systems prepared by picking or lifting transfer processes show dramatic difference. Enhanced photoluminescence spectrum of E_y resonance of a L3 photonic crystal microcavity was collected by high-resolution measurement with a 900 g/mm grating and a 10 μm slit width. The linewidth of the resonance is measured to be 0.2 nm and the corresponding Q factor is as high as 8028.

Transformation of close-packed 2D nanoparticle arrays into oriented nanorod/nanowire arrays stabilized within a polymer film has been demonstrated using scanning E-beam irradiation and annealing of transferred, free-standing NP/polymer

arrays with one unconstrained edge. Strain-induced directional retraction of the polymer matrix drives linear NP aggregation through a square-packed intermediate. The close proximity of the NPs to the surface and degraded polymer molecular weight allows rearrangement at points of contact to form single-crystal like nanorods. A diverse spectrum of anisotropic nanostructures can be created through control of the scanning e-beam. It's envisioned that mechanical instabilities of polymer matrices can also be utilized to direct assembly, for example, by applying a uniaxial or biaxial mechanical strain to the NP/polymer array.

In general, thorough study of 2D nanoparticle/polymer array, from assembly to transformation, to integration, and application was conducted respectively. We contribute to this nano array field of fast growth and increased competitively, in terms of deep understanding of assembly scheme, complete characterization, and elaborate integration into devices. We have successfully demonstrated a paradigm of combining top-down fabrication and bottom-up assembly, creating nano thin film materials with methodologies based on comprehensive interpretation of structure-property relations.

7.2 Future directions

Although NPs are well-known as catalytic materials, and have been amply investigated with respect to size, composition, shape, and substrate effects on catalytic properties, little is understood in terms of how placement in self-assembled lattices influences fundamental pathways of chemical transformations. We propose to investigate these effects, as well as demonstrate the formation of new NP catalytic architectures, using electrocatalysis with Pt nanoparticles embedded in a conductive

polymer as a model catalytic system. Specifically, we will examine methanol oxidation by Pt NPs combined with NPs of other metals or metal oxides within well-ordered superlattice NP/polymer arrays, where the second material creates ·OH species that react with adsorbed -C≡O species at the surface of the Pt particles. We will synthesize multicomponent superlattices of Pt NPs with other metal or metal oxide NPs to create binary (or higher order) catalytic architectures with well-defined geometries and interfaces between materials.

Another direction is to realize co-assembly of nanoparticles with block copolymers. In this way the nanoparticles can be positioned selectively in specific phase and the pattern dimension is also tunable. By applying external stimulus, responsive nanoparticle array for application in optics and catalysis will be studied. This part of work will be directly related to my future research.

REFENRENCES

(1) Schaffer, J. P.; Saxsena, A.; Antolovich, S. D.; Sanders, J. T. H.; Warner, S. B. *The science and design of engineering materials*; McGraw Hill: New York, 1999.

(2) Jortner, J.; Rao, C. N. R. *Pure and Applied Chemistry* **2002**, *74*, 1491.

(3) Huynh, W. U.; Dittmer, J. J.; Alvisatos, A. P. *Science* **2002**, *295*, 2425.

(4) Masciangioli, T.; Zhang, W. X. *Environmental Science and Technology* **2003**, 102A.

(5) Serp, P.; Corrias, M.; Kalck, P. *Applied Catalysis A* **2003**, *253*, 337.

(6) Knobel, R. G.; Cleland, A. N. *Nature* **2003**, *424*, 291.

(7) Cui, D.; Gao, H. *Biotechnology Progress* **2003**, *19*, 683.

(8) Collins, P. G.; Arnold, M. S.; Avouris, P. *Science* **2001**, *292*, 706.

(9) Rawlett, A. M.; Hopson, T. J.; Amlani, I.; Zhang, R.; Tresek, J.; Nagahara, L. A.; Tsui, R. K.; Goronkin, H. *Nanotechnology* **2003**, *14*, 377.

(10) Xiong, Z. H.; Wu, D.; Vardeny, Z. V.; Shi, J. *Nature* **2004**, *427*, 821.

(11) Gupta, M. C. *AIP Conference Proceedings* **2002**, *615*, 14.

(12) Binning, G.; Quate, C. F.; Gerber, C. *Physical Review Letters* **1986**, *56*, 930.

(13) Binning, G.; Rohrer, H.; Gerber, C.; Weibel, E. *Physical Review Letters* **1982**, *49*, 57.

(14) Williams, D. B.; Carter, C. B. *Transmission electron microscopy*; Plenum Press: New York, 1996; Vol. 1.

(15) Lee, H. J.; Ho, W. *Science* **1999**, *286*, 1719.

(16) Cao, G. *Nanostructures and nanomaterials: Synthesis, properties, and applications*; Imperial College Press: London, 2004.

(17) Timp, G. *Nanotechnology*; Springer: New York, 1999.

(18) Sidek, R. M.; Straube, U. N.; Waite, A. M.; Evans, A. G. R.; Parry, C.; Phillips, P.; Whall, T. E.; Parker, E. H. C. *Semiconductor Science and Technology* **2000**, *15*, 135.

(19) Li, Z.; Rajendran, B.; Kamins, T. I.; Li, X.; Chen, Y.; Williams, S. *Applied Physics A* **2005**, *80*, 1257.

(20) Geng, C.; Jiang, Y.; Yao, Y.; Meng, X.; Zapien, J. A.; Lee, C. S.; Lifshitz, Y.; Lee, S. T. *Advanced Functional Materials* **2004**, *14*, 589.

(21) Nutzenadel, C.; Zuttel, A.; Chartouni, D.; Schmid, G.; Schlapbach, L. *European Physical Journal D* **2000**, *8*, 245.

(22) Lieber, C. M. *Solid State Communictions* **1998**, *107*, 607.

(23) Niemeyer, C. M. *Angewandte Chemie International Edition* **2003**, *42*, 5796.

(24) Fritzsche, W.; Taton, T. A. *Nanotechnology* **2003**, *14*, R63.

(25) Bauer, L. A.; Birenbaum, N. S.; Meyer, G. J. *Journal of Materials Chemistry* **2004**, *14*, 517.

(26) Santos, D. H.; Garcia, M. B. G.; Garcia, A. C. *Electroanalysis* **2002**, *14*, 1225.

(27) Henglein, A. *Chemical Reviews* **1989**, *89*, 1861.

(28) Wang, Z. L. *Advanced Materials* **1998**, *10*, 13.

(29) Faraday, M. *Philosophical Transactions* **1857**, *147*, 145.

(30) Carpenter, E. E. *Journal of magnetism and magnetic materials* **2001**, *225*, 17.

(31) Reetz, M. T.; Helbig, W. *Journal of the American Chemical Society* **1994**, *116*, 7401.

(32) Tsutsui, G.; Huang, S.; Sakaue, H.; Shingubara, S.; Takahagi, T. *Japanese Journal of Applied Physics* **2001**, *40*, 346.

(33) Sato, T.; Hasko, D. G.; Ahmed, H. *Journal of Vacuum Science and Technology B* **1997**, *15*, 45.

(34) Templeton, A. C.; Wuelfing, W. P.; Murray, R. W. *Accounts of Chemical Research* **2000**, *33*, 27.

(35) Brust, M.; Kiely, C. J. *Colloids and Surfaces* **2002**, *202*, 175.

(36) Yin, A. J.; Li, J.; Jian, W.; Bennett, A. J.; Xu, J. M. *Applied Physics Letters* **2001**, *79*, 1039.

(37) Wu, Y.; Yan, H.; Huang, M.; Messer, B.; Song, J. H.; Yang, P. *Chemistry European Journal* **2002**, *8*, 1260.

(38) Sun.S; Meng, G.; Zhang, M.; Hao, Y.; Zhang, X.; Zhang, L. *Journal of physical chemistry B* **2003**, *107*, 13029.
(39) Wang, X.; Summers, C. J.; Wang, Z. L. *Nano Letters* **2004**, *4*, 423.
(40) Zhong, Z.; Wang, D.; Cui, Y.; Bockrath, W. M.; Lieber, C. M. *Science* **2003**, *302*, 1377.
(41) Liu, J.; Lin, Y.; Liang, L.; Voigt, J. A.; Huber, D. I.; Tian, Z. R.; Coker, E.; Mckenzie, B.; Mcdermott, M. J. *Chemistry: A European Journal* **2003**, *9*, 605.
(42) Yang, Y. H.; Wu, S. J.; Chiu, H. S.; Lin, P. I.; Chen, Y. T. *Journal of physical chemistry B* **2004**, *108*, 846.
(43) Lew, K. K.; Redwing, J. M. *Journal of Crystal Growth* **2003**, *254*, 14.
(44) Holmes, J. D.; Johnston, K. P.; Doty, R. C.; Korgel, B. A. *Science* **2000**, *287*, 1471.
(45) Sau, T. P.; Murphy, C. J. *Langmuir* **2004**, *20*, 6414.
(46) Ding, Y.; Gao, P. X.; Wang, Z. L. *Journal of the American Chemical Society* **2004**, *126*, 2066.
(47) Chung, S. W.; Ginger, D. S.; Morales, M. W.; Zhang, Z. F.; Chandrasekhar, V.; Ratner, M. A.; Mirkin, C. A. *Small* **2005**, *1*, 64.
(48) Piner, R. D.; Zhu, J.; Xu, F.; Hong, S. H.; Mirkin, C. A. *Science* **1999**, *283*, 661.
(49) Wu, Y. Y.; Yan, H. Q.; Huang, M.; Messer, B.; Song, J. H.; Yang, P. D. *Chemistry-a European Journal* **2002**, *8*, 1261.
(50) Cheung, C. L.; Hafner, J. H.; Odom, T. W.; Kim, K.; Lieber, C. M. *Applied Physics Letters* **2000**, *76*, 3136.
(51) Lieber, C. M. *Mrs Bulletin* **2003**, *28*, 486.
(52) Duan, X. F.; Huang, Y.; Cui, Y.; Wang, J. F.; Lieber, C. M. *Nature* **2001**, *409*, 66.
(53) Xie, X. W.; Li, Y.; Liu, Z. Q.; Haruta, M.; Shen, W. J. *Nature* **2009**, *458*, 746.
(54) Hurst, S. J.; Payne, E. K.; Qin, L. D.; Mirkin, C. A. *Angewandte Chemie-International Edition* **2006**, *45*, 2672.
(55) Smith, P. A.; Nordquist, C. D.; Jackson, T. N.; Mayer, T. S.; Martin, B. R.; Mbindyo, J.; Mallouk, T. E. *Applied Physics Letters* **2000**, *77*, 1399.
(56) Wang, Y.; Tang, Z. Y.; Podsiadlo, P.; Elkasabi, Y.; Lahann, J.; Kotov, N. A. *Advanced Materials* **2006**, *18*, 518.
(57) Kim, F.; Kwan, S.; Akana, J.; Yang, P. D. *Journal of the American Chemical Society* **2001**, *123*, 4360.
(58) Heath, J. R.; Knobler, C. M.; Leff, D. V. *Journal of Physical Chemistry B* **1997**, *101*, 189.
(59) Schultz, D. G.; Lin, X. M.; Li, D. X.; Gebhardt, J.; Meron, M.; Viccaro, P. J.; Lin, B. H. *Journal of Physical Chemistry B* **2006**, *110*, 24522.
(60) Motte, L.; Billoudet, F.; Lacaze, E.; Douin, J.; Pileni, M. P. *Journal of Physical Chemistry B* **1997**, *101*, 138.
(61) Rabani, E.; Reichman, D. R.; Geissler, P. L.; Brus, L. E. *Nature* **2003**, *426*, 271.
(62) Tang, J.; Ge, G. L.; Brus, L. E. *Journal of Physical Chemistry B* **2002**, *106*, 5653.
(63) Bigioni, T. P.; Lin, X. M.; Nguyen, T. T.; Corwin, E. I.; Witten, T. A.; Jaeger, H. M. *Nature Materials* **2006**, *5*, 265.
(64) Mueggenburg, K. E.; Lin, X. M.; Goldsmith, R. H.; Jaeger, H. M. *Nature Materials* **2007**, *6*, 656.
(65) Redl, F. X.; Cho, K. S.; Murray, C. B.; O'Brien, S. *Nature* **2003**, *423*, 968.
(66) Deegan, R. D.; Bakajin, O.; Dupont, T. F.; Huber, G.; Nagel, S. R.; Witten, T. A. *Nature* **1997**, *389*, 827.
(67) Shenhar, R.; Norsten, T. B.; Rotello, V. M. *Advanced Materials* **2005**, *17*, 657.
(68) Shevchenko, E. V.; Talapin, D. V.; Kotov, N. A.; O'Brien, S.; Murray, C. B. *Nature* **2006**, *439*, 55.
(69) Santhanam, V.; Liu, J.; Agarwal, R.; Andres, R. P. *Langmuir* **2003**, *19*, 7881.
(70) Santhanam, V.; Andres, R. P. *Nano Letters* **2004**, *4*, 41.
(71) Lin, X. M.; Parthasarathy, R.; Jaeger, H. M. *Applied Physics Letters* **2001**, *78*, 1915.
(72) Lin, X. M.; Jaeger, H. M.; Sorensen, C. M.; Klabunde, K. J. *Journal of Physical Chemistry B* **2001**, *105*, 3353.
(73) Hoole, A. C. F.; Welland, M. E.; Broers, A. N. *Semiconductor Science and Technology* **1997**, *12*, 1166.

(74) Schierhorn, M.; Boettcher, S. W.; Peet, J. H.; Matioli, E.; Bazan, G. C.; Stucky, G. D.; Moskovits, M. *Acs Nano* **2010**, *4*, 6132.

(75) Kim, J. S.; Seo, B. W.; Gu, H. B. *Synthetic Metals* **2003**, *132*, 285.

(76) Kim, J. S.; Kim, S. K.; Gu, H. B. *Molecular Crystals and Liquid Crystals* **2003**, *405*, 113.

(77) Jo, J.; Lee, T. M.; Yu, J. S.; Kim, C. H.; Kim, D. S.; Lee, E. S.; Esashi, M. *Sensors and Materials* **2007**, *19*, 487.

(78) Alivisatos, A. P. *Endeavour* **1997**, *21*, 56.

(79) Alivisatos, A. P.; Barbara, P. F.; Castleman, A. W.; Chang, J.; Dixon, D. A.; Klein, M. L.; McLendon, G. L.; Miller, J. S.; Ratner, M. A.; Rossky, P. J.; Stupp, S. I.; Thompson, M. E. *Advanced Materials* **1998**, *10*, 1297.

(80) Daniel, M. C.; Astruc, D. *Chemical Reviews* **2004**, *104*, 293.

(81) Murray, C. B.; Norris, D. J.; Bawendi, M. G. *Journal of the American Chemical Society* **1993**, *115*, 8706.

(82) Sun, S. H.; Murray, C. B.; Weller, D.; Folks, L.; Moser, A. *Science* **2000**, *287*, 1989.

(83) Sun, S. H.; Anders, S.; Thomson, T.; Baglin, J. E. E.; Toney, M. F.; Hamann, H. F.; Murray, C. B.; Terris, B. D. *Journal of Physical Chemistry B* **2003**, *107*, 5419.

(84) Zhou, W. L.; He, J. B.; Fang, J. Y.; Huynh, T. A.; Kennedy, T. J.; Stokes, K. L.; O'Connor, C. J. *Journal of Applied Physics* **2003**, *93*, 7340.

(85) Gattas-Asfura, K. M.; Constantine, C. A.; Lynn, M. J.; Thimann, D. A.; Ji, X. J.; Leblanc, R. M. *Journal of the American Chemical Society* **2005**, *127*, 14640.

(86) Kuroishi, K.; Chen, M. P.; Kitamoto, Y.; Seki, T. *Electrochimica Acta* **2005**, *51*, 867.

(87) Lin, Y.; Boker, A.; He, J. B.; Sill, K.; Xiang, H. Q.; Abetz, C.; Li, X. F.; Wang, J.; Emrick, T.; Long, S.; Wang, Q.; Balazs, A.; Russell, T. P. *Nature* **2005**, *434*, 55.

(88) Bruchez, M.; Moronne, M.; Gin, P.; Weiss, S.; Alivisatos, A. P. *Science* **1998**, *281*, 2013.

(89) Huynh, W. U.; Dittmer, J. J.; Alivisatos, A. P. *Science* **2002**, *295*, 2425.

(90) McDonald, S. A.; Konstantatos, G.; Zhang, S. G.; Cyr, P. W.; Klem, E. J. D.; Levina, L.; Sargent, E. H. *Nature Materials* **2005**, *4*, 138.

(91) Haruta, M. *Gold Bulletin* **2004**, *37*, 27.

(92) Liu, J.; Lee, T.; Janes, D. B.; Walsh, B. L.; Melloch, M. R.; Woodall, J. M.; Reifenberger, R.; Andres, R. P. *Applied Physics Letters* **2000**, *77*, 373.

(93) Pang, J. B.; Xiong, S. S.; Jaeckel, F.; Sun, Z. C.; Dunphy, D.; Brinker, C. J. *J Am Chem Soc* **2008**, *130*, 3284.

(94) Coe, S.; Woo, W. K.; Bawendi, M.; Bulovic, V. *Nature* **2002**, *420*, 800.

(95) Narayanan, S.; Lee, D. R.; Guico, R. S.; Sinha, S. K.; Wang, J. *Physical Review Letters* **2005**, *94*.

(96) Schmitt, J.; Decher, G.; Dressick, W. J.; Brandow, S. L.; Geer, R. E.; Shashidhar, R.; Calvert, J. M. *Advanced Materials* **1997**, *9*, 61.

(97) Tate, M. P.; Hillhouse, H. W. *The Journal of Physical Chemistry C* **2007**, *111*, 7645.

(98) Rasband, W.; ImageJ, U. *Bethesda, Maryland, USA* **1997**, *2007*.

(99) Brust, M.; Walker, M.; Bethell, D.; Schiffrin, D. J.; Whyman, R. *Journal of the Chemical Society-Chemical Communications* **1994**, 801.

(100) Talapin, D. V.; Rogach, A. L.; Kornowski, A.; Haase, M.; Weller, H. *Nano Letters* **2001**, *1*, 207.

(101) Pileni, M. *J. Phys. Chem. B* **2001**, *105*.

(102) Middleton, A. A., Winggreen, N.S. *Phys. Rev. Lett.* **1993**, *71*.

(103) Fan, H. Y.; Yang, K.; Boye, D. M.; Sigmon, T.; Malloy, K. J.; Xu, H. F.; Lopez, G. P.; Brinker, C. J. *Science* **2004**, *304*, 567.

(104) Shalkevich, N.; Escher, W.; Burgi, T.; Michel, B.; Si-Ahmed, L.; Poulikakos, D. *Langmuir* **2010**, *26*, 663.

(105) Kovalenko, M. V.; Scheele, M.; Talapin, D. V. *Science* **2009**, *324*, 1417.

(106) Chen, X. Q.; Saito, T.; Yamada, H.; Matsushige, K. *Appl Phys Lett* **2001**, *78*, 3714.

(107) Tao, A.; Kim, F.; Hess, C.; Goldberger, J.; He, R. R.; Sun, Y. G.; Xia, Y. N.; Yang, P. D. *Nano Lett* **2003**, *3*, 1229.

(108) Whang, D.; Jin, S.; Wu, Y.; Lieber, C. M. *Nano Lett* **2003**, *3*, 1255.

(109) Messer, B.; Song, J. H.; Yang, P. D. *J Am Chem Soc* **2000**, *122*, 10232.

(110) Huang, Y.; Duan, X. F.; Wei, Q. Q.; Lieber, C. M. *Science* **2001**, *291*, 630.

(111) Yu, G. H.; Cao, A. Y.; Lieber, C. M. *Nat Nanotechnol* **2007**, *2*, 372.
(112) Yu, G. H.; Li, X. L.; Lieber, C. M.; Cao, A. Y. *J Mater Chem* **2008**, *18*, 728.
(113) Pevzner, A.; Engel, Y.; Elnathan, R.; Ducobni, T.; Ben-Ishai, M.; Reddy, K.; Shpaisman, N.; Tsukernik, A.; Oksman, M.; Patolsky, F. *Nano Lett* **2010**, *10*, 1202.
(114) Javey, A.; Nam, S.; Friedman, R. S.; Yan, H.; Lieber, C. M. *Nano Lett* **2007**, *7*, 773.
(115) Fan, Z. Y.; Ho, J. C.; Jacobson, Z. A.; Razavi, H.; Javey, A. *P Natl Acad Sci USA* **2008**, *105*, 11066.
(116) Yerushalmi, R.; Jacobson, Z. A.; Ho, J. C.; Fan, Z.; Javey, A. *Appl Phys Lett* **2007**, *91*.
(117) Fan, Z. Y.; Ho, J. C.; Takahashi, T.; Yerushalmi, R.; Takei, K.; Ford, A. C.; Chueh, Y. L.; Javey, A. *Adv Mater* **2009**, *21*, 3730.
(118) Xiong, S. S.; Miao, X. Y.; Spencer, J.; Khripin, C.; Luk, T. S.; Brinker, C. J. *Small* **2010**, *6*, 2126.
(119) Croll, S. G. *J Appl Polym Sci* **1979**, *23*, 847.
(120) Finch, D. S.; Vesely, D. *Polymer* **1987**, *28*, 675.
(121) Plimpton, S.; Attaway, S.; Hendrickson, B.; Swegle, J.; Vaughan, C.; Gardner, D. *J Parallel Distr Com* **1998**, *50*, 104.
(122) Lane, J. M. D.; Grest, G. S. *Physical Review Letters* **2010**, *104*.
(123) Kang, S. L. In *Sintering-Densification, Grain Growth, and Microstructure*; Elsevier: Burlington, 2005.
(124) Chen, Y.; Palmer, R. E.; Wilcoxon, J. P. *Langmuir* **2006**, *22*, 2851.
(125) Nanda, K. K., Maisels, A., Kruis, F. E. *Journal of Physical Chemistry C* **2008**, *112*, 4.
(126) Ruiz, R.; Kang, H. M.; Detcheverry, F. A.; Dobisz, E.; Kercher, D. S.; Albrecht, T. R.; de Pablo, J. J.; Nealey, P. F. *Science* **2008**, *321*, 936.
(127) Bita, I.; Yang, J. K. W.; Jung, Y. S.; Ross, C. A.; Thomas, E. L.; Berggren, K. K. *Science* **2008**, *321*, 939.
(128) Song, J. H.; Wu, Y. Y.; Messer, B.; Kind, H.; Yang, P. D. *Journal of the American Chemical Society* **2001**, *123*, 10397.
(129) Collier, C. P.; Saykally, R. J.; Shiang, J. J.; Henrichs, S. E.; Heath, J. R. *Science* **1997**, *277*, 1978.
(130) Pileni, M. P. *Abstracts of Papers of the American Chemical Society* **2001**, *222*, U218.
(131) Oregan, B.; Gratzel, M. *Nature* **1991**, *353*, 737.
(132) Jiang, C. Y.; Markutsya, S.; Pikus, Y.; Tsukruk, V. V. *Nature Materials* **2004**, *3*, 721.
(133) Evers, W. H.; Friedrich, H.; Filion, L.; Dijkstra, M.; Vanmaekelbergh, D. *Angewandte Chemie-International Edition* **2009**, *48*, 9655.
(134) Tran, T. B.; Beloborodov, I. S.; Hu, J. S.; Lin, X. M.; Rosenbaum, T. F.; Jaeger, H. M. *Physical Review B* **2008**, *78*.
(135) Achermann, M.; Petruska, M. A.; Crooker, S. A.; Klimov, V. I. *Journal of Physical Chemistry B* **2003**, *107*, 13782.
(136) Shevchenko, E. V.; Talapin, D. V.; Murray, C. B.; O'Brien, S. *Journal of the American Chemical Society* **2006**, *128*, 3620.
(137) Talapin, D. V.; Shevchenko, E. V.; Bodnarchuk, M. I.; Ye, X. C.; Chen, J.; Murray, C. B. *Nature* **2009**, *461*, 964.
(138) Smith, D. K.; Goodfellow, B.; Smilgies, D. M.; Korgel, B. A. *Journal of the American Chemical Society* **2009**, *131*, 3281.
(139) Purcell, E. M. *Physical Review* **1946**, *69*.
(140) Fushman, I.; Englund, D.; Vuckovic, J. *Applied Physics Letters* **2005**, *87*.
(141) Hennessy, K.; Badolato, A.; Winger, M.; Gerace, D.; Atature, M.; Gulde, S.; Falt, S.; Hu, E. L.; Imamoglu, A. *Nature* **2007**, *445*, 896.
(142) Surrente, A.; Gallo, P.; Felici, M.; Dwir, B.; Rudra, A.; Kapon, E. *Nanotechnology* **2009**, *20*, 415205.
(143) Akahane, Y.; Asano, T.; Song, B. S.; Noda, S. *Nature* **2003**, *425*.
(144) Shisheng Xiong; Darren Dunphy; Zhang Jiang; Jing Wang; Brinker, C. J. *to be published*.
(145) Lakowicz, J. R.; Ray, K.; Chowdhury, M.; Szymanska, M.; Zhang, J.; Nowaczyk, K. *Analyst* **2008**, *133*.
(146) Komaragiri, U.; Begley, M. R.; Simmonds, J. G. *Trans. ASME, J. Appl. Mech.* **2005**, *72*, 203.

(147) Luk, T. S.; Chow, W. W.; Xiong, S.; Miao, X.; Farfan, B. G.; El-Kady, I.; Resnick, P. J.; Su, M. F.; Subramania, G.; Taha, M. R.; Brinker, C. J. *to be published*.

(148) Vahala, K. J. *Nature* **2003**, *424*, 839.

(149) Wiersig, J.; Gies, C.; Jahnke, F.; Aszmann, M.; Berstermann, T.; Bayer, M.; Kistner, C.; Reitzenstein, S.; Schneider, C.; Hofling, S.; Forchel, A.; Kruse, C.; Kalden, J.; Hommel, D. *Nature* **2009**, *460*, 245.

(150) Pelton, M.; Santori, C.; Vuckovic, J.; Zhang, B.; Solomon, G. S.; Plant, J.; Yamamoto, Y. *Phys Rev Lett* **2002**, *89*, 233602.

(151) Santori, C.; Fattal, D.; Vuckovic, J.; Solomon, G. S.; Yamamoto, Y. *Nature* **2002**, *419*, 594.

(152) Lounis, B.; Orrit, M. *Reports on Progress in Physics* **2005**, *68*, 1129.

(153) Khitrova, G.; Gibbs, H. M.; Kira, M.; Koch, S. W.; Scherer, A. *Nat Phys* **2006**, *2*, 81.

(154) Shields, A. J. *Nat Photon* **2007**, *1*, 215.

(155) Michler, P.; Imamoglu, A.; Mason, M. D.; Carson, P. J.; Strouse, G. F.; Buratto, S. K. *Nature* **2000**, *406*, 968.

(156) Makarova, M.; Vuckovic, J.; Sanda, H.; Nishi, Y. *Applied Physics Letters* **2006**, *89*.

(157) Tanabe, T.; Nishiguchi, K.; Kuramochi, E.; Notomi, M. *Opt. Express* **2009**, *17*, 22505.

(158) Phillips, J. M.; Burrows, P. E.; Daves, R. F.; Simmons, J. A.; Malliaras, G. G.; So, F.; J.A., M.; Nurmikko, A. V.; Smith, D. L. *Basic research needs for solid-state lighting*, 2006.

(159) Ji, M.; Park, S.; Connor, S. T.; Mokari, T.; Cui, Y.; Gaffney, K. J. *Nano Lett.* **2009**, *9*.

(160) Tiedje, T.; Yablonovitch, E.; Cody, G. D.; Brooks, B. G. *Ieee Transactions on Electron Devices* **1984**, *ED-31*.

(161) Kress, A.; Hofbauer, F.; Reinelt, N.; Kaniber, M.; Krenner, H. J.; Meyer, R.; Bohm, G.; Finley, J. J. *Physical Review B* **2005**, *71*.

(162) Lund-Hansen, T.; Stobbe, S.; Julsgaard, B.; Thyrrestrup, H.; Sunner, T.; Kamp, M.; Forchel, A.; Lodahl, P. *Phys Rev Lett* **2008**, *101*.

(163) Nomura, M.; Kumagai, N.; Iwamoto, S.; Ota, Y.; Arakawa, Y. *Optics Express* **2009**, *17*.

(164) Fushman, I.; Englund, D.; Faraon, A.; Stoltz, N.; Petroff, P.; Vuckovic, J. *Science* **2008**, *320*, 769.

(165) Faraon, A.; Fushman, I.; Englund, D.; Stoltz, N.; Petroff, P.; Vuckovic, J. *Nature Physics* **2008**, *4*, 859.

(166) Fujita, M.; Tanaka, Y.; Noda, S. *Ieee Journal of Selected Topics in Quantum Electronics* **2008**, *14*, 1090.

(167) Wu, Z.; Mi, Z.; Bhattacharya, P.; Zhu, T.; Xu, J. *Applied Physics Letters* **2007**, *90*.

(168) Makarova, M.; Sih, V.; Warga, J.; Li, R.; Dal Negro, L.; Vuckovic, J. *Applied Physics Letters* **2008**, *92*.

(169) Pattantyus-Abraham, A. G.; Qiao, H.; Shan, J.; Abel, K. A.; Wang, T.-S.; van Veggel, F. C. J. M.; Young, J. F. *Nano Letters* **2009**, *9*, 2849.

(170) Yang, J.; Heo, J.; Zhu, T.; Xu, J.; Topolancik, J.; Vollmer, F.; Ilic, R.; Bhattacharya, P. *Applied Physics Letters* **2008**, *92*, 261110.

(171) Gong, Y.; Makarova, M.; Yerci, S.; Li, R.; Stevens, M. J.; Baek, B.; Nam, S. W.; Hadfield, R. H.; Dorenbos, S. N.; Zwiller, V.; Vuckovic, J.; Dal Negro, L. *Opt. Express* **2010**, *18*, 2601.

(172) Meldrum, A.; Bianucci, P.; Marsiglio, F. *Opt. Express* **2010**, *18*, 10230.

(173) Ryu, H. Y.; Notomi, M. *Optics Letters* **2003**, *28*, 2390.

(174) Xu, Y.; Lee, R. K.; Yariv, A. *Physical Review A* **2000**, *61*, 033808.

(175) Makarova, M.; Sih, V.; Warga, J.; Li, R.; Dal Negro, L.; Vuckovic, J. *Applied Physics Letters* **2008**, *92*.

(176) Turyanska, L.; Patane, A.; Henini, M.; Hennequin, B.; Thomas, N. R. *Applied Physics Letters* **2007**, *90*, 101913.

(177) Peterson, J. J.; Krauss, T. D. *Nano Letters* **2006**, *6*, 510.

(178) Harbold, J. M.; Wise, F. W. *Physical Review B (Condensed Matter and Materials Physics)* **2007**, *76*.

(179) Xiong, S.; Miao, X.; Spencer, J.; Khripin, C.; Luk, T. S.; Brinker, C. J. *Small* **2010**, n/a.

(180) Schaller, R. D.; Pietryga, J. M.; Goupalov, S. V.; Petruska, M. A.; Ivanov, S. A.; Klimov, V. I. *Physical Review Letters* **2005**, *95*, 196401.

(181) An, J. M.; Califano, M.; Franceschetti, A.; Zunger, A. *Journal of Chemical Physics* **2008**, *128*.

(182) Joannopoulos, J. D.; Johnson, S. G.; Winn, J. N.; Meade, R. D. *Photonic crystals Molding the Flow of Light*, 2008.

(183) Mandelshtam, V. A.; Taylor, H. S. *Journal of Chemical Physics* **1997**, *107*, 6756.

(184) Tran, N.-V.-Q.; Combri; eacute; Sylvain; De Rossi, A. *Physical Review B* **2009**, *79*, 041101.

(185) Crenshaw, M. E. *Physics Letters A* **2006**, *358*, 438.

(186) Dolgaleva, K.; Boyd, R. W.; Milonni, P. W. *J. Opt. Soc. Am. B* **2007**, *24*, 516.

(187) Berman, P. R.; Milonni, P. W. *Physical Review Letters* **2004**, *92*, 053601.

(188) Glauber, R. J.; Lewenstein, M. *Physical Review A* **1991**, *43*, 467.

(189) Lorentz, H. A. *Theory of electrons*; Teubner, 1916.

(190) Crenshaw, M. E.; Bowden, C. M. *Physical Review Letters* **2000**, *85*, 1851.

(191) Ganesh, N.; Zhang, W.; Mathias, P. C.; Chow, E.; Soares, J. A. N. T.; Malyarchuk, V.; Smith, A. D.; Cunningham, B. T. *Nat Nano* **2007**, *2*, 515.

(192) Klimov, V. I.; Mikhailovsky, A. A.; Xu, S.; Malko, A.; Hollingsworth, J. A.; Leatherdale, C. A.; Eisler, H. J.; Bawendi, M. G. *Science* **2000**, *290*, 314.

(193) Liao, S.; Dutta, M.; Schonfeld, D.; Yamanaka, T.; Stroscio, M. *Journal of Computational Electronics* **2008**, *7*, 462.

(194) Clark, S. W.; Harbold, J. M.; Wise, F. W. *Journal of Physical Chemistry C* **2007**, *111*, 7302.

(195) Scholes, G. D.; Rumbles, G. *Nat Mater* **2006**, *5*, 683.

APPENDIX

Synthesis of Au NPs

Monodisperse Au NPs (about 5.5nm in diameter) were synthesized by a modified single phase method.[1] All chemicals were used as ordered from Aldrich. Briefly, 0.4 g of gold chloride and 1.4 g of didodecyldimethylammonium bromide were dissolved in 100 ml of toluene in a 500 ml flask with sonication. Under vigorous stirring, 0.2 g of sodium borohydride dissolved in 0.5 g of DI water was added dropwise into the flask. After 10 minutes of reduction, the solution turned dark red, and 2~4 ml of 1-dodecanethiol was added for ligand exchange. Excess reactant and water were removed by ethanol precipitation and evaporation using a RotoVap, respectively. After addition of another 2~4 ml of 1-dodecanethiol, the solution was taken to a heated oil bath and refluxed for 30 min. Heating was terminated and the flask was left in the oil bath overnight. The dark red Au NC colloid was then centrifuged at 3000 rpm for 5 minutes to remove any precipitates. The supernatant was concentrated with using a RotoVap. The NPs were precipitated out with methanol, vacuum dried, re-dissolved in chloroform to create a stock solution.

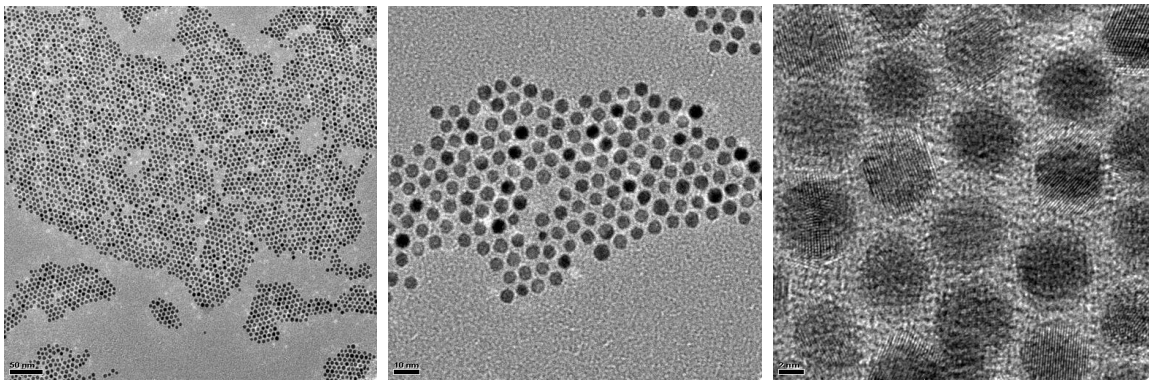

Figure A1 TEM images of Au NPs at different magnification

Synthesis of semiconductor and magnetic NPs

The CdSe nanorods (CdSe NR, about 14 nm in length and 4nm in diameter, stabilized by trioctylphosphine oxide and tetradecylphosphonic acid) and FePt nanoparticles (FePt NP, about 8nm in diameter, stabilized by oleylamine and oleic acid) were synthesized following the published procedures,[2, 3] respectively.

Precursors, reducing agents, and stabilizers used to synthesize nanoparticles are summarized and listed in Table A1 as reference.

Table A1 List of precursors, reducing agents, and polymer stabilizers for nanoparticle synthesis. [16]

Precursors		**Reducing agents**		**Polymer stabilizers**
	Formula		**Formula**	
Metal anode	Pd, Ni, Co	Hydrogen		Polyvinylpyrrolidone PVP
Palladium Chloride	$PdCl_2$	Sodium Citrate		Polyvinylalcohol PVA
Hydrogenhexachloroplatinate	H_2PtCl_6	Carbon Monoxide		Polyethyleneimine
Silver nitrate	$AgNO_3$	Phosphorous		Sodium Polyphosphate
Chloroauric acid	$HAuCl_4$	Methanol		Sodium Polyacrylate
Rhodium Chloride	$RhCl_3$	Hydrogen Peroxide		Tetraalkylammonium Halogenides

Characterization methods

The transmission electron microscopy (TEM) images were taken using a JEOL 2010 microscope operated at 200 kV. The scanning electron microscopy (SEM) images were taken using a Hitachi S-5200 electron microscope operating at an accelerating voltage of 5.0 kV. Ultraviolet-Visible (UV-Vis) absorption spectra of the NP solutions and thin films were measured on a PerkinElmer Lambda 45 UV-Vis spectrometer. Room-temperature photoluminescence (PL) spectra of semiconductor quantum dots (QDs) solutions and thin films were recorded by a Hamamatsu 928 photomultiplier tube (PMT), equipped with a SRS 830 lock in amplifier. All samples were excited by an Ar laser emitting at 518nm. Grazing incidence small-angle x-ray scattering (GISAXS) was performed on beamline 8-ID at the Advanced Photon Source of Argonne National Labs using a Marr 2048×2048 CCD detector, an energy of 7.35 keV, and a sample to detector distance of 1580 mm.

Degradation of Au/P3HTfilms studied from Raman Spectra

Au/P3HTmonolayer films were prepared and transferred onto cover glasses or Discovery platform. All these samples are made and then storaged for one week to two weeks. The Raman spectra were collected under 488 nm excitation laser.

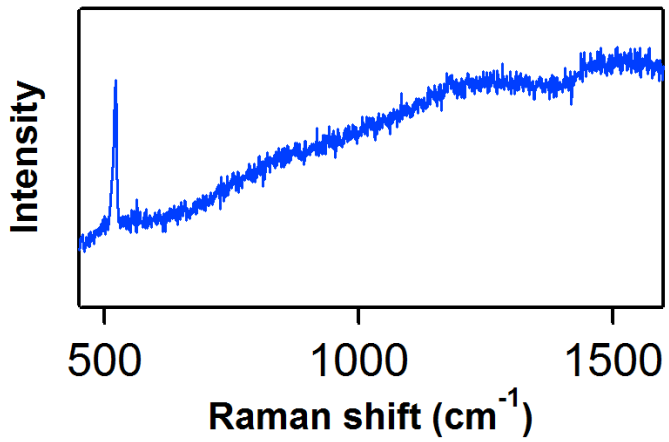

Figure A2 shows the Raman of annealed P3HTfilm on Discovery platform (DP).

There is only one sharp peak at ~520 cm^{-1}, which is assigned to be Si peak of DP. We obtained good S/N ratio Raman spectra of C=C mode of P3HT with fresh made samples without high intensity background. In this spectrum, the absence of P3HT Raman peaks and high background are maybe due to fluorescence of degradation. All samples are kept in N_2 box before test, what makes the destruction happen?

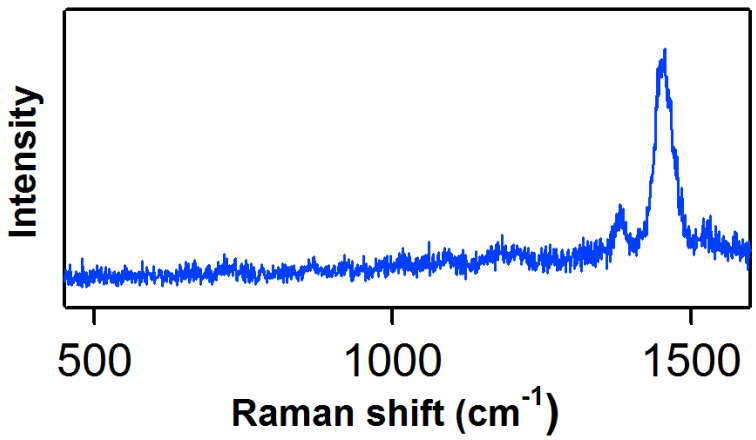

Figure A3 Raman spectrum of P3HT on glass kept for 14 days

While in Figure A3, annealed film of P3HT which was prepared 14 days ago still showed P3HT Raman peaks. This indicates that the plain P3HT film is quite stable in N_2 atmosphere. When put on DP, the degradation process is accelerated by some factors.

The difference of substrates suggests that the Au of electrode may react with thiophene ring when laser hits on the samples.

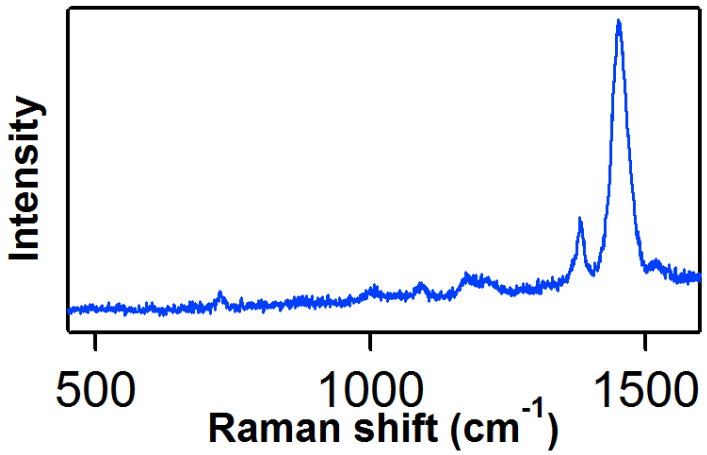

Figure A4 Raman spectrum of Au/P3HT on glass (14 days old)

Figure A4 shows the Raman spectrum of Au/P3HTmonolayer films on cover glass to test Au nanoparticles effect on degradation. This sample was also tested before and kept in N2 atmosphere for 14 days. The Raman spectrum shows very similar features with C=C and C-C modes. The results suggest that the nanoparticles are not the factor which accelerates the degradation process, which is reasonable because the nanoparticles are capped and protected with ligands, kept from the possible reaction with P3HT.

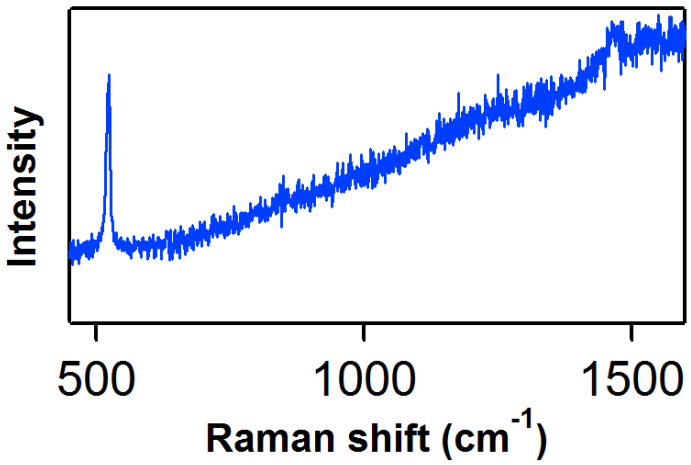

Figure A5 Raman spectrum of Au/P3HT on DP (7 days old)

Figure A5 shows the as-made Au/P3HT monolayer on DP which was 7 days old. We cannot resolve C=C and C-C peaks clearly due to very high background. Only Si band is showed and well resolved. Comparing all the Raman spectra above, the conclusion is that the P3HT or Au/P3HTfilms are stable on cover glass substrate. DP substrate accelerates the degradation process because of some chemical reactions, leading to the formation of defect species (traps) that alter device performance over time and repeated voltage cycling.

REFERENCES

(1) Deegan, R. D.; Bakajin, O.; Dupont, T. F.; Huber, G.; Nagel, S. R.; Witten, T. A. *Nature* **1997**, *389*, 827-829.

(2) Santhanam, V.; Liu, J.; Agarwal, R.; Andres, R. P. *Langmuir* **2003**, *19*, 7881-7887.

(3) Santhanam, V.; Andres, R. P. *Nano Letters* **2004**, *4*, 41-44.

LIST OF ABBREVIATIONS

2D	2 dimensional
AFM	Atomic Force Microscopy
CNT	Carbon Nanotubes
CVD	Chemical Vapor Deposition
DLS	Dynamic Light Scattering
DP	Discovery Platform
DPN	Dip-Pen Nanolithography
EDS	Energy Dispersive Spectroscopy
EISA	Evaporation Induced Self Assembly
EHP	Electron Hole Pair
FDTD	Finite Difference Time Domain
FET	Field Effect Transistor
FRET	Förster Resonance Energy Transfer
GISAXS	Grazing Incidence Small Angle X-ray Scattering
HRTEM	High Resolution Transmission Electron Microscopy
LAMMPS	Large-scale Atomic/Molecular Massively Parallel Simulator
LBL	Layer by Layer
LED	Light Emitting Diode
NP	Nanoparticle
NR	Nanorod
NW	Nanowire
P3HT	Poly (3-Hexylthiophene)
P3OT	Poly (3-Octylthiophene)
PDMS	Polydimethylsilozane
PEG	Polyethylene Glycol
PMMA	Poly(dimethyl metha acrylate)
PL	Photoluminescence
PS	Polystyrene
PS-PAA	*Polystyrene*-b-poly(acrylic acid)
PVC	Poly Vinyl Chloride
QD	Quantum Dot
SEM	Scanning Electron Microscopy
SERS	Surface Enhanced Raman Scattering
SLS	Solution Liquid Solid
STEM	Scanning Transmission Electron Microscopy
TEM	Transmission Electron Microscopy
UV	Ultraviolet
VLS	Vapor Liquid Solid